**Title**
Femtosecond laser nanomachining as a technique for probing the role of adhesion geometry and density on cell behavior

**Permalink**
https://escholarship.org/uc/item/4tg6h5hf

**Author**
Schmidt, Raymond C

**Publication Date**
2010

Peer reviewed|Thesis/dissertation

Femtosecond laser nanomachining as a technique for probing the role of adhesion geometry and density on cell behavior

by

Raymond Charles Schmidt


A dissertation submitted in partial satisfaction of the requirements for the degree of

Joint Doctor of Philosophy

with University of California, San Francisco

in

Bioengineering

in the

Graduate Division

of

University of California, Berkeley


Committee in Change

Kevin Healy (chair)
Valerie Weaver
Costas Grigoropoulos


Spring 2010

Femtosecond laser nanomachining as a technique for probing the role of adhesion geometry and density on cell behavior

© 2010

by Raymond Charles Schmidt

Abstract

Femtosecond laser nanomachining as a technique for probing the role of adhesion geometry and density on cell behavior

by

Raymond Charles Schmidt

Doctor of Philosophy in Bioengineering

Professor Kevin Healy, chair


A nanopatterning technique, termed femtosecond laser nanomachining, was developed in order to study the effect of clustering, placement, and overall cell adhesive ligand density on cell function.  The general patterning strategy was to render a quartz cell culture substrate non-fouling through the grafting of a pEG polymer, followed by femtosecond laser ablation of the polymer to generate regions into which cell adhesive peptides or proteins could be adsorbed.  Specifically, a high density ultrathin pEG brush layer was synthesized directly from the surface using surface initiated atom transfer polymerization, (SI-ATRP) a living radical polymerization with a constant growth rate that provides very low polydispersities.  As the film thickness varied linearly with time, demonstrated with *in situ* growth monitoring in a quartz crystal microbalance with dissipation (QCM-D), thickness was easily tunable, and the resulting surfaces had very low roughness (less than 1 nm RMS) as verified by AFM.  Surface chemistry was verified with x-ray photoelectron spectroscopy, (XPS) with a notable peak growth for energies associated with carbon-oxygen bonding, expected for a ethylene glycol rich polymer.  Exposure of pEG modified quartz oscillators to various peptide solutions resulted in minimal frequency and dissipation changes, reaffirming that our film robustly inhibits protein adsorption.

Our pEG thin film was then ablated with 400 nm wavelength femtosecond laser pulses focused with various far field objectives to elucidate the ablation thresholds of both our film and the underlying quartz substrate.  We identified an ideal processing window between fluences of 0.7 J/cm$^2$ (polymer threshold) and 1.5 J/cm$^2$ (quartz threshold), which results in clean film removal without damaging the underlying substrate.  The effect of laser fluence on feature diameter for various film thicknesses and objective magnifications was characterized to map processing parameters for patterned sample generation.  Protein adsorption into our ablated features was verified by fluorescence microscopy and AFM scanning samples prior to and post protein modification.  Cell adhesion on a variety of avidin derivative proteins and biotinylated peptides were quantified using a fluorescence based assay to assess an optimal ligand presentation system from our surface.  Neutravidin with biotin-bsp-RGD(15) was identified as an ideal adhesive ligand presentation system, due to maintenance of a high degree of cell adsorption with minimum background adhesion to the neutravidin itself. We used laser ablation to create a variety of substrates that are not easily accessible to other nanopatterning techniques, including one dimensional and two dimensional gradients of feature pitch, patterns designed to isolate single cells in different morphologies, and line patterns to control cell alignment and aspect ration.

To highlight the link between adhesion island size, pitch, and overall surface ligand density to the morphology and cytoskeletal development within the cell, gradient patterns and isometric

pitch samples were created to isolate these variables. Gradient patterns of both adhesive island diameter and pitch were created in order to define a critical ligand density for cell adhesion, determined to lie in the range of 0.15-0.3 pmol/cm$^2$ for the human mesenchymal stem cells on these patterned substrates. Patterns consisting of isometric pitch and diameter constrained within a non-fouling border were also created. For these patterns, rat mesenchymal stem cells were found to adhere down to densities of 0.03 pmol/cm$^2$. Nuclear distension was quantified with the nuclear shape index metric (maximum cross sectional area over the high of the nucleus) and a statistically significant difference in NSI ($p<0.05$) was found for cells adhered surfaces on designed to project ligand densities of 0.03 pmol/cm$^2$ and 1 pmol/cm$^2$, suggesting the underlying surface density modulates intracellular tension and nuclear distension.

# Table of Contents

# Table of Figures

# Table of Tables

# Table of Equations

# Nomenclature

| | |
|---|---|
| **AAm** | acrylamide |
| **AFM** | atomic force microscopy |
| **AG-73** | RKRLQVQLSIRT |
| **ATC** | allyltrichlorosilane |
| **ATRP** | atom transfer radical polymerization |
| **biotin-bsp-RGD(15)** | biotin-CGGNGEPRGDTYRAY-NH2, termed |
| **bipy** | 2-2'-bipyridine |
| **BIS** | N,N'-methylenebisacrylamide |
| **BSA** | bovine serum albumin |
| **CQ** | camphorquinone |
| **DDZ** | a,a-dimethyl-3,5-dimethoxybenzyloxycarbonyl |
| **DMEM** | Dubellco's minimum essential media |
| **DNA** | deoxyribonucleic acid |
| **e-beam** | electron beam |
| **ECM** | extracellular matrix |
| **EDAC** | 1-ethyl-3-(3-dimethylaminopropyl)carboiimide |
| **ERK** | extracellular related kinases, in this case referring to the signaling pathway in which it is involved |
| **FWHM** | full width half maximum |
| **IC** | integrated circuit |
| **IPN** | interpenetrating polymer network |
| **ISP** | ink, subtract, print |
| **MW** | molecular weight |
| **LI** | liquid immersion |
| **Matrigel** | purified basement membrane isolated from rat sarcomas |
| **MSC** | mesenchymal stem cell (hMSC denotes human, rMSC denotes rat) |
| **MTMS** | methacryloxypropyltrimethoxysilane |
| **NIH-3T3** | immortalized murine fibroblast cell line |
| **NMP** | nuclear matrix proteins |
| **NMR** | nuclear magnetic resonance |
| **NSOM** | near field scanning optical microscopy |

| | |
|---|---|
| **PBS** | phosphate buffered saline |
| **PDI** | polydispersity index |
| **pEG** | polyethylene glycol |
| **PEG-MA** | polyethylene glycol methacrylate |
| **PDEPMA** | poly(3,3'-diethoxypropyl methacrylate) |
| **PDMS** | polydimethylsiloxane |
| **PLL** | poly-L-lysine |
| **PMMA** | polymethylmethacrylate |
| **QCM-D** | quartz crystal microbalance with dissipation |
| **RGD** | integrin engaging cell adhesive peptide sequence Arginine-Glycine-Aspartic acid |
| **RGE** | scrambled version of RGD, swapping aspartic acid with glutamic acid (D to E) |
| **RMS** | root mean squared |
| **SAM** | self assembled monolayer |
| **SI-ATRP** | surface initiated radical polymerization |
| **UPW** | ultra pure water (ASTM Type I reagent grade water; 18.2 MΩ-cm, pyrogen free, endotoxin < 0.03 EU/m) |
| **UV** | ultraviolet |
| **XPS** | x-ray photoemission spectroscopy |

# Symbols

| | |
|---|---|
| $\lambda$ | wavelength |
| $\omega_0$ | Gaussian beam spot radius where intensity drops to $1/e^2$ of peak intensity |
| $d$ | radius of the first Airy disk for an optical diffraction pattern |
| $D$ | feature diameter |
| $F_0$ | laser fluence |
| $F_{th}$ | threshold fluence |
| $I$ | beam intensity |
| $I$ | initiator (for chemical reaction schemes) |
| $k$ | number of photons required to bridge the valence to conduction band gap |
| $K_{eq}$ | equilibrium constant |
| $k_p$ | rate constant of propagation |
| $k_t$ | rate constant of termination |
| $L$ | oxidizable metal ligand, used in ATRP |
| $M$ | monomer |
| $N$ | F number of a lens |
| $NA$ | numerical aperature |
| $P_{MPI}$ | probability of a multiphoton event |
| $P_n$ | polymer with (n)-mers |
| $P^\bullet$ | polymer containing a free radical |
| $R_p$ | rate of propagation |
| $X$ | halide |
| $z$ | atomic charge |

# Acknowledgements

First off, I would like to thank Hojeong Jeon and David Hwang, my collaborators in the Laser Thermal Lab. They both put a great deal of work into the laser processing and characterization described in this thesis. They were also very patient and helpful in aiding me to understand the complicated physics behind the ablation process. I would also like to thank Dr. Costas Grigoropoulos, for letting me try my experiments on his very, very expensive femtosecond laser system.

From the Healy lab, a number of people deserve acknowledgement. First, I would like to thank Kevin for his intellectual and (of course) monetary support of my project, and for his nudges in the right direction.

I would also like to thank:

Naomi Kohen for explaining the functioning and running of the QCM-D, and for finally paying me back all the beers she owes me (I hope).

Beth Irwin for the initial training on the IPN synthesis and polymerization in general.

Sam Wall for helping with my first forays into fluorescence microscopy.

Jacob Pollock for his general help in lab and a sounding board for ideas (as well as fantastic GRC trips and ridiculously long presentations)

Jeremy Barton for his recent help in sample prep and some SEM work.

From outside the lab, I would also like to thank:

Marty Mulvihill and Dr. Peidong Yang, U.C. Berkeley, for their help with synthesizing the silane ATRP initiator.

Dr Frank Ogletree for training me on the AFM.

Dr Ting Xu for her use of the spectral reflectometer.

I would also like to thank all my family and friends for being there during the good times, and putting up with the bad. Specifically, I want to thank my parents and sisters for supporting me through this endeavor. Chris and Jessie for all the lunches, barbeques, and road trips. Julie for all the baked goods. Jeff, Anuj, Craig, and Kyle for the snowboarding trips to Tahoe. And of course Tina, for the entertainment, companionship, and the bottle of blue label. Not to mention putting up with me while I largely ignored you over the last month.

# Chapter 1 - Hypothesis and Specific Aims

## 1.1 - Introduction

The cellular environment is a complex system of chemical, topographic, and mechanical signals, all of which can influence intracellular tension, cell migration, cytoskeletal organization, and ultimately cell fate.[1-7] Elucidating the individual effects of these signals has driven researchers to develop new techniques (or adopt techniques from other fields) to control the distribution of biomolecules and topographic features at the length scale of both cells and extracellular matrix proteins themselves. A range of studies already exist exploiting spatially resolved chemistry on a micrometer length scale;[5-10] however these studies are limited due to the inability to independently control cell adhesive area and ligand input to the cell via the adhesion domains presented on the surface. Mechanistically controlling ligand exposure to a cell can influence proliferation, differentiation, and gene expression. We and others have proposed that advanced nanopatterning technologies can control ligand presentation and overcome the previous limitations in cell-materials interaction studies.

An ideal nanopatterning technique would have the following attributes: 1) accessibility to biological researchers, 2) high throughput, 3) direct control over feature geometries, 4) the ability to pattern on a variety of substrates, 5) control over topographical features, and 6) the ability to passivate the areas surrounding the patterns from non-specific protein and cell adhesion. The main critical limitations to the generation of nanoscale cell ligand patterns are the lack of availability of many of the techniques to biological researchers and lack of throughput. The equipment required for generation of nanoscale patterns is highly specialized, such as e-beam sources, atomic force microscopes, or near-field scanning optical microscopes. The aforementioned techniques have focused on developing methodologies for patterning various biomolecules for cell studies, but the number of cell studies in the literature is limited, indicating that scale up of a many of these techniques is difficult. Colloidal or block co-polymer lithographies are the most accessible and do not suffer from scale up issues, but do not allow the user full control of the patterns generated, thereby limiting the types of biological questions that can be investigated. Therefore, development of a technique allowing for user controlled, repeatable, and easily scalable nanopatterns of surface chemistry will be critical in studying cell-material interactions.

## 1.2 - Objective

This thesis seeks to outline an optimized methodology for generating nanopatterned cell culture substrate in order to mechanistically probe the effect of focal adhesion clustering, spatial distribution, and ligand input on stem cell fate and function. We hypothesized that we could control cell adhesion, morphology, and nuclear shape by altering the underlying arrangement of cell adhesive sites. Nanopatterned substrates would allow us independently probe adhesion site size, pitch, and overall ligand input to the cell, decoupling confounding effects that were typically observed in past micropatterned studies. To achieve this, a patterning scheme was proposed to deposit and then remove a non-fouling polyethelyne glycol (**pEG**) polymer, creating protein or peptide islands within a passivated background that could act as adhesion sites for cells. Removal involved ablation of the polymer with femtosecond laser pulses focusing through far field optics. The process was coined "femtosecond laser nanomachining." In order to test our hypothesis, the following specific aims were identified.

### *1.3 - Specific Aims*

### 1.3.1 - Specific Aim A - Development and characterization of an non-fouling polymer surface with tunable thickness and low surface roughness

In this aim, we sought to develop a surface modification to prevent non-specific protein and cell adhesion, with a number of characteristics deemed critical for femtosecond laser nanomachining. The modified surface must eliminate non-specific protein adsorption, have low surface roughness(less than 5 nm peak to peak roughness), have tunable thickness, and absorb sufficient laser energy to ablate using a multiphoton ionization process. Surface initiate atom transfer radical polymerization (**SI-ATRP**), a controlled living radical polymerization, was identified as an ideal polymerization scheme due to the slow reaction speed and degree of control over polydispersity and molecular weight. To achieve this aim, the growth kinetics of an ultrathin pEG brush layer was characterized, and the ability of the film to resist protein adsorption was verified. Reaction conditions were also optimized to produce a nearly linear growth rate and a surface with minimum surface roughness (less than 1 nm RMS).

### 1.3.2 - Specific Aim B – Characterization of our polymer/substrate system's ablation characteristics with femtosecond laser pulses

For this aim, we sought to identify laser ablation conditions that would allow us to create nanoscale patterns on our pEG modified substrates. The ablation threshold of both the underlying quartz substrate and the pEG surface modification were experimentally determined to establish a processing regime which would allow for polymer film removal only. The ablated feature dimensions were measured for various laser fluences and objectives, giving us a framework for creating a wide range of feature sizes while only removing the polymer film. The final step was verification that proteins adsorbed into the ablated craters.

### 1.3.3 - Specific Aim C – Generation of nanopatterned substrata to probe cell adhesion, morphology, and nuclear distension

In this aim, a variety of cell culture substrates were created with varying feature geometries and pitch. A simple packing model was used to estimate the theoretical density of peptide on a patterned surface, given the dimension and pitch of the ablated craters. Gradients of pitch and feature diameter were created to determine a cutoff value for cell adhesion to the nanopatterns and outline patterning parameters used for nuclear shape analysis. Finally, nanopatterned cell culture substrates designed to have identical projected adhesion ligand densities through varying pitch and feature diameter were created, and used to determine if these variables independently modulate cell behavior.

### *1.4 - Organization*

This document outlines the development, characterization, and testing of a nanopatterning methodology. Logically, the document breaks down neatly into the development and full characterization of each particular step of our patterning process.

*Chapter 2*

The first chapter is a review of the current literature. As this thesis focused on the development of a novel cell culture patterning technique, a large portion of the introduction deals with an examination of currently available nanopatterning techniques, and their strength and

weaknesses in the biological arena.  Following this review, background material is presented on the physics of laser ablation as it relates to our polymer/substrate system.  This material is relevant to the laser ablation processing described in Chapter 4.  Background is also given for cell mechanics, as it relates to the cell studies in Chapter 6.  The role of adhesion ligand/integrin interaction and integrin clustering on focal adhesion formation is discussed, as well as how this relates to mechanical transduction within the cell, particularly around the nucleus.  This establishes the motivation for our cell studies.

*Chapter 3*

An ultrathin pEG layer with tunable thickness and low surface roughness was synthesized and characterized.  Chapter 3 provides an outline of the polymerization mechanism and kinetics, followed by thorough treatment of how the current pEG synthesis methodology was established.  The limitations of a polymer system previously developed in the lab, an interpenetrating polymer network of pEG and polyacrylamide (**pAAm**) were examined, which include unacceptable surface roughness and difficulty in producing ultrathin layers under 20 nm.  This was followed by optimization of the silane chemistry and deposition to produce a nearly smooth starting layer for the polymerization reaction.  Characterization of pEG brush layers synthesized by SI-ATRP using a quartz crystal microbalance with dissipation (**QCM-D**), atomic force microscopy (**AFM**), and x-ray photoemission spectroscopy (**XPS**) are detailed.  The chapter rounds out with QCM-D analysis demonstrating elimination of protein adsorption by the pEG brush.

*Chapter 4*

Chapter 4 focuses on characterizing the laser/material interaction of our polymer modified substrates. The dimensions of features ablated using femtosecond laser pulses on our substrates with various film thicknesses, laser fluences, and processing objectives were calculated and plotted to delineate an ideal processing regime.  Verification of protein adsorption in the features using fluorescent microscopy and AFM is also described.

*Chapter 5*

The commonly used avidin/biotin system is examined as a potential adhesive peptide presentation platform.  In Chapter 5, cell adhesion to a number of avidin derivatives, including streptavidin and neutravidin, is detailed.  This chapter also examines a number of blocking methods, the effect of serum on cell attachment to peptide modified surfaces, and cell adhesion to surfaces of mixed peptides.  The effect of mixtures of RGD, RGE, and AG-73 peptides on cell adhesion and morphology is also explored.

*Chapter 6*

In Chapter 6, the effect of ligand density on cells adhered to line patterns, gradient patterns, and isometric pitch patterns was determined.  Initial cell response to nanopatterned surfaces was observed using using video microscopy, while threshold peptide densities for cell adhesion to isometric pitch and line samples were also defined.  Isometric pitch samples designed to control overall ligand density with varying feature geometry were used to probe the effect of ligand density and arrangement on nuclear distension, indicating changes in intracellular tension.

*Chapter 7*

Here we detail what we have learned.  Chapter 7 summarizes the conclusions from each of the previous chapters, as well as analyzes the strengths and weaknesses of our particular patterning

scheme in the realm of biological studies.  Finally, future work and potential new directions are detailed.

# Chapter 2 -  Background and significance

The cellular environment is a complex system of chemical, topographic, and mechanical signals, all of which can influence intracellular tension, cell migration, cytoskeletal organization, and ultimately cell fate.[1-7] Elucidating the individual effects of these signals has driven researchers to develop new techniques (adopt techniques from other fields) to control the distribution of biomolecules and topographic features at the length scale of both cells and extracellular matrix proteins themselves.  Interactions between the extracellular matrix (**ECM**) and cell surface receptors, primarily the heterodimeric proteins known as integrins, initiate or modulate a wide range of signaling pathways.  The ability of integrins to cluster on the nanometer length scale is also critical to the activation of these pathways, as well as forming the basis of focal adhesion development, the initial structure required for polymerization of the actin cytoskeleton.  Nanometer scale spatial control of the ECM proteins or peptides that associate with integrins will be paramount to mechanistically examining the effects of integrin clustering, focal adhesion size and spatial arrangement, and ligand density on cell fate and function.

## 2.1 - Current nanopatterning techniques

A large body of work currently exists on micropatterning the cellular environment to examine the interdependent effects of cell morphology and spreading, cell-cell contacts, matrix composition on proliferation, cytoskeletal organization, and gene expression.[11]  A major limitation of these studies has been the inability to independently control the size of the cell adhesive domains and the ligand density exposed to the cell, leaving the question as to which factor dominates a specific observation unanswered. Ultimately, precisely displaying biological adhesion motifs on the nanometer length scale will allow researchers to directly modulate the placement of individual focal adhesions and their associated cytoskeletal elements, prompting development of new methods to create spatially resolved chemistries on the nanometer length scale.  This section reviews those techniques, and is previously published.[12]

A major hurdle in fabricating submicron patterned substrates has been that standard photolithographic techniques become prohibitively expensive as the pattern's scale moves below the diffraction limit of the processing light.  The diffraction limit is a physical limitation to any optical processing system that is governed by the wavelength of the processing light, the numerical aperture of the optics, and the refractive index of the processing media.  Although the diffraction limit can be decreased through techniques such as liquid-immersion photolithography and deep UV photolithography, this comes at a steep monetary cost.[13]  Microcontact printing, a common technique to creating microscale patterns quickly and cheaply, did not translate well into the nanoscale, as the low modulus of the elastomeric stamps limits pattern fidelity.[14, 15]  Alternatively, many nanoscale patterns of biological molecules (i.e., biological nanopatterns) have been created via non-photolithographic techniques, bypassing the diffraction issue altogether.  The diffraction limit can also be bypassed by processing with light in the near-field.  Scanning probe lithographies, electron beam lithography, and colloidal lithography have all been used to create nanoscale patterns by eliminating the need for photo-based processing.

An ideal system for a cell culture platform would allow for creation of nanoscale patterns of biological adhesion ligands against a background that resists non-specific protein absorption and is chemically stable for extended periods under cell culture conditions. Deconvoluting nanotopographical and chemical cues will also be critical, as both have been shown to affect cell

morphology and cytoskeletal development. The ability to quickly cover large areas of substrate with ligands in a user defined arrangement on the length scale of the particular ligands being patterned is also critical. Regarding the latter, a dichotomy exists in the available techniques: direct writing techniques allow the user to define specifically where the ligands are placed, but the time and expense to cover an entire cell substrate can be prohibitive; while colloidal lithography allows the user to quickly cover large areas with ligands, but is limited to simple geometric patterns. Although many of these techniques can be used for high resolution imaging and processing across a number of disciplines, this review will focus on biologically relevant nanopatterns, specifically schemes designed to control the spatial resolution of active biomolecules such as proteins, peptides, and nucleic acids.

### 2.1.1 - Photolithography

Standard i-line photolithography has been used to generate protein patterns down to 500nm by combining a pH degradable polymer system (poly(3,3'-diethoxypropyl methacrylate, **PDEPMA**) with a photoacid generator.[16] A combined solution of the polymer and the photoacid generator was spin coated on the substrate, followed by illumination through a photomask to cause degradation of the PDEPMA, generating localized regions of aldehydes on the surface that was subsequently exposed to UV light. These aldehyde regions were further modified using standard bioconjugate techniques to tether peptides or other biomolecules to the surface. While this technique does offer submicron resolution, the overall expense of photolithographic methods is increasing rapidly as pattern dimensions shrink as described above. The expense of mask creation, novel resist development, and facilities setup to take advantage of higher resolution photolithographic processes (i.e. deep-UV or liquid-immersion) is prohibitively expensive for most academic and biology labs.

### 2.1.2 - Serial 'Writing' Processes

*Scanning Probe Lithographies*

Scanning probe lithographies use the high resolution capabilities of scanning probe imaging techniques to chemically or topographically modify a surface, or directly "write" a molecular ink onto a surface. Silicon cantilever tips have been used to create localized chemistry by altering electrical fields, to physically scrape off molecules, or to deposit molecules that have been physisorbed onto the cantilever (i.e., dip-pen lithography).[17] These techniques offer very high resolution for both pattern generation and imaging the resulting modified substrates. However, for biological studies these techniques are limited in scope as the scanning probe coverage area is typically restricted to a single 100 micron square for standard instruments, clearly not useful for generating the number of samples needed for mechanistic studies of cell function and fate determination.

The simplest of these methods, oxidative lithography, utilizes a current capable probe tip and a conductive substrate to generate a voltage between the tip and the surface. The voltage can then chemically modify the surface to create patterned areas. For example, applying a +17V microsecond pulse to an ethylene glycol film created polarized regions approximately 90nm in diameter that selectively reacted with the heterobifunctional crosslinker EDAC (1-ethyl-3-(3-dimethylaminopropyl)carboiimide).[18] This crosslinker was then used to conjugate an avidin-biotin system to graft biomolecules to the surface. Protein features as small as 70nm have been written with this technique by oxidizing on a thiol rich surface to create thiolsulfinates and

thiolsulfonates, creating active areas for further conjugation.[19] Polymethylmethacrylate (PMMA) thin films and polyethylene glycol (PEG)-silane monolayers have also been utilized as substrates.[20, 21]  Oxidative lithography has also been used to selectively deprotect an amine functionality on a deposited monolayer, providing a versatile substrate for further chemical modification.[22] An amine terminated monolayer was protected with a common peptide protecting group, DDZ (a,a-dimethyl-3,5-dimethoxybenzyloxycarbonyl), which was selectively removed with an AFM derived voltage. With this technique, a minimum line width of 25nm was achieved.  Although this technique is able to generate high resolution patterns of spatial resolved chemistries, a number of restrictions limit the usefulness of this technique for patterning. The high voltage needed requires the use of a conductive substrate, and the limited scanning area of the probe tip and serial nature of the patterning technique present the same scale up issues that occur for all scanning probe techniques.

Dip-pen nanolithography and nanopipettes have been used to directly write molecules of choice on a surface, typically on an activated background. Dip-pen nanolithography requires dipping an AFM probe tip into a solution containing the molecule to be deposited, and then "writing" this molecule onto a surface with the tip.  The most common "inks" are alkanethiols, which allows patterns to be written on a gold surface followed by backfilling of the surface with a passivating moiety, such as oligoethylene glycol-terminated thiols.[23-25]  Line resolution as small as 40nm has been achieved using thiolated collagen on a gold surface.[26]  Biotin patterns have also been directly written onto polyethyleneimine[27] and a mercaptopropyl terminated silane[28] using dip-pen nanolithography.  Self-assembled monolayers of thiolated molecules can also be scraped or pushed off of the surface with an AFM tip, exposing the underlying gold substrate.  In this manner, squares of 500nm were created within various background SAMs, methyl and ethylene glycol terminated, that were then backfilled with another functionally active thiolate or a sulfhydryl terminated antibody.[29, 30] In one cell study, dip-pen nanolithography was used to create 500 nm spots of a hydroquinone  terminated alkanethiol that were then electrochemically modified to tether the ubiquitous cell adhesive Arg-Gly-Asp (**RGD**) peptide, a common cell binding amino acid sequence found in a number of extracellular matrix proteins.[31]  By creating 60 x 60 μm islands for cell adhesion with two different pitches within the single cell island (6 μm and 3 μm), its was shown that 3T3 mouse fibroblasts would polarize with their nucleus, Golgi apparatus, and centrosome preferentially located towards the higher density region of the pattern.

One limitation to scale up of dip pen nanolithography is that it requires the user to reink the tip of the cantilever to maintain a sufficient volume of solution on the tip.  To address this limitation, hollow fiber nanopipettes have been developed to deliver molecules to a surface in a similar manner to dip pen in a continuous flow, termed "nano fountain pen" lithography.  In this manner, glass slides precoated with streptavidin were patterned with biotinylated proteins and ss-DNA.[32] Flow rate from the pipette, and thereby solution volume, was controlled via an electrode formed by a wire inserted into the tip. In this study, resolution down to 800nm was achieved.  Proteins have also been printed directly onto a albumin coated glass slide with spots of 200nm in diameter using simple capillary action from the nanopipette.[33]  However, resolution is highly dependent on pipette diameter, tip sample spacing, and the interaction between the solvent, the pipette, and the surface.  Thus the processing parameters, and ultimately the resolution, depend on the specific chemistry employed.

Collectively, these cantilever based serial processes are limited in their application to cellular studies, since the scanning area for a typical AFM head with a single tip is limited to approximately a 100x100 micron area without moving the sample relative to the tip. This severely limits their throughput. Parallel dip-pen nanolithography uses an array of AFM cantilevers linked together, and offers the ability to more rapidly pattern larger areas than a standard single tip. This technique has been used to create 1cm by 1cm antibody arrays of 500nm dots separated 1 micron one SAMs.[24]  Although this technology improves the coverage area of the pattern, the user is still required to reink the entire array as the solution is deposited, ultimately limiting its usefulness for large scale cell behavior studies.  These parallel cantilever setups are also not commonly available to the biological community and must be specially designed and constructed, as the standard atomic force microscopes used for imaging typically only have a single scanning head.  Dip-pen nanolithography is a well established technique that has been widely touted as advantageous for creation of biosensors and nanopatterned cell substrates, but the lack of large scale cell studies suggests that scaling up production to produce large substrates, a wide range of experimental conditions, and statistically sufficient sample repeats is a significant obstacle.

*Near-field Scanning Optical Lithography:*

Another scanning probe technique allows for photo-based processing in the optical near field. Instead of direct chemical patterning, an AFM probe capable of delivering light through an aperture is used.  Near-field based lithography techniques depend on illumination through either a silicon cantilever with an aperture smaller than the wavelength of the processing light or a finely extruded fiber optic cable, which allows for resolution greater than the diffraction limit. In this manner, a near field scanning optical microscope (**NSOM**) coupled to the proper wavelength of laser can be used to pattern photoactive materials, such as resists, with line spacing down to 40-50nm.[34]  Pulsed laser energy can also be utilized to ablate thin films from substrates, exposing underlying chemistries.  Alkanethiol-based self-assembled monolayers were patterned with a line resolution down to 20nm by coupling a UV laser to an NSOM, which was used to oxidize the alkanethiol, thereby weakening its attraction to the underlying gold substrate.[35] The original SAM was displaced with a new alkanethiol with a different terminal moiety to create activated regions for subsequent biomolecule tethering.  However, as this technique depends on a system coupled to a scanning probe, it suffers from the same aforementioned low throughput and scan area limitations as other scanning probe based lithographies, especially considering that parallel cantilever arrays have not been developed for this technique.

*Electron beam lithography*

The high resolution of scanning electron microscopes has been utilized as another powerful serial writing process in the nanoscale patterning of biological molecules.  Bombarding a surface with a stream of electrons can both ablate polymeric materials as well as alter the charge properties of the surface.  This allows a wide range of materials to be chemically functionalized, topographically altered, or used as resists for further modification of underlying substrates, but requires the materials to be stable in ultra high vacuum.  Throughput is relatively high compared to other serial writing processes, as patterns can easily be programmed, and the scan limits are typically on the order of millimeters.

E-beam lithography can be used to generate both spatially distributed topography and chemistry. In one methodology, a PEG terminated silane-based monolayer was ablated from a

surface, exposing the substrate for further reaction.  DNA arrays with a resolution of 300nm were generated by covalent coupling via an aldehyde terminated silane, which could also be utilized to attach other biomolecules.[36] A similar method involved e-beam ablation of a fluorinated silane monolayer and subsequent reaction of an amine terminated silane to the exposed substrate, which created 500nm biotin functionalized spots.[37] PMMA resists have also been used to create selectively exposed substrates for further functionalization with biomolecules on silicon with a resolution of 50nm[38, 39] and titanium down to 200nm[40, 41].

E-beam lithography has also been used to create ordered nanotopography, including cliffs and arrays of pits and pillars.  Photoresist was patterned on a titanium coated silica substrate and eventually etched to create topography in the underlying silica. [42]  These pillared silica substrates were used as both cell culture materials as well as masters to create negative reliefs of the topography in polycaprolactone. Attachment and spreading of both endothelial cells and epitenon fibroblasts was reduced on regular nanotopography, such as pits and pillars. However the cells were found to adhere and align along asymmetrical topography, such as cliffs. E-beam with a compatible resist has also been used to create 70nm ridges on silicon oxide substrates. Topographical feature sizes ranged from 70nm to 2μm, and the effect on human corneal epithelial cell morphology and cytoskeleton were examined. Cells aligned and elongated along the ridges, and groove depth was found to have a more profound effect on cell alignment than the pitch of the pattern. Patterned substrates were also found to limit cell mobility more than "flat" substrates, while cells adhered more strongly to nanofeatured topography.  The size of the ridges also correlated with the size of mature focal adhesions up to 650 nm, above which focal adhesion size remained constant. [43, 44] However, in a subsequent study published by the same group, it was shown that cells would preferentially elongate perpendicular to the ridges when the media was changed from DMEM/F12 to Epilife media for 400nm pitches, implying that both soluble factors and substrate morphology influences cell behavior.[45]

Limiting factors of e-beam lithography are typically the need for a conductive substrate, access to an electron source, and cost.  As a serial process, the trade-off of pattern design freedom is that scale up is an issue.  Surface charging can also hamper the ultimate resolution in the generation of creating nanoscale chemical patterns on certain substrate types.  Specific substrate requirements, the need for processing in an ultra-high vacuum environment, and the necessity of an electron source combine to create accessibility issues for the biological community at large.

### 2.1.3 - Distributive patterning processes

*Imprint lithography*

Imprint lithography uses a nanopatterned rigid master to create a number of masks for large area patterns, similar to microcontact printing.  However, the standard polydimethylsiloxane (**PDMS**) stamps used in microcontact printing are not suitable for nanometer scale resolution. Typically, masters are created using a high resolution patterning method such as e-beam lithography or deep-UV photolithography with specially formulated resists and reactive-ion etching.  Some success has also been generated using existing silicon nanostructures, such as AFM test gratings. For example, after creating an embossed polystyrene master from an AFM grating, PDMS stamps with a "hard" PDMS surface were used in conjunction with high molecular weight dendrimer inks to print lines of 42nm.[15] To generate arbitrary patterns, PMMA is typically hot-embossed from a lithographically defined master to give the

topographical features of the stamp, which can then be further processed to achieve spatially resolved nanometer surface chemistry.  By imprinting a PMMA film on a silicon substrate and etching with oxygen plasma, patterned regions of exposed substrate were created and subsequently bound with a biotin-streptavidin scheme to achieve lines of 75nm.[46]  Extreme ultraviolet interference lithography has also been used to create large distributions of periodic features in a PMMA master with sub 50nm resolution, although the PMMA resist was not completely removed in the developing step, creating pattern inhomogeneities.[47] Using a liftoff technique with a PMMA resist, a biotin functionalized PEG layer has been produced with a resolution down to 100nm.  The background was filled with PLL-PEG to prevent non-specific protein adsorption, creating a useful platform for functionalizing surfaces using the biotin/avidin conjugation system.

A newly emerging contact printing method, termed 'ISP' patterning (ink, subtract, print) uses a topographically featured substrate to "subtract" inked protein from a planar elastomeric stamp.[48]  The only requirement is that the lithographically defined subtracting substrate have a higher affinity for the ink than the elastomeric stamp.  Once proteins are absorbed onto the elastomer, they can be easily stamped onto an oxygen plasma treated silicon or glass substrate. In this manner, a wide arrangement of protein patterns down to ~90nm have been distributed over a large substrate area using a PDMS elastomer and a silicon subtraction master.  Multiple proteins can also be stamped by repeated application of the inking and subtracting steps. However, the background was not backfilled with a protein resistant layer to passive the remainder of the substrate, limiting their use as a cell culture substrate.

Topography has also been patterned using imprint lithography by using the rigid masters to mold a pliable polymer substrate into topographical features, typically by replication molding or hot embossing. Bovine pulmonary artery smooth muscle cells were cultured on PMMA and PDMS surfaces with topographical features with 350nm line width, 700nm pitch, and 350nm height, created by casting the polymer against the rigid imprint master.[49]  Cells were seeded onto the topographically patterned substrates in the presence of serum, and were shown to elongate and align both their bodies and nuclei parallel to these topographies. Decreased BrdU incorporation into the elongated cells suggested a decrease in proliferation on the nanotopographical features.[49] PMMA-based substrates have also been topographically patterned with features 300nm deep and between 100-400nm wide, with spacing between 100-1600nm. After coating with Matrigel, mouse sympathetic and sensory ganglia were cultured to study the effects of topography on axonal outgrowth.  The axons were found to preferentially grow along the tops of the features and aligned with the topography.  Larger axons were found to be less affected by the topography.[50] Nanoscale grooves of 300nm with 300nm depth on polyurethane were created by a combination of x-ray lithography (to create the master) and nanoimprint lithography. [51] Decreasing the pitch of these features from 4 microns to 400 nm was found to decrease both corneal epithelial cell proliferation, as well as long term (after 14 days) corneal fibroblast proliferation.

Imprint lithography has similar advantages to microcontact printing, but the increased resolution places a number of limitations on the physical systems that can be utilized.  Numerous stamps can be molded from a single master, reducing the requirement for clean room or electron beam access.  The stamps can also be easily used to generate distributed chemistry across a cell culture sized substrate with numerous repeats of the same pattern. However, access to an e-beam system or deep UV/LI photolithography capable facility to generate the master is still required,

limiting rapid pattern and design changes. Maintaining nanoscale feature size fidelity requires a fairly rigid stamp such as PMMA, and maintaining conformal contact on a rigid substrate can be difficult if there are substrate/stamp heterogeneities, surface contamination, or substrate surface roughness. This creates limitations on the types of substrates and facilities that can be used to create patterns, limiting access to the biological community.

*Colloidal Lithography*

The lithography techniques addressed above require some form of serial direct writing to create user-defined patterns, which is both time consuming and expensive. As such, generating multiple substrates with large areas of patterns for cell studies is difficult and cumbersome. Colloidal lithography removes the user-specific control of individual features while allowing rapid coverage of large substrate areas with features. Colloids or block co-polymer dispersions can be used to deposit gold nanodots or to create regular, ordered masks for further substrate modification.

In a series of studies that utilized colloidal distributions of 8nm gold nanodots, Arnold *et al.*[52], Walter *et al.*[53], and Cavalcanti-Adam *et al.*[54] examined the limits of focal adhesion spacing required for cell spreading and focal adhesion/actin stress fiber formation, and subsequently analyzed the strength of the binding for various spacings. Arnold *et al.* [52] tethered ligands of c[RGDfK(Ahx-Mpa)] (cyclic peptide linked via the spacer aminohexanoic acid to mercaptopropione acid) to 8nm gold nanodots. These surfaces were designed to limit the binding of one focal adhesion per dot. These "nanodots" were patterned in regular hexagonal close-packed patterns onto glass or silicon surfaces via a block copolymer micelle of polystyrene-*b*-poly[2-vinylpyridine(HAuCl$_4$)$_{0.5}$], where the spacing was controlled through the molecular weight of the copolymer. The surfaces were subsequently passivated with poly(ethylene glycol) (**pEG**) chains. MC3T3-osteoblasts, REF52-fibroblasts, and B16-melanocytes were cultured on the patterned nanodots for 12-24 hrs and were stained for focal adhesion kinase, actin, and vinculin. At spacing below 73 nm cells appear spread with well formed vinculin clusters and actin fibers, whereas above 73 nm actin fibers and vinculin had little apparent order. The authors attributed this cutoff to the fact that when the individual RGD molecules were spaced above a minimum clustering distance of 58nm, focal adhesions were not able to adequately cluster for activation.

In a later study, Walter *et al.* probed the surface bound cells with magnetic tweezers in order to measure the force required to detach the focal adhesions. Using the substrates described above with spacing of 50-300nm, rat embryonic fibroblasts were plated at various time scales (up to 10min). Subsequently, epoxy coated paramagnetic beads designed to covalently attach to free amine groups on a cell surface were pulled on by magnetic tweezers to measure adhesion forces of the cells. [52] It was also found that lamellipodia extension velocity, focal adhesion turnover, and cell motility were all affected by the underlying peptide density presented on the gold nanodot surfaces.[54] These gold nanodot distributions have also been combined with standard photolithographic or e-beam lithographic lift off techniques to create localized micrometer patterns on substrates with nanometer features.[55]

A variation of this theme exploited charged latex spheres that were electrostatically distributed across a thin gold layer on a silicon or quartz substrate to create a colloid mask. The gold was then etched with an argon ion beam, creating an array of 124nm gold disks that were subsequently reacted with an alkanethiol SAM and crosslinked to laminin. A PLL-g-PEG

copolymer was adsorbed onto the exposed silicon substrate as a passivating layer.[56, 57] Nanospheres have also been used as a colloidal mask to create 118nm diameter lysozyme spots on a silane background. A reactive carboxylic acid silane was deposited on a silicon surface, followed by deposition of the colloid array as a mask. The carboxylic acid on the exposed region was then reacted with a PEG terminated silane to create a non-fouling background before the nanospheres were removed in an ultrasonic bath. The newly exposed carboxylic acids were then coupled to lysozyme to create regions of protein patterns.[58] Arrays of regularly patterned protein spots around 200nm have also been created on titanium dioxide and silicon dioxide substrates using similar techniques,[59] as well as polyacrylamide hydrogels.[60]

These distributed techniques are relatively inexpensive compared to serial writing methods and can cover large areas of substrate quickly and effectively, with varying degrees of homogeneity depending on the system. However, the specific feature distribution is not directly controlled by the user, largely depending on the polymer physics of the system employed. As these methods depend on surface distribution of molecules, colloidal lithography is typically limited to regular geometries such as hexagonal or square distributions of the colloidal bodies, or irregular distributions with average spacings depending on molecular weight of the polymer spacers. To create single cell or locally distributed chemistries on the length scale of multiple cells, colloidal lithographic techniques must be combined with a micropatterning or photolithographic approach, and other potentially useful patterns, such as gradients of feature pitch or varying feature size on a single substrate are unachievable.

### 2.1.4 - Conclusions and Future Direction

A number of surface modification techniques have been described for the creation of nanoscale patterns of peptides, proteins, or surface topography for biologically relevant studies. Nanoscale variations in topography have already been shown to effect neuronal axon growth, and fibroblast and endothelial cell proliferation. Furthermore, patterns of evenly spaced single cell adhesion ligands have shown the effects of integrin spacing on focal adhesion complex formation and cell attachment. However, none of these approach an ideal nanopatterning technique, which would allow creation of user designed spatial distributions of topography or chemistry independently, over large areas. Work by Spatz *et al.*[55] involving micropatterning block copolymer distributions of gold nanodot focal adhesion sites has demonstrated large patterned regions with controlled nanometer scale features that serve as the current state of the art for cell-substrate interaction studies. However, this technique still suffers from a lack of direct control over focal adhesion placement. These types of distributed techniques, when combined with a liftoff or photolithographic process could generate substrates useful for single cell studies with a high degree of throughput and reproducibility. Nanoimprint lithography can be used to create large nanopatterned areas for cell studies and holds promise to effectively transfer stamped molecules, but requires a large amount of optimization and difficult characterization to ensure that the molecules are effectively transferred to the sample surface.

Table 2.1. Overview of commonly used nanopatterning techniques.

| Patterning Technique | Resolution | Cost | Access | Scale-up | User defined features |
|---|---|---|---|---|---|
| Scanning probe lithography | 10nm | ++ | +++ | ++ | ++++ |
| Near-field scanning optical lithography | 10nm | - | + | + | ++++ |
| Electron beam lithography | 50nm | - | - | +++ | ++++ |
| Laser ablation lithography | 70nm | - | + | ++++ | ++++ |
| Liquid Immersion photolithography | 45nm | - | - | ++++ | + |
| Imprint lithography | Varies[a] | +++ | ++++ | ++++ | +++ |
| Colloidal/block copolymer lithography | Single integrins | ++++ | ++++ | ++++ | + |

a- requires the use of another patterning technique to create a master.

Collectively, the critical limitation to the generation of nanoscale cell ligand patterns is the lack of availability of many of the techniques to biological researchers. The equipment required for generation of nanoscale patterns is highly specialized, such as e-beam sources, atomic force microscopes, or near-field scanning optical microscopes. The aforementioned techniques have focused on developing methodologies for patterning various biomolecules for future cell studies, but the number of cell studies in the literature is limited, indicating that scale up of a many of these techniques is difficult. Colloidal or block co-polymer lithographies are the most accessible and do not suffer from scale up issues, but do not allow the user full control of the patterns generated, thereby limiting the types of biological questions that can be investigated. Therefore, development of a technique allowing for user controlled, repeatable, and easily scalable nanopatterns of surface chemistry will be critical in studying cell-material interactions.

## *2.2 - Laser ablation*

As described above, a wide range of patterning techniques center around modification of materials with light, including standard photolithography, light-based chemical conjugation and polymerization, and laser machining of a wide range substrates. A number of these techniques, most notably photolithography, are used in the semiconductor manufacturing industry to build up structured integrated circuit layers. As demand for higher circuit density has increased, patterning processes have been developed to create increasing features on a surface.

The diffraction limit of a given optical system presents a maximal physical limitation on the achievable resolution based on the wavelength of processing light and the optics involved. The limit is related to the diffraction pattern a beam of light moving through an aperture or around a solid object. For a circular aperture of or focused lens, a pattern known as an Airy disk forms, consisting of a bright central circular area surrounded by concentric rings of alternating light and dark areas. The pattern is caused by destructive interference of the propagating waves making up the beam. As a result, the maximum resolvable distance of an optical system, known as the diffraction limit, is defined as:

$$d = 1.22\lambda N \approx \frac{1.22\lambda}{2NA},$$

<div align="center">Equation 2.1</div>

where $d$ is the radius to the first null of the Airy disk, $\lambda$ is the wavelength of light, $N$ is the f number of the lens, and $NA$ is the numerical aperture .  However a wide range of methods exist to lower or bypass the diffraction limit, including increasing the numerical aperture of the processing objective, altering processing environments to reduce the refractive index (liquid immersion lithography), or decreasing the wavelength of the processing light (deep UV lithography).  While these are incremental extensions of previously existing technologies to allow for use of already well developed facilities in the IC industry, the startup and process development costs required for small research labs and the biological community present a significant barrier to entry.

For our particular application, we chose to ablate an ultrathin polymer film with femtosecond laser pulses to create exposed islands for protein adsorption. Material ablation is typically attributed to either a photochemical or photothermal degradation mechanism, with the mechanism depending on a wide range of factors, including the laser fluence, pulse width, and wavelength, as well as the chemical and physical makeup of the ablation target.[61]  For processing of relatively delicate polymer thin films (especially when compared to metal films or solid dielectric materials), minimizing thermal and mechanical stress in both the polymer film and underlying substrate is paramount.  The use of femtosecond laser pulses can reduce both the feature size in transparent films as well as reduce collateral damage in the film due to its dependence on a multiphoton ionization process to initiate the dominant ablation mechanism, generating more consistent ablation results.[62, 63]

As our application relies on far field ablation of an ultrathin, transparent polymer layer (polyethylene glycol/polymethylmethacrylate co polymer) on a transparent dielectric (fused quartz) using focused femtosecond laser pulses, generating nanoscale patterns requires surpassing the diffraction limit.  Ablation dynamics are material dependent, therefore the following section will focus on the ablation mechanism for our particular application.

For ablation with a given far field based optical system, there exists a limit to the smallest focal spot that can be obtained as defined by the diffraction limit described above.  A beam with a Gaussian distribution, such as the titanium-sapphire used in this work, will create circular features based on the following general relationship:[64]

$$D^2 = 2w_0^2 \ln\!\left( F_0 \middle/ F_{th} \right),$$

<div align="center">Equation 2.2</div>

where $D$ is the feature diameter, $w_0$ is the beam spot radius, defined as where the beam drops to $1/e^2$ of the peak intensity, and $F_0$ and $F_{th}$ are the beam fluence and ablation threshold fluence, respectively.  Since the beam is not evenly distributed across its cross section, and ablation is a threshold process, extremely small features can be ablated using a tightly focused beam and at processing energies slightly above the ablation threshold fluence, schematically demonstrated in Figure 2.1.
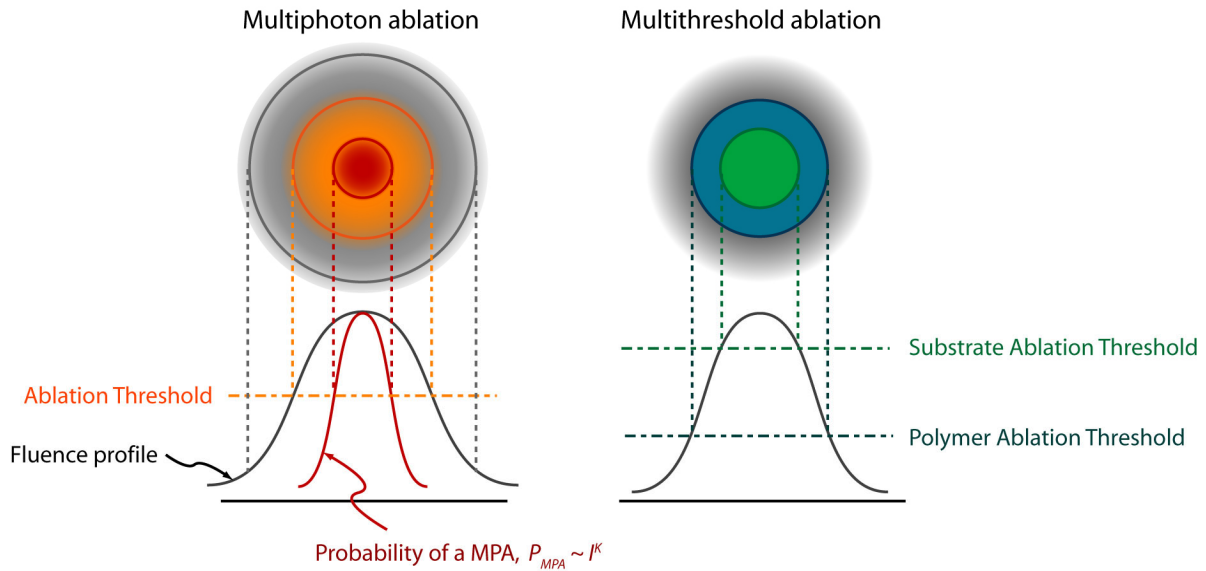
Figure 2.1. Effect of multiphoton ablation and layer substrates with different ablation thresholds on ablation characteristics (figure adapted from [64])

    The threshold behavior of ablation is inherent in the mechanism by which material degradation begins. For ablation to occur, the fluence intensity must surpass the energy volume density of the material, resulting in an ablation area present only in the highest energy area in the center of the beam spot, and resulting in the relationship described above. The dominant mechanism of energy adsorption from the beam depends on the opacity of the material at the processing wavelength: typically linear adsorption for opaque materials and non-linear for transparent. In the case of an opaque material, the energy from a photon imparts sufficient energy to promote an electron from the valence to the conduction band, then the electron energy is transferred to the lattice, causing the material to boil and/or vaporize. The duration of this energy transfer in the material is known as the electron-phonon relaxation time, and is responsible for the differences in ablation characteristics between ultrashort (fs) and longer (ps to ns) pulse processing.

    For transparent materials, the process is more complex as there is minimal linear interaction between the electrons in the material and the beam. As the individual photons in the beam do not have sufficient energy to cause an electron to jump from the valence to the conduction band, multiple photons must impart energy to the electron nearly simultaneously to cause it to jump the band gap. Following multiphoton ionization, energy is again transferred to the lattice causing decomposition. A second ionization method, termed avalanche ionization, can also play a role in photon/material interaction.[63] In this manner, seed electrons already present in the conductance band absorb photon energy linearly and are bumped to increasingly higher energy states. Collisions between these higher energy electrons can cause secondary electrons to move from the valence band to the conduction band if the energy is sufficient (i.e. the energy between the electron and the conductance band is greater than the energy between the conductance and the valence band.) This newly promoted electron can subsequently linearly absorb energy from the beam and recruit other valence electrons in the same manner, creating a highly ionized region on the surface susceptible to ablation events. The seed electrons for this process can either come from electrons in the conductance band due to a multiphoton process or electrons trapped in impurities in the material.

Probabilistically, a higher photon density increases the chance of a multiphoton event occurring and is proportional to the fluence intensity raised to the power of the number of photons required to bridge the bandgap, or:[65]

$$P(I)_{MPI} = \sigma_k I^k,$$

Equation 2.3

where $P(I)_{MPI}$ is the probability of a multiphoton event, $\sigma_k$ is the multiphoton absorption coefficient, $I$ is the intensity of the beam, and $k$ is the number of photons needed to bridge the bandgap. As this scales in a power relation with the fluence intensity, a further reduction of the area in the center of the beam exceeding the ablation threshold is achieved.

It should also be noted that pulse width plays a factor in the overall repeatability and feature quality of the ablated features, and is related to the electron-phonon relaxation time. The relaxation time is typically on the order of picoseconds, therefore longer pulses (ns) are still exiting the sample as the energy is transferred from conductance band electrons to the material lattice and the subsequent ablation, causing both events to occur simultaneously. This causes a high degree of melt and large heat affected and shock affected zones in the ablated feature. However, femtosecond laser pulses are no longer illuminating the sample during the energy transfer step, meaning electron excitation and energy transfer occur in two separate phases, minimizing the amount of thermal and mechanical shock imparted to the substrate. The minimization of collateral damage around the ablated features is critical for delicate polymer thin films that could easily be damaged by excess heat or mechanical stress.[66]

Other processing techniques have been reviewed in the previous section, as well as their strengths and weaknesses. In the realm of nanotechnology, laser nanomachining provides a number of distinct advantages over existing patterning methodologies. As a serial writing process, laser ablation has similar advantages and limitations to e-beam lithography. The process can be computer controlled using a PC connected shutter and motorized stage to allow for rapid pattern customization, increased throughput, and the ability to create any user defined pattern. Creating large numbers of substrates for an extensive biological study can be time consuming and costly. However, laser nanomachining can be done on the bench top and does not require specialized substrates or processing environments. Patterns can be changed rapidly during processing, without the need to remake expensive photomasks or masters, and patterns are not constrained to regular or random patterns as in colloidal lithography.

The same basic concepts that are employed in laser micromachining setups can be converted into a nanoscale patterning system, with the following caveats. Due to tight depth of focus requirements, the stage must be flat on the nanoscale over the length of the sample and must be isolated from vibrations or other physical displacements. To pattern the size and quantity of samples necessary for large scale biological experiments, the stage must also have both high translation speed and movement limits. During translation, the stage must also have minimal movement in the Z-axis perpendicular to the substrate, such that the sample will stay in proper focus during the entire patterning process. An autofocus enabled processing setup could also be used to correct for stage motion, as well as for patterning non-planar substrates or medical implants.

For a serial process, laser ablation nanolithography has the potential to develop into a highly controllable, easily scaled writing process that would allow researchers complete control over

pattern design. This technique has a number of practical advantages over the widely used techniques of e-beam and dip-pen lithographies. Although it is a serial process, the high pulse rate of commercially available laser systems (kHz-MHz) places the throughput limitation on how quickly the sample can be rastered. The lack of substrate requirements or specialized processing environments means a wide range of materials can be processed, and that access would not be a issue to the biological community if nanoscale laser machining setups become commercially available.

## 2.3 - Cell mechanics

Interaction with their surrounding microenvironment drives a wide range of cellular behavior, including gene expression, protein production, cell morphology and differentiation, and apoptosis.[1-7] Cells are able to sense both mechanical and chemical cues in the external environment, and the complex interplay between physical forces and chemical stimuli drive both the detection and response to these cues. Receptor ligands on the cell surface allow for chemical recognition of specific amino acid sequences on the proteins that comprise the extracellular matrix (**ECM**), cytoskeletal contraction lets the cell "feel" the stiffness of its surrounding matrix, soluble chemical signals are internalized to sample the surrounding fluid, cell-cell junctions allow for direct communication between adjacent cells. All of these interactions can have profound effects on how a cell responds and behaves in a given microenvironment.

Due to the sheer number of signals presented to a cell on even the simplest type of cell culture substrate, designing completely synthetic microenvironments can be exceedingly complex. Here, we seek to develop a nanopatterning platform that would allow for direct control the interaction of the cell and the substrate. Such a patterning scheme would allow for greater control of peptide ligand density, adhesion domain cluster size, and spatial arrangement of adhesion domains. These variables are deemed critical to cell adhesion, spreading, and morphology, which in turn can influence proliferation, differentiation, and gene expression.[5-10] A range of studies already exist exploiting spatially resolved chemistry on a micrometer length scale, but these studies are limited due to the inability to independently control ligand input to the cell via the adhesion domains presented on the surface. For example, in a previous micropatterning study, it was found that cell spreading also correlated to the spreading and flattening of the of the nucleus. Both spreading of the cell and nucleus correlated to increased collagen production in rat primary bone derived cells, suggesting a possible mechanical link between external adhesion ligands to the nucleus.[67] However, this result is confounded by the fact that cells with higher spread areas were also exposed to an increased ligand density on the surface, preventing mechanistic analysis of the effect of both ligand density and cell spread area on function.

A surface with nanoscale control of adhesive ligands presented from a surface would provide biological researchers the means to independently control ligand density, pitch, and clustering, making mechanistic studies of these variables possible. For cell adhesion to a substrate, large protein plaques known as focal adhesions provide chemical recognition of the external ECM, anchor points for the cytoskeleton, and a pathway for outside in signaling of the cell, making them a critical access point on the exterior of the cell. Initial adhesion to the ECM depends on the interaction between a class of transmembrane proteins called integrins on the cell surface and specific recognition sites present on the ECM molecules.[68]

Integrins are made of a combination of one α and one β subunit, and the combination of the two subunits determines which biorecognition site on the ECM molecule to which the integrin will bind. Mammalian genes code for 22 α and 8 β subunits, so a wide variety of specific interactions possible.[69] Following activation by binding to the ECM, integrins cluster and recruit other adaptor and associated proteins, including talin, paxillin, vinculin, which serve as an initiation site and organization center for actin filament formation. The result of integrin clustering is the conglomeration of external proteins, internal proteins, and actin filaments, generating large focal adhesion complexes and actin stress fibers. Integrin activation also typically phosphorylates focal adhesion kinase, which eventually merges into the ERK/MEK pathways, critical to cell cycle regulation.

Independent of the chemical signaling cascade initiated by integrin binding and activation, the mechanical state of the cell has also been implicated in the regulation of protein production and stem cell differentiation.[70, 71] Mechanical forces are transmitted from the external environment to the nuclear envelope via actin filaments, stress fibers, and other cytoskeletal elements, which provide a continuous mechanical network throughout a cell. It is hypothesized that tension on the cytoskeletal elements can then impart forces on nuclear matrix proteins (NMPs) that regulate nuclear architecture and DNA structure. Deformation of the nuclear architecture could allow easier access to the DNA for transcription factors and promoter sequences, resulting in changes in protein production and cell behavior.[72]

As integrin activation and focal adhesion development are an integral first step in both chemical signaling pathways and mechanical transduction within the cell, control over the size, placement, and density of adhesive ligands will be critical to mechanistically investigating how these variables influence cell behavior. Nanopatterned surfaces, specifically surfaces designed to spatially control surface chemistry and cell adhesive ligands on the length scale of proteins themselves, will be critical in decoupling variables such as ligand density, projected cell area, and focal adhesion clustering influence cell fate.

# Chapter 3 - Fabrication of a non-fouling, low roughness, tunable thickness brush layer

## 3.1 - Introduction

The first step in generating our nanopatterned cell culture platform was the development of a polymer layer with the following desirable properties: tunable thickness, low surface roughness, resist protein and prevent cell adhesion. The first two characteristics were critical for pattern generation and characterization with respect to laser processing at the nanometer length scale, as high surface roughness prevented visualization of the surface features using scanning probe microscopy and resulted in difficulty in proper laser focusing. Tunable thickness, and the ability to generate a polymer layer of consistent thickness, was necessary for achieving repeatable ablated feature geometries, as the ablation process is a volumetrically controlled process. Protein adsorption resistance allowed us to create regions on the surface that were "cell adhesive" by ablating the polymer away and exposing the substrate beneath decorated with appropriate cell adhesion motifs.

Initial attempts at patterning on a crosslinked polyacrylamide-co-polyethylene glycol interpenetrating polymer network (**IPN**) that had previously been developed and characterized in our lab were unsuccessful.[73] The IPN was synthesized by a free radical polymerization, whose uncontrolled nature resulted in a large degree of surface roughness and a crosslinked polymer layer with a 20 nm dry thickness, but would swell to hundreds of nanometers upon submersion in aqueous solutions. In order to provide a smooth and consistent surface to pattern, the reaction scheme was changed to a controlled or "living" radical polymerization.

### 3.1.1 - Surface initiated atom transfer radical polymerization

Atom transfer radical polymerization (**ATRP**) is a controlled or living radical polymerization that generates polymers with a low polydispersity index (**PDI**) and a relative slow growth rate. When surface initiated, (**SI-ATRP**) the relatively slow rate of reaction allows for the thickness of the layer to be tightly controlled and the low PDI results in production of a low surface roughness, both advantageous for our patterning scheme. As a radical polymerization, a wide range of monomers and macromonomers can be polymerized in various arrangements and geometries. ATRP has been used to make bulk polymers, block and random copolymers, crosslinked gels, brush and star polymers, as well as surface modifying nanotubes, nanoparticles, gold self assembled monolayers, and silicon and titanium oxides.[74-79]

*ATRP Reaction scheme*

Atom transfer radical polymerization depends on the reversible radicalization on a growing polymer chain by an oxidizable metal ion in solution, shown schematically in Figure 3.1:
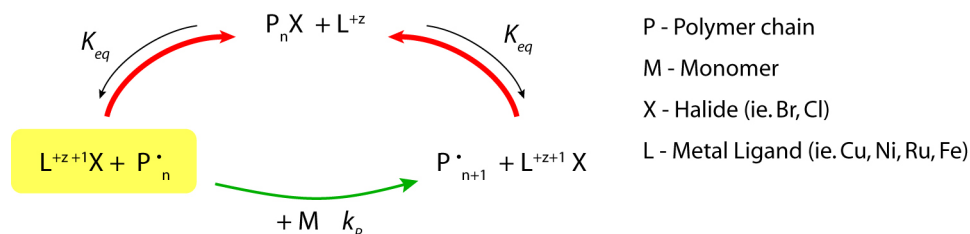


Figure 3.1. Schematic representation of the basic ATRP mechanism.

The notable components of the ATRP scheme are the metal-halide complex that is able to change oxidation state and the reversibly abstractable halide group on the initiator/growing polymer chain.  During the reaction, the metal ion is able to change oxidation states and remove the halide form the capped polymer chain, producing a radical at the chain terminus.  This "activated state" is highlighted in yellow in Figure 3.1, and only persists transiently. From this state, the radical then competes for two possible reactions: should an oxidized metal-halide complex encounter the radical, the radical production step is reversed (red arrow), recapping the chain with a protective halide.  A monomer encountering the radical, however, will cause chain growth (green arrow), adding a monomer while otherwise preserving the chains activated radical state. Following addition, the chain again can undergo either a halide recapping or a monomer addition, depending on which species encounters the radical first.  For the reaction to proceed in a controlled manner, the recapping reaction must be heavily kinetically favored, such that at any given time only a limited number of radicals are present concurrently, greatly reducing the chance for undesirable chain transfer or coupling termination mechanisms.

A wide range of polymers, halide, and metal ligands have been employed in ATRP reactions. Polymerizations of styrene, acryl, methacryl, and acetonitrile have been demonstrated, with copper or nickel as the most prevalent metal ions and chlorine or bromine typically used as removable halide groups.[80]  For reactions involving copper, a bidentate nitrogen containing ligand is also employed as a pi-accepting, chelating agent that complexes with and stabilizes the copper ions in solution, most commonly 2,2'-bipyridine or an analogous derivative.  It has been empirically shown that reaction mixtures containing a 2:1 molar ratio of ligand to copper maximizes chain growth rate, suggesting that two molecules of the nitrogen containing ligand coordinate to stabilize a central copper ion in the polymerization solution. [81, 82]

*Reaction Kinetics*

The nature of the ATRP mechanism allows for a number of assumptions to be made regarding the kinetics of chain growth.  Writing the reaction mechanism in more conventional terms yields:

Initiation:

$$IX + L^{+z} \xleftrightarrow{K_{eq}'} I^\bullet + L^{+z+1}X$$

$$I^\bullet + M \xrightarrow{k_p'} P_1^\bullet$$

Propagation:

$$P_n X + L^{+z} \xleftrightarrow{K_{eq}} P_n^\bullet + L^{+z+1}X$$

$$P_n^\bullet + M \xrightarrow{k_p} P_{n+1}^\bullet$$

Termination:

$$P_n^\bullet + P_m^\bullet \xrightarrow{k_t} P_{n+m} + (P_n + P_m)$$
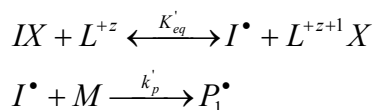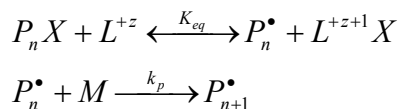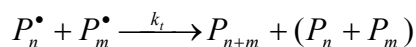
Equation 3.1

Where *I*, *P*, *M*, *L*, and *X* represent initiator, polymer, monomer, metal ligand, and halide concentrations, respectively. In order for the ATRP reaction mechanism to occur properly, the equilibrium reaction between the halide capped and radical presenting polymer chain must be established rapidly, necessary for achieving low PDI polymers and consistent reaction kinetics. Once this occurs, unwanted termination reactions are virtually eliminated due to the low number of chains containing a free radical present on the surface at a given time. Initiation reactions are relevant during the first moments of the polymerization, and if similar chemistries are used for both the initiator and the monomer, the rate constants should be similar.

Making the fast equilibrium approximation, and assuming minimal termination reactions occur, the reaction kinetics simplify to:

$$R_p = k_p[P^\bullet][M] = k_p K_{EQ}[I]\frac{[L^{+z}]}{[L^{+z+1}][M]}$$

Equation 3.2

where

$$K_{eq} = \frac{[P^\bullet][L^{+z+1}X]}{[L^{+z}][PX]},$$

and $R_p$ is the rate of propagation, $k_p$ is the rate constant of propagation, $K_{eq}$ is the equilibrium constant for propagation, and *I*, *P*, *M*, *L*, and *X* represent initiator, polymer, monomer, metal ligand, and halide concentrations, respectively. Thus, the rate of polymerization is proportional to the metal ligand, monomer, and initiator concentration. Initiator concentration and metal ligand should stay constant under equilibrium conditions, therefore the length of the polymer chain should grow nearly linearly with time assuming minimal monomer depletion relative to the initial concentration.

The controlled nature, slow reaction kinetics, and lack of undesirable coupling terminations during the ATRP reaction results polymers with a very low polydispersity, typically PDI's of around 1.1 are observed.[83] The requirement for a halide leaving group to be present on a molecule undergoing polymerization makes this technique particularly effective for surface polymerizations and block copolymerizations. As radicals are only generated from halide

containing initiators and the growing chain can be capped to preserve its reactivity, many interesting configurations can be imagined based on initiator design. Star copolymers can be created by creating initiators with multiple halides around a central core, wide varieties of substrates can be modified provided a heterobifuctional crosslinker can be synthesized with a halide leaving group end and a substrate reactive end, and samples can be transferred from one monomer solution to another to easily create block copolymers. The ease at which the halide group can be removed also allows for the growing chains to be terminally functionalized; for example, providing a potential site for bioconjugatable species to be added to the polymer.

## 3.2 - Methods

### 3.2.1 - Silane modification

*Silane synthesis*

For the SI-ATRP synthesis, a silane-based initiator was synthesized by adding 2-bromo-2-methyl propionyl bromide dropwise to a solution of (3-aminopropyl)trimethoxysilane (Gelest) and triethylamine in anhydrous dichloromethane. After reacting for 14hrs in a nitrogen environment, the solution was filtered, rinsed twice with dilute hydrochloric acid, once with water, and then dried with anhydrous calcium sulfate. The desiccant was filtered off and the resulting clear or yellowish solution was purified *in vacuo*. The 3-(trimethoxysilylpropyl)-2-bromo-2-methylpropanamide structure was verified with proton NMR in CDCl$_3$. $^1$H peak shifts are reported in parts per million (ppm) relative to TMS. $^1$H NMR (300 MHz, CDCl$_2$): $\delta$ 6.88 (1H, s), 3.57 (9H, s), 3.30 (2H, dd), 1.96 (6H, s), 1.69 (2H, m), 0.67 (2H, t).

*Silane deposition*

Prior to silane deposition, all samples were cleaned by sonicating in water, acetone, hexanes, acetone, and water for 10 minutes each, blown dry with nitrogen, and oxygen plasma treated for 3 minutes. For the silane deposition from methanol, oxygen plasma treated quartz or glass pieces were immersed in 1% silane solution, 4% water (ASTM Type I reagent grade water; 18.2 M$\Omega$-cm, pyrogen free, endotoxin < 0.03 EU/m), and 95% methanol solution with 1mM acetic acid for 10 min, rinsed thrice with methanol, and baked for 30 minutes at 110ºC. For deposition from toluene, a 1.25% (v/v) solution of allyltrichlorosilane in anhydrous toluene was prepared in a glovebox, and plasma treated samples were immersed in the solution for 5 minutes, rinsed thrice with toluene, and baked in at 110ºC for 30 minutes.

### 3.2.2 - Polymer synthesis

*IPN synthesis*

A polyacrylamide-co-polyethylene glycol IPN was synthesized as described previously. Allyltrichlorosilane or methacryloxypropyltrimethoxysilane was deposited either from methanol or toluene as described above. Following silane modification, substrates were photopolymerized in a two step reaction. The acrylamide (**AAm**) prepolymer solution was mixed by combining 0.1485 g/mL acrylamide, 0.0015 g/mL bis-acrylamide (**BIS**), and 0.03324 g/mL camphor quinone (**CQ**) in acetone that had been bubbled w/ nitrogen for 30 minutes. The solution was sonicated until completely dissolved, pipetted over the samples and allowed to rest for 5 minutes, followed by 20 minutes of photopolymerization under blue light in a Rayonette photoreactor. The samples were rinsed with acetone and water, sonicated in water for 30 minutes, and dried under nitrogen. The PEG layer was the synthesized in an identical manner to the AAm layer,

using 0.02 g/mL polyethylene glycol methacrylate (MW 1000), 0.01 g/mL BIS, 0.03324 g/mL CQ in deoxygenated methanol.

*PEG brush layer synthesis*

PEG brush layers were synthesized by reacting a surface grafted with the SI-ATRP silane with solution containing poly(ethylene glycol) monomethacrylate monomer (PolySciences) in a deoxygenated environment. The SI-ATRP synthesis was carried out as described previously.[84] Briefly, 1.0 mmol copper(I) bromide, 2.0 mmol bipyridine, 0.3 mmol copper(II) bromide, and 25 mmol of the monomer poly(ethylene glycol) monomethyacrylate (side chain MW=200) were dissolved in 12 mL of methanol and 3mL of degassed water. The dark red solution was bubbled with nitrogen for 30 minutes and sonicated until all materials were dissolved, before being poured over the samples. The reaction proceeded for various times to give desired thicknesses, under nitrogen flow before the samples were removed, rinsed copiously with methanol and dried under a nitrogen stream.

### 3.2.3 - Characterization

*Quartz crystal microbalance with dissipation (QCM-D)*

After depositing a silane initiator as described above onto a silicon dioxide coated QCM-D crystal, a solution of poly(ethylene glycol) monomethacrylate, methanol, and water was pumped through the chamber with a peristaltic pump at 0.05 mL/min until a stable baseline was achieved. The solution was then switched to the reaction mixture containing the copper(I) bromide, copper(II) bromide, and bipyridine initiator system, at which point the reaction was monitored *in situ,* at room temperature. The same molar ratios were used as described above. Following the reaction, the system was flushed with the PEG, methanol, and water mixture to remove the catalyst system, and the changes in frequency and dissipation were recorded.

*X-ray Photoemission spectroscopy (XPS)*

All XPS spectra were taken on a Surface Science Instruments S-probe spectrometer with a monochromatic Al Ka X-ray and a low energy electron flood gun for charge neutralization. X-ray spot size for these acquisitions was on the order of 800 μm. Pressure in the analytical chamber during spectral acquisition was less than $5 \times 10^{-9}$ Torr. Pass energy for survey spectra (composition) was 150 eV and pass energy for high resolution scans was 50eV. The take-off angle (the angle between the sample normal and the input axis of the energy analyzer) was 55º (55 degree take-off angle, ~ 50 Å sampling depth). The Service Physics ESCAVB Graphics Viewer program was used to determine peak areas, to calculate the elemental compositions from peak areas and to peak fit the high resolution spectra. The binding energy scale of the high-resolution C1s spectra was calibrated by assigning the hydrocarbon peak in the C1s high-resolution spectrum a binding energy of 285.0 eV.

*Atomic Force Microscopy (AFM)*

Atomic force microscopy images were taking on a Bioscope I microscopy system in tapping mode. Samples were cleaned by sonication for 10 minutes in 2% Hellmanex (Hellma), a filtered surfactant based detergent for 10 minutes, rinsed with UPW, and dried under a gently stream of nitrogen before scanning.

### 3.3 - Results

#### 3.3.1 - Decreasing surface roughness

Initial experiments were undertaken using a previously developed polymer system, an interpenetrating polymer network of polyacrylamide and polyethylene glycol (**IPN**) that has been show to provide robust resistance to non-specific protein adsorption, as well as providing the underlying structure necessary for modification of the modulus through the base acrylamide layer.[73, 85, 86]  However, we observed surface roughness on the same length scales of the features we hoped to generate, likely due to the fast reaction kinetics of the free radical polymerization scheme and initiation in the bulk of the polymer solution.  As our major characterization tool was atomic force microscopy (**AFM**), a technique that images topographical features, reducing surface roughness on our samples was paramount.

AFM scans were taken after each step in the IPN polymerization, namely after silane deposition, AAm polymerization, and PEG polymerization.  Using the procedure previously developed in the lab, an allyltrichlorosilane (**ATC**) was deposited onto the surface from toluene in a 1% solution, which resulted in a hemispherical drops remaining on the surface of the substrate that could contribute to surface roughness, as shown in Figure 3.2a.  The suspected mechanism for this was that upon silanization, the chlorosilane groups on the ATC molecule hydrolyze into a reactive silanol, generating an amphiphilic molecule capped with a hydrophilic silanol and a hydrophobic allyl at opposite ends. This results in aggregated drops or micelles forming in toluene and despositing onto the surface.  To improve this, two new silanes were deposited that more closely mimicked the polymer chemistry seen in the IPN. 3-(acryloxypropy)trimethoxyl silane (Figure 3.2b) and methacryloxypropyltrimethoxysilane (**MTMS**) (Figure 3.2c) deposited from a 5% silane, 1% water, and 94% methanol solution, with 1mmol of acetic acid to lower pH provided a low surface roughness deposition on glass (Figure 3.2c). Of the three silane deposition methods, MTMS deposited from methanol provided the lowest surface roughness. It should also be noted that the methacrylate terminal group more closely chemically resembles both the acrylate backbone and the methacrylate backbone of the acrylamide and PEG-methacrylate monomers used is the subsequent reaction steps, thus silane deposition from methanol was used for all subsequent experiments.
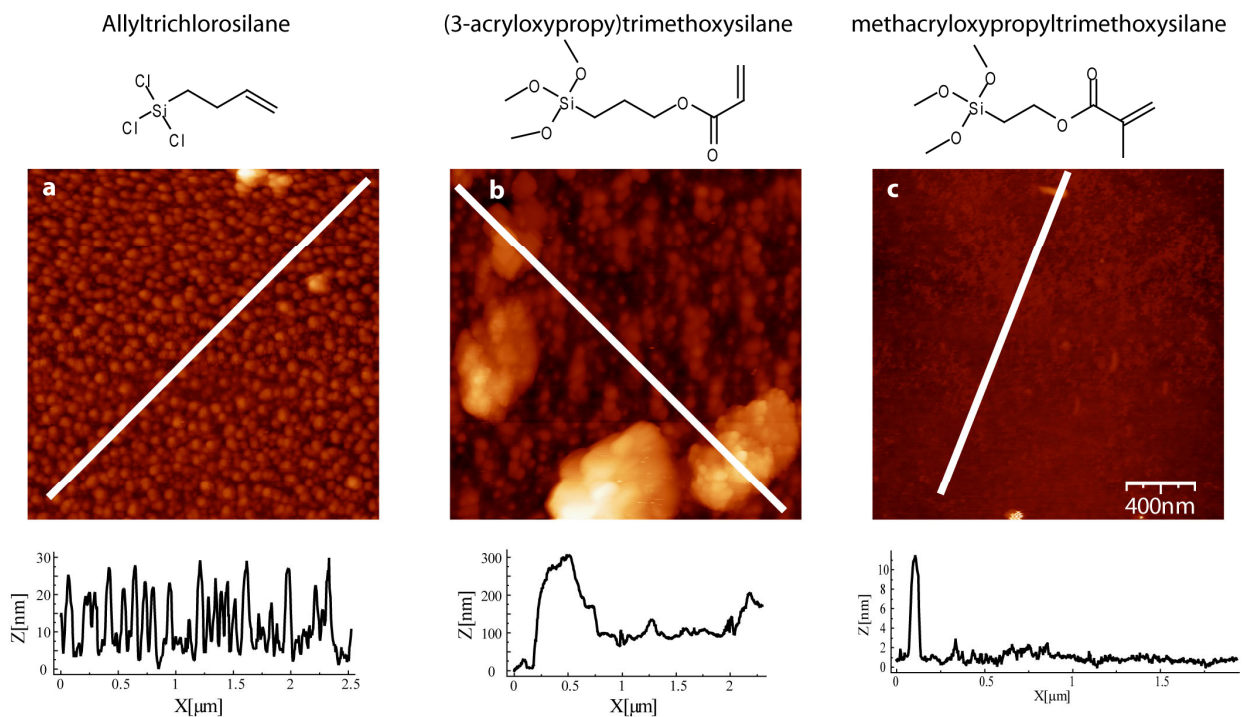
Figure 3.2. AFM scans with cross sections for various silane depositions. ATC deposited from toluene(a) and ATMS deposited from methanol (b) both had surface features exceeding 30nm, while MTMS (c) was largely flat (< 2-3 nm peak to peak roughness).

Following the silane deposition optimization, a high degree of roughness was still observed after the IPN polymerization as shown in Figure 3.3. Looking at each layer individually, the pAAm layer, which comprised the bulk of the IPN, seemed to be providing the bulk of the surface roughness. We initially attempted to alter the reaction conditions to eliminate surface roughness in the IPN layer by changing AAm polymerization time, crosslinker and monomer concentrations, and sandwiching the polymerization between two coverslips, all of which failed in providing a suitable reduction in topographical features. Therefore, another reaction scheme was explored that would provide better control of growth rate and surface roughness.
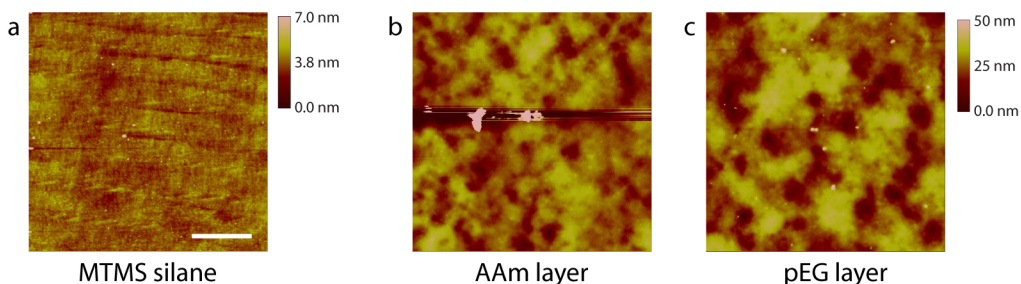


Figure 3.3. AFM scans showing roughness after each synthesis step of the IPN, including silane deposition (a), AAm synthesis (b), and pEG synthesis (c). The majority of the observed roughness occurs following the AAm step (b). (Scale bar = 5 microns)

25

### 3.3.2 - ATRP PEG characterization

*Silane deposition*

Surface initiated ATRP (**SI-ATRP**), a controlled radical polymerization scheme was used to modify the surface of quartz substrates with a non-fouling polyethylene glycol methacrylate (**PEG-MA**) brush layer.[84]  As described above, ATRP provides a high degree of control over the reaction kinetics, and due to the controlled nature a low polydispersity index (**PDI**) is typically observed.[80]  For our initial experiments, a silane initiator was synthesized and deposited on diced quartz substrates, providing polymerization initiation sites localized only at the surface of the substrate.  AFM scans were taken of the surfaces after deposition of the silane from both methanol and toluene to verify that a low roughness surface was maintained, as shown in Figure 3.4.  Deposition of both MTMS and our brominated silane initiator (a & b) both showed an RMS roughness of less than 1 nm.  Deposition of the bromosilane from toluene again showed small aggregates appearing on the surface (c), although the to a lesser degree than the previously studied ATC.
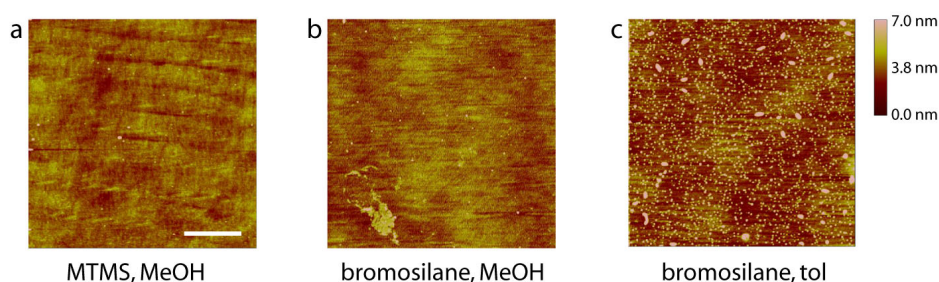


Figure 3.4. AFM scans of deposited silanes.  Methanol deposition of MTMS (a) and the brominated silane initiator (b) had no observable surface features, while bromosilane deposited by toluene formed small aggregated drops. (Scale bar = 5 microns)

*Reaction Kinetics*

For a standard ATRP synthesis, immersion in a prepolymer solution results in linear chain growth from the surface at a rate proportional to the monomer concentration, thus the growth rate should proceed nearly linearly with time.  To verify this, film thickness, growth rates, and surface chemistry were verified using thin film spectral reflectometry, quartz crystal microbalance with dissipation (**QCM-D**), and x-ray photoelectron spectroscopy, respectively.  Initially our SI-ATRP synthesis, our PEG polymerization mixture used the following components: poly (ethylene glycol)$_n$ monomethyl ether monomethacrylate (MW = 200) as a macromonomer, copper(I) bromide and bipyridine as a stabilizer/catalyst system in a 1:2 molar ratio, and methanol and water as solvents.  This reaction mixture yielded a surface modification that had an RMS surface roughness typically around 1 nm or less and provided a robust protein and cell adsorption resistance.  However, the growth rate, and hence the resulting film thickness, did not seem to follow the expected linear growth curve.  Identical reaction conditions and times would result in relatively large variations in thickness, samples polymerized under identical conditions would vary 20 and 45 nm.

Using the standard reaction concentrations of PEG, CuBr, and bipyridine described in the methods section, the polymerization reaction was carried out on a silicon dioxide coated quartz crystal in a QCM-D chamber.  As the QCM-D reaction chamber holds relatively low solution

volume, a peristaltic pump was hooked up to the outlet of the chamber at a low flow rate to pull the reaction mixture through the chamber.  The QCM-D measures changes in frequency and dissipation of the resonance frequency of the oscillation of the quartz crystal.  For a solid, rigid thin film adhered to the surface of the quartz, this is represented by the Saurbrey equation, which simple states that the mass adsorbed is proportional to the change in resonant frequency.[87]  However, for viscoelastic films or swollen polymers the density and viscosity of the bulk fluid, as well as the viscosity, density, and modulus of the film must be taken into account.

For each run, a quartz crystal was cleaned and modified with a brominated silane initiator as described above.  Following loading in the QCM-D chamber, a macromonomer solution consisting of PEG, methanol, and water, but without the CuBr/bipy catalyst system was pumped at a flow rate of 0.05 mL/min to equilibrate the QCM-D frequency and dissipation readings under both flow and the expected bulk fluid density and viscosity readings expected during the polymerization reaction.  After a stable baseline was achieved, the pumped solution was switched to an already prepared solution containing the complete reaction mixture, including CuBr/bipy.  The pump flow rate was briefly increased to rapidly fill the chamber with the polymerization solution, before being decreased again to 0.05 mL/min.  The reaction was allowed to proceed, typically until most of the reaction mixture was depleted, and the frequency and dissipation was monitored.

The growth curves were noticed to follow a distinctly non-linear growth profile, something that was not expected based on the derived rate of polymerization as shown in Figure 3.5a.  We initially believed these deviations to be due to leakage of oxygen into the system as the QCM-D was not placed in a nitrogen atmosphere.  Poisoning by oxygen would cause the copper catalyst to deactivate and explain the subsequent slowing of the growth rate.  To confirm these results, silicon wafer pieces were polymerized under the same conditions for varies time points and the thickness was measured using spectral reflectometry.  However, although these samples were polymerized under a controlled nitrogen environment, their growth profiles exhibited two distinct regimes, an initial rapid burst following by a slow, nearly linear growth. (Figure 3.5c, green square)
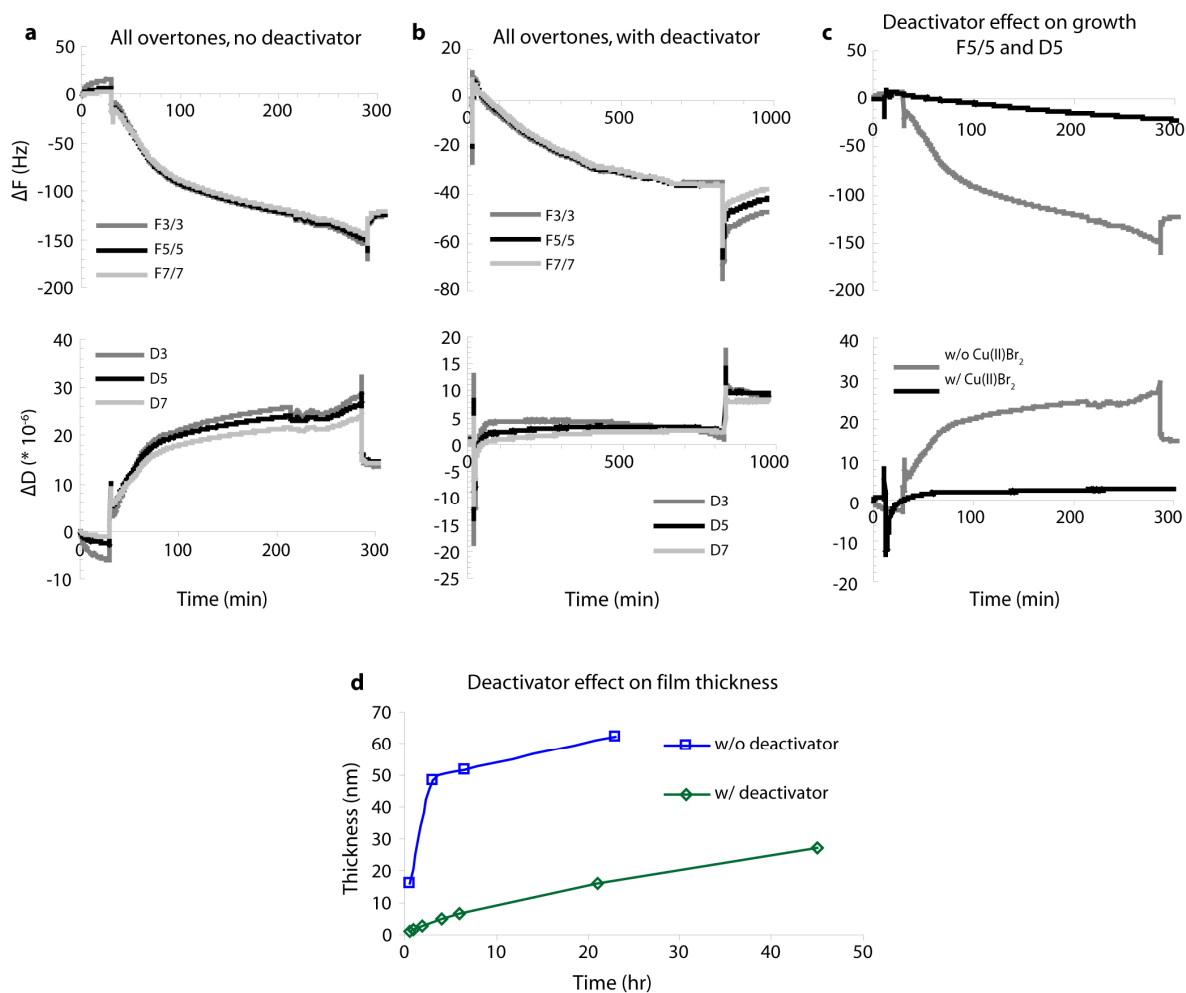
Figure 3.5. *In situ* monitoring of ATRP growth with QCM-D.  The reaction without deactivating CuBr2 (a) shows rapid growth initially followed by a slow, sustained growth.  Addition of deactivator significantly slows the reaction and eliminates the initial rapid growth (b).  The fifth overtone for each run is overlaid in (c).

It has been demonstrated that addition of 30% Cu(II)Br$_2$ relative to the molar concentration of the Cu(I)Br can improve the linearity of the growth curve and the overall PDI of the final polymer[82]  This effect is easily explained by the reaction mechanism described in Figure 3.1, as the controlled radical polymerization depends on the deactivating step (in our particular reaction) of Cu$^{+2}$ abstracting a radical from the growing polymer chain and rebrominating it, temporarily preventing it from polymerizing or terminating.   Without the presence of the copper(II) species, the reaction simply becomes an uncontrolled free radical polymerization.  In a bulk polymerization with a large amount of solubilized initiator, the generation of radicals from the initiator will create a significant amount of Cu$^{+2}$ in solution to act as deactivator.  However, for surface initiated polymerizations, the amount of initiator is low relative to the total amount of monomer and activating Cu$^{+1}$ in solution.  This resulted in a significant amount of free radical polymerization during the first phase of the reaction, eliminating the desired control of the growth rate.  Therefore, we adapted our polymerization strategy to include the 30% cupric bromide relative to cuprous bromide concentration, and a noted change was observed in the polymerization rate, as shown in Figure 3.5c & d.

*Surface analysis*

The final steps in characterizing our surface modification scheme were verifying the surface chemistry, surface roughness, and non-fouling nature of the polymer.  Surface roughness of the film after both silanization and brush layer synthesis is shown in Figure 3.6, demonstrating the lack of surface features on our film (RMS roughness less than 1 nm). The surface chemistry of the polymer thin film was verified by x-ray photoelectron spectroscopy (**XPS**). High resolution C1s scans for a substrate modified with the silane initiator and a polymer brush layer after 3 hours of growth are shown in Figure 3.7 and Table 3.2, with atomic analysis is shown in Table 3.1. Bare quartz substrates show a high percentage of silicon and oxygen, with some carbon-carbon and carbon-oxygen peaks appearing, likely due to adventitious hydrocarbon species adsorbing on the surface before scanning.  Silane modification results in the appearance of a trace of bromine and a carbonyl moiety, expected from the brominated methacrylate terminal functionality.  Following pEG synthesis, the high resolution C1s scan is dominated by the ether peak, as would be expected for a film containing a large amount of ethylene glycol units.  For atomic analysis, copper was also analyzed due to its cytotoxicity, and none was found within the detectable limits of the XPS.  Oxygen and carbon appear in roughly a 2:1 ratio, as would be expected for an ethylene glycol polymer.
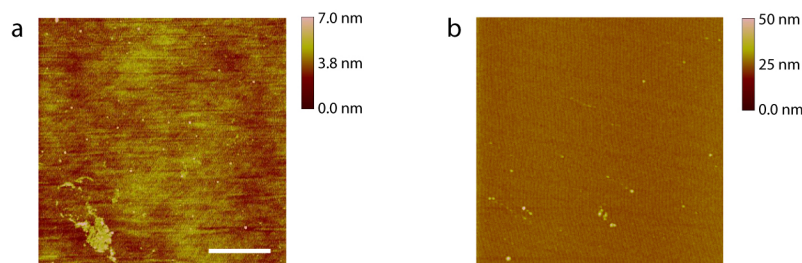


Figure 3.6. AFM scans after each step of the ATRP synethsis: silane deposition (a) and pEG brush synthesis (b).  For each step, the RMS roughness was less than 1 nm. (scale bar = 5 microns)
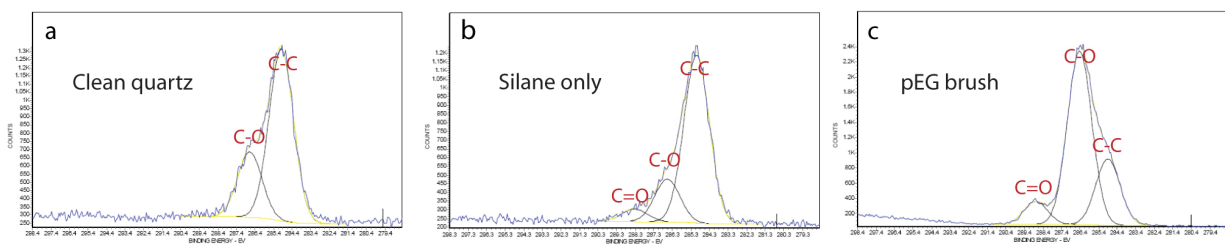
Figure 3.7. XPS high resolution C1s scans of our samples in various steps of the reaction. Brush layer synthesis (c) shows a dominant peak representing C-O bonds, as would be expected for an ethylene glycol containing polymer.

Table 3.1. Atomic percentages of various elements detected by XPS.

| Sample | Atomic Percent | | | | | |
|---|---|---|---|---|---|---|
| | C | O | Si | Br | Cu | N |
| Cleaned quartz | 19.2 ± 0.4 | 53.4 ± 0.7 | 27.4 ± 0.5 | n/d | n/d | n/d |
| Silane | 18.0 ± 1.6 | 52.9 ± 1.6 | 27.9 ± 0.3 | 0.3 ± 0.2 | n/d | n/d |
| pEG brush | 68.8 ± 0.7 | 30.8 ± 0.8 | 0.4 ± 0.4 | n/d | n/d | n/d |

Table 3.2. Relative percentages of peaks from C1s high resolution scan detected by XPS.

| | BE (eV) | % | Probable Chemistry |
|---|---|---|---|
| Cleaned Quartz | 285.0 | 72.6 | C-C, C-H |
| | 286.7 | 26.4 | C-O |
| Silane | 285.0 | 76.7 | C-C, C-H |
| | 286.5 | 17.1 | C-O |
| | 288.2 | 6.3 | C=O |
| pEG brush | 285.0 | 23.1 | C-C, C-H |
| | 286.5 | 68.2 | C-O |
| | 288.9 | 8.7 | C=O |

For protein adsorption onto the pEG film, QCM-D was again employed to demonstrate the lack of adhesion of protein on the surface. A quartz crystal was modified with a pEG film using our standard reaction conditions, and placed into the QCM-D chamber. For this experiment, the surface was exposed to three protein solutions in PBS to demonstrate its ability to prevent protein adsorption: 20% fetal bovine serum; 0.1 mg/mL neutravidin; and 0.1 mg/mL fibronectin. The pEG modified quartz crystals were loaded into the chamber, and equilibrated with PBS for at least 1 hr. The PBS was then replaced with the protein solution for 45 minutes, followed by rinses with PBS, a 2% Hellmanex solution, and PBS again. The protein adsorption curves are shown in Figure 3.8.
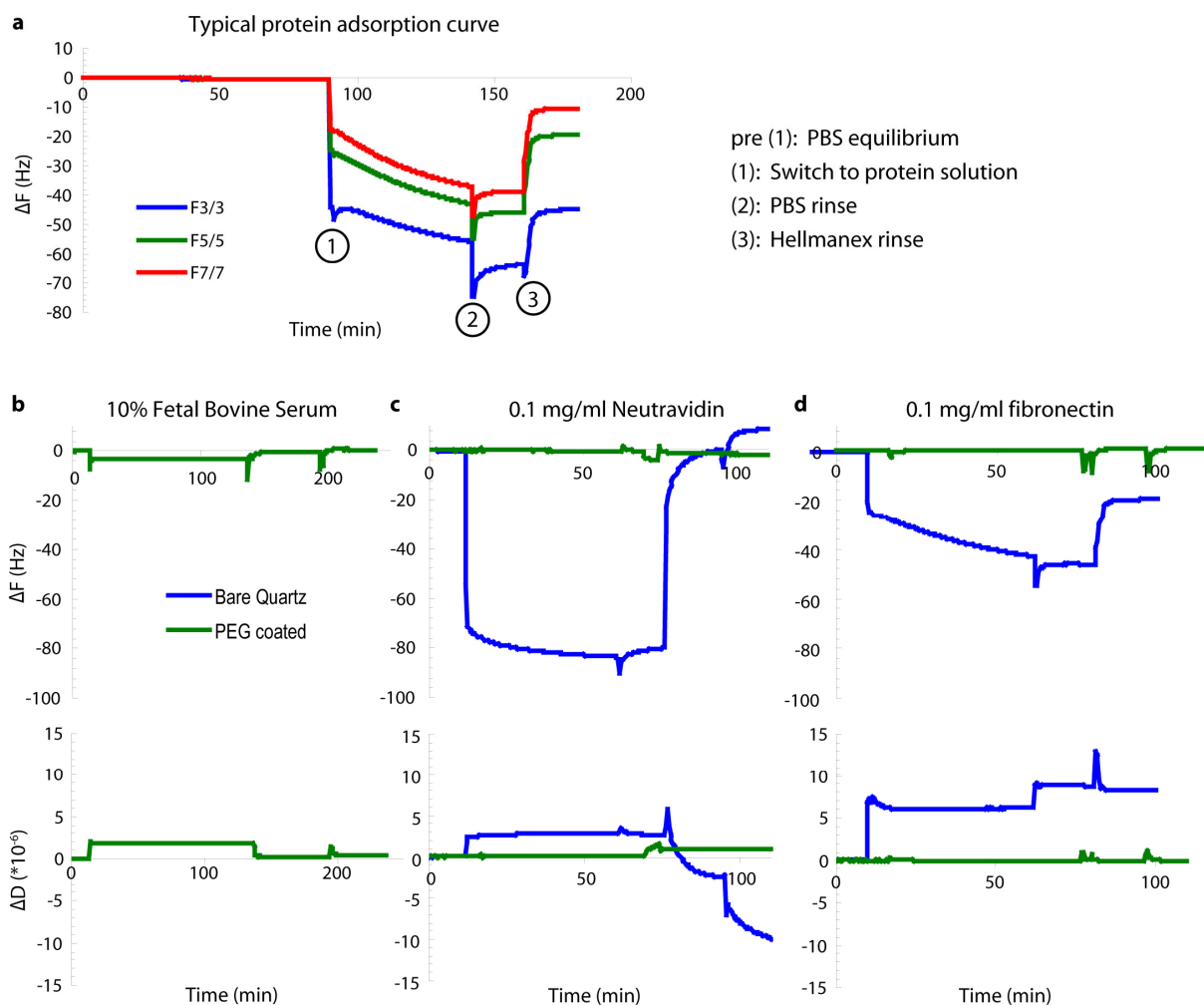
Figure 3.8. QCM-D monitoring of protein adsorption on bare and pEG brush layer coated quartz. A typical protein adsorption curve is shown in (a), noting changes in the chamber solution. Changes in frequency (top) and dissipation (bottom) of FBS (b), neutravidin (c), and fibronectin (d) are shown in green. For neutravidin and fibronectin, adsorption onto a bare quartz oscillator is shown in blue for comparison.

   The fibronectin (b) and neutravidin (c) compare bare quartz substrates with pEG modified substrates. Quartz substrates showed a large change in frequency and dissipation, suggesting that protein was adsorbing to the surface, and the subsequent PBS rinse did not remove the protein. Substrates modified with pEG brush layers under the same conditions showed no significant changes in frequency and dissipation under fibronectin and neutravidin solutions, and only minimal change (~3 Hz) under 10% serum that was reversed upon the PBS rinse. The small change in frequency and dissipation in this case could represent a small amount of protein adsorbing to the surface, a small amount of protein associated with the surface but not physically adsorbed on it, or a small shift in the bulk density and viscosity of the fluid in the chamber. As the noted change is reversed upon rinsing with PBS, there does not appear to be any permanent protein adsorption onto the substrate or film.

### 3.4 - Discussion

In this chapter, the development of our surface modification scheme was outlined.  Due to the unsuitable surface roughness of the previously developed IPN chemistry, as well as the inability to directly control the thickness on the desired length scale, a new synthesis method was developed and characterized.  Surface initiated ATRP proved to be an ideal choice for our particular reaction scheme, as the controlled reaction allowed for ease of control of the film thickness and yielded a marked decrease in the overall surface roughness of the resulting film, critical for characterizing our features using AFM.  The localization of our silane initiator to the quartz surface resulted in insufficient copper(II) species in the polymerization solution and rapid initial growth of the film, causing variations in overall film thickness under identical reaction conditions.  Addition of a small amount of copper(II) in the reaction mixture eliminated this rapid polymerization and yielded more reproducible results.

Surface chemistry was verified by XPS following each step, showing the presence of bromine and carbonyl groups after modification with a brominated methacryl terminated silane.  A large ether peak appears after modification with the pEG brush with approximately a 2:1 oxygen:carbon ratio, as expected, and does not show the presence of any copper species in the brush.  The ultra thin polymer films also resist protein adsorption, showing a frequency change of less than 3 Hertz under 10% serum that was reversed following PBS rinsing, and negligible frequency and dissipation changes for 0.1 mg/mL neutravidin and fibronectin solutions.

The SI-ATRP synthesis of pEG brush layers showed all of the required characteristics necessary for our desired patterning scheme: flatness, tunable thickness, and robust protein adsorption resistance.   The reaction mechanism also provides a number of other potential benefits for future work in this area.  Any molecule containing a halide leaving group that will generate a radical can be used as an initiator leaves a wide range of suface modifications open.  Localization of the polymerization to the surface eliminates complications of photoinitiated polymerizations, such as polymer "skins" forming on the surface preventing light penetration to the samples, localized clumps of polymer forming on the surface, and uneven illumination.  From a protein adsorption standpoint, growing the pEG brush directly from the surface, similar to a "grafting from" approach, yields a very dense polymer surface and eliminates the need for cloud point grafting and other workarounds in typical "grafting to" strategies.

# Chapter 4 - Laser Nanomachining for pattern generation

## 4.1 - Introduction

   A main objective of this thesis was to develop a robust method for nanopatterning biomolecules at interfaces. Following the modification of a cell culture substrate with an ATRP synthesized pEG brush layer to provide a non-fouling background, we developed a patterning methodology involving femtosecond laser ablation of the thin film and subsequent adsorption of proteins of interest onto the exposed quartz. Our overall surface patterning strategy is described in Figure 4.1. Laser ablation patterning scheme. Figure 4.1, in which a 10-15 nm pEG brush layer was selectively ablated using femtosecond laser pulses to expose the quartz substrate beneath. The exposed quartz was then used as a selective adsorption site for surface modification, and could theoretically adsorb a wide range of biomolecules or possibly targeted for subsequent chemical modification. As a model system for this particular work, we adsorbed avidin or a derivative and conjugated with a biotin derived molecule of interest.
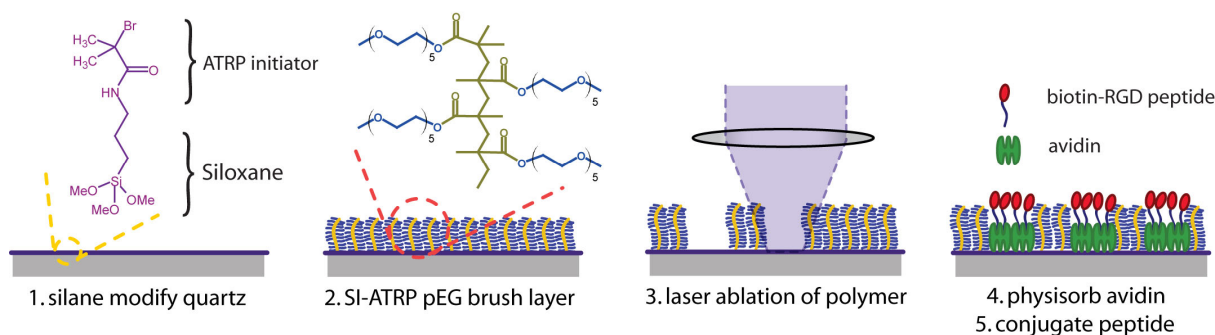


Figure 4.1. Laser ablation patterning scheme.

   As described in Chapter 2.2, a wide range of factors influence the ablated feature area and crater depth on both the laser/objective side and the material selection side. The ability of the material to absorb energy from the laser beam at its particular wavelength will determine ablation threshold and the number of photons required for breakdown to occur. On the laser side, the numerical aperture and overall magnification strength of the objective determine the dimensions of the beam spot diameter. The wavelength of the processing light also influences the beam spot dimension, as well as sets the energy per photon. The polarization of the beam as it is processed through the various objectives and filters, overall fluence of the beam, and the number of pulses per feature all affect feature dimensions and shape.

   Laser based processing has been used in a wide variety of patterning applications, including top down, bottom up, and three dimensional patterning schemes. Using a photoinitiators, polymer structures can be created in multiple dimensions by using multiphoton absorption process in combination with a three dimensional stage,[88] as well as conjugating biomolecules within already formed hydrogels.[89] They have also been used to pattern photosensitive resists to generate imprint lithography masters or directly pattern substrates,[90] Ultrashort pulse lasers have proven to be advantageous tools for precise nanomachining due to reduced heat and shock affected zones, as well as sharper and significantly lower material modification and ablation thresholds, including the ability to ablate subcellular regions without rupturing the cell membrane.[91] Due to the Gaussian nature of the beam profile, features smaller than the processing beam spot size can be fabricated by precisely adjusting the femtosecond pulse energy

to the threshold neighborhood, especially when a multiphoton liftoff process is employed.[92, 93]

### 4.1.1 - Laser nanomachining setup

The laser nanomachining setup is shown schematically in Figure 4.2. Amplified Ti:Al$_2$O$_3$ laser pulses of ~100 fs (**FWHM**; full width half maximum) and 800 nm wavelength were used for nanomachining after being frequency-doubled to a wavelength of 400 nm by a nonlinear crystal (**NLC**) and focused through a processing objective. The processing lens was also used to monitor the surface *in situ* by imaging with a CCD camera coupled to a zoom lens (12X), providing a useful means for ensuring the sample was maintained in proper focus during the nanomachining process. As the laser pulse energy required to ablate high resolution features was extremely low, three separate beam attenuators were inserted into the beam path; a half waveplate ($\lambda$/2) with a thin film polarizer, a half waveplate ($\lambda$/2) with a polarizing beamsplitter, and a neutral density filter. As the beam applied to the sample surface was linearly polarized (P polarized), the sample was precisely aligned normal to the incoming beam path by adjusting the tilting angle of the sample to minimize polarization effects. To generate user designed patterns, samples were loaded on a precise two-dimensional motorized microstage having ~0.1 μm resolution with a synchronized laser firing system controlled by a programmable PC.
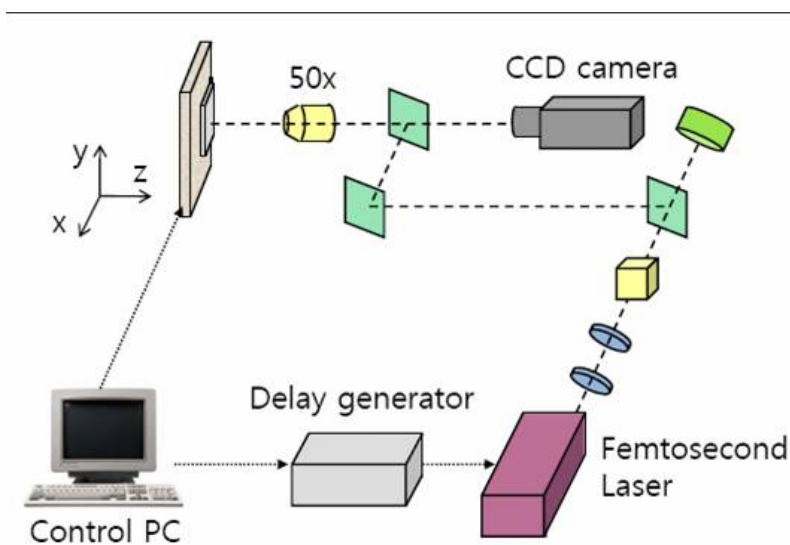


Figure 4.2. Schematic of the femtosecond laser nanomachining setup. (Courtesy of Hojeong Jeon)

## 4.2 - Methods

ATRP film synthesis was carried out as described in Chapter 3.

### Pattern generation

Patterns were generated on ATRP-synthesized pEG films (see, Chapter 3) using the machining setup described above. The pEG modified quartz substrates were mounted onto the XY-stage and brought into focus. As the lens remains fixed, the sample was moved to the edge points of the intended patterned regions, and the tilt of the XY-stage was adjusted such that the sample remained in focus over the entire patterned area. The laser energy was altered by adjusting the polarization angle of the thin film polarizer relative to the incoming beam polarization, and measured by placing an energy meter in the beam path. Computer control of

the XY-stage and the Z-axis of the processing objective allowed us to raster the sample and adjust focus and patterns on the fly.

*Protein adsorption*

To create nanoscale adhesion domains, the SI-ATRP synthesized pEG brush layer was selectively ablated using single femtosecond laser pulses to expose the underlying quartz substrate as described at length in the text. After ablation, either neutravidin or fibronectin (0.1 mg/mL) was physisorbed to the bottoms of the craters from phosphate buffered saline (PBS) for 60 min. For neutravidin modified surfaces, the substrates were rinsed with PBS, and then exposed to the biotin modified probe (0.1 mg/mL) of choice for 30 min. Biotinylated molecules used included a biotin-conjugated peptide presenting the cell-binding domain of bone sialoprotein (**bsp**), biotin-CGGNGEP**RGD**TYRAY-NH$_2$, termed **biotin-bsp-RGD(15)** and a non-adhesive version biotin-bsp-RGE, (American Peptide) as well as biotin-Alexa594 (Molecular Probes) to visualize the bioconjugation spatially.

*Confocal imaging*

Protein deposition was verified by tagging neutravidin with a fluorescently labeled biotin probe. Following staining as described above, the samples were mounted under a coverslip in SlowFade (Molecular Probes), and imaged on a Zeiss 510 Meta confocal microscope.

*AFM Imaging*

AFM images were obtained in tapping mode using high aspect ratio tips (7:1) to obtain accurate measurements in the bottom of heavily ablated craters.

## 4.3 - Results

### 4.3.1 - Ablation characteristics of SI-ATRP synthesized brush layers

In order to generate nanopatterned substrates, the ablation characteristics of our film/substrate system using femtosecond laser pulses were explored. A wide range of parameters can affect the ablation characteristics, as described in Chapter 2.2. In order to effectively pattern our substrates, we needed to determine the feature diameter resulting from a variety of objectives, film thicknesses, and laser fluences. We initially undertook a parametric study examining feature size versus pulse energy for a fixed objective and film thickness. By using various energies, we were able to generate 3 different feature geometries, as shown in Figure 4.3.
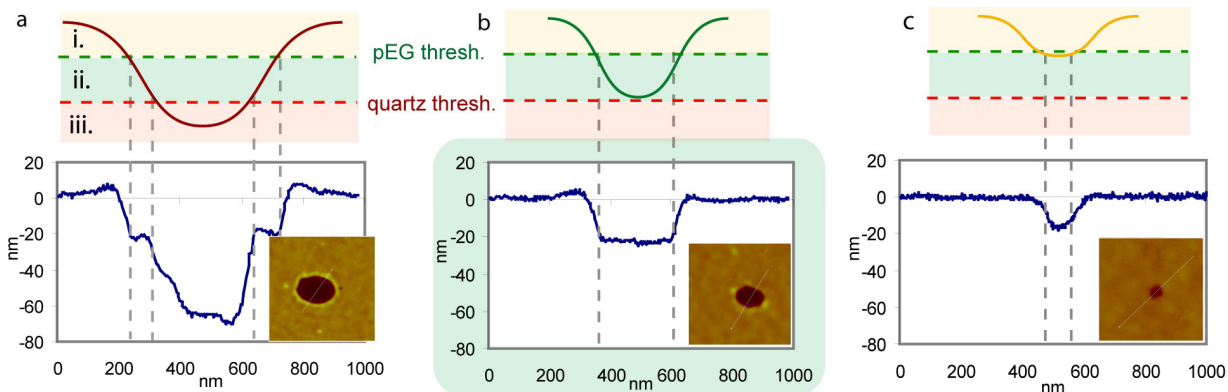
Figure 4.3. Overview of ablation characteristics of our substrate/film system. At high fluences (a), there is sufficient energy to exceed both the pEG and quartz ablation thresholds, ablating through both. In (b), only the polymer ablation threshold is crossed, removing only the film. In (c), the film is only partially removed, and no quartz is exposed.

Three ablation regimes were demonstrated in our parametric study: when the energy was above the quartz ablation threshold (region iii, red) there was sufficient energy to ablate both the quartz substrate and the polymer. Due to the Gaussian profile of the beam intensity, high ablation energies result in a "double crater" as shown in Figure 4.3a. The fluence of the center of the beam exceeded the quartz ablation threshold and the profile penetrated into the substrate, while only polymer was removed in a narrow band surrounding the quartz ablation crater. For intermediate energies, (region ii, green) only the polymer ablation threshold was crossed, and a flat bottomed crated was observed as only the polymer film was removed (Figure 4.3b). No penetration into the substrate was observed. For lower energies, (Figure 4.3c) the polymer ablation threshold was crossed, but only slightly, resulting in incomplete film removal that did not penetrate to the substrate. For energies below the polymer threshold (region i, yellow) there was no observable film removal.

For our initial parametric study, a 15 nm thick pEG brush layer was ablated using femtosecond laser pulses that had been frequency doubled to a wavelength of 400 nm and focused through a 50x, 0.55 NA objective. The sample was rastered through the fixed beam to create columns of features, with four columns generated at each pulse energy. AFM images of the ablated surfaces, as well as high-resolution images of single features, are shown in Figure 4.4, demonstrating the regularity of features at or above 60 nJ (a-b). Below this threshold, as shown in Figure 4.4c, features were inconsistent in terms of size and appearance, although higher resolution was achieved. Features approaching 100 nm were visible at 56 nJ, while below this energy it was unclear whether the polymer was fully ablated from the substrate, or just modified. (d) While this initial study parametrically examined pulse energy, a number of other variables can affect the ablation energy required for film removal, including film thickness and density, the numerical aperture of the focusing objective, focal positioning of the objective lens, and laser beam profile and alignment. The data presented here are defined for our polymer/substrate system with a fixed film thickness, lens arrangement, and single pulse ablation. The optimized process energy will change when the aforementioned film, optics, and laser properties are altered.
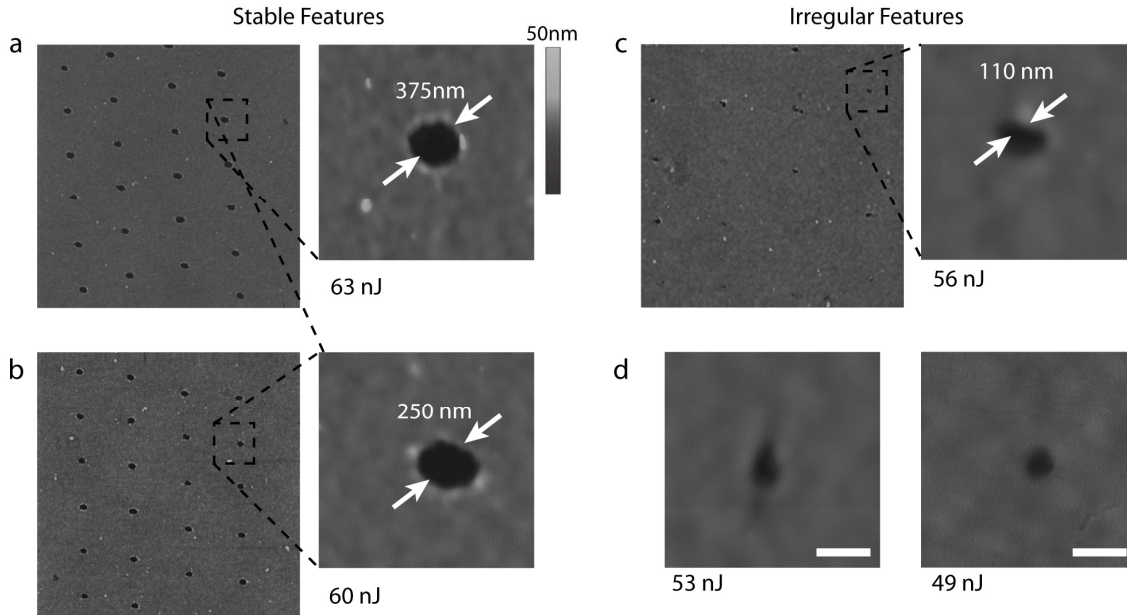
Figure 4.4. Overview of feature sizes for various pulse energies. Features in (c) and (d) were ablated near the pEG threshold and appeared inconsistently. (sb = 200nm)

Two factors that are easily within our control are the magnification of the processing objective and the thickness of the film, and similar parametric studies were undertaken for films of various thicknesses and different processing objectives. Figure 4.5 plots the effect of fluence on the squared diameter of the observed features for various objective and film thicknesses. The effect of fluence on feature diameter is shown Figure 4.5a for various objectives, including a 10x (0.28 NA), 20x (0.42 NA), and 50x (0.55 NA). Samples were ablated as described above and characterized using AFM. The diameter was measured across the top surface of the feature, and therefore the exposed substrate area was significantly smaller. As expected, feature diameter was drastically reduced for high magnification and numerical aperture objectives, with submicron (below $1*10^6$ nm$^2$) features ablated using both 20x and 50x objectives. A similar study was performed on films of various thicknesses, ablating with the 50x objective at various fluences, and is shown in (b). Interestingly, thicker films appeared to ablate more effectively, with a higher amount of material removal observed for a single shot, as compared to thinner films. However, this higher degree of film removal is counter productive towards shrinking feature sizes and leads to large observed feature diameters. Ablation was also carried out on a bare quartz wafer piece to determine the quartz ablation threshold, critical for determining design parameters to achieve clean film removal without substrate damage.
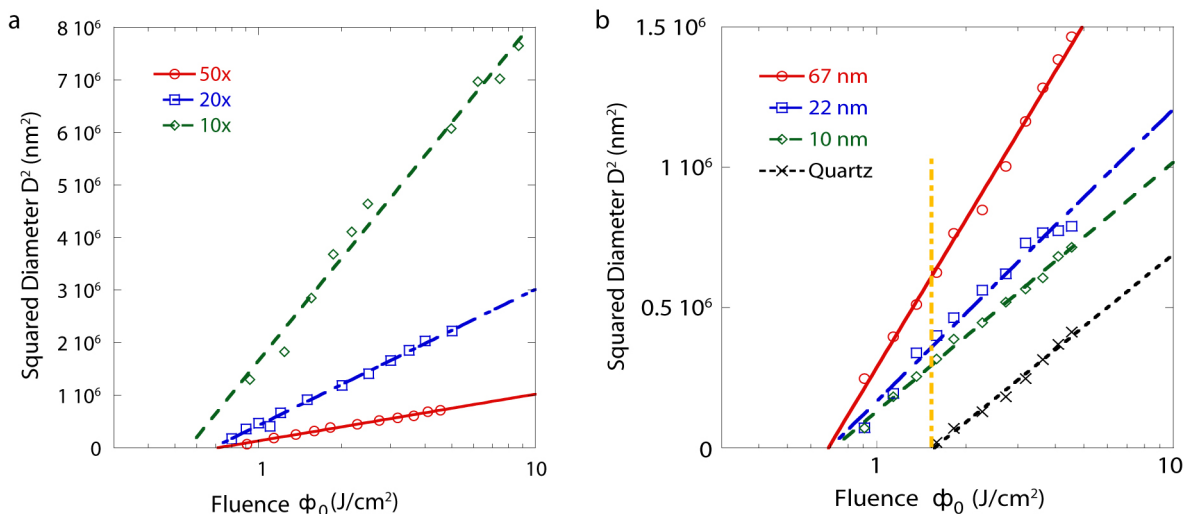
Figure 4.5. Feature size as a function of fluence for various processing objectives on a 10 nm film (a) and varying film thicknesses with a 50x objective (b). The vertical yellow line in (b) represents the ablation threshold of the quartz substrate, below which only removal of the pEG film takes place. For ease of reference, $1*10^6$ nm$^2$ corresponds to a 1000 nm diameter feature. (Figure courtesy of Hojeong Jeon)

The ablation thresholds for each processing configuration were determined by the intercepts of the linear fit lines for each processing setup. From Figure 4.5b, to achieve film removal without substrate ablation, processing must be performed at fluences lower than the ablation threshold of the quartz, denoted by the vertical yellow line at roughly 1.5 J/cm$^2$. Below that processing threshold, a wide range of feature sizes can be achieved for a 10 nm thick film, simply by using different processing objectives and fluences.

### 4.3.2 - Protein adsorption into ablated craters

Protein adsorption was visualized by staining avidin or neutravidin modified substrates with a biocytin-AlexaFlour conjugate and imaging with confocal microscopy. Using this method, spots were visible down to ablation energies corresponding to 250 nm diameter features, with the background pEG around the features unstained. These features had roughly the same diameter as the measured AFM craters, but as the smaller features approached the diffraction limit of the microscope, making them difficult to visualize. In certain cases, at very high ablation energies in our parametric studies, background damage to the pEG film was noted and a dim fluorescent "halo" was observed around the patterned area that faded as ablation energy was lowered. Figure 4.6 shows confocal images of laser ablated pEG films that have been adsorbed with avidin and tagged with a biocytin-Alexa594. The samples were processed using single shots at various pulse energies with a 50x objective on a 15 nm film, and the features correspond to those imaged with AFM and shown in Figure 4.4. Fluorescence was visible on features ablated with pulse energy of 60 nJ, which corresponds to feature diameters of 250 nm.

38
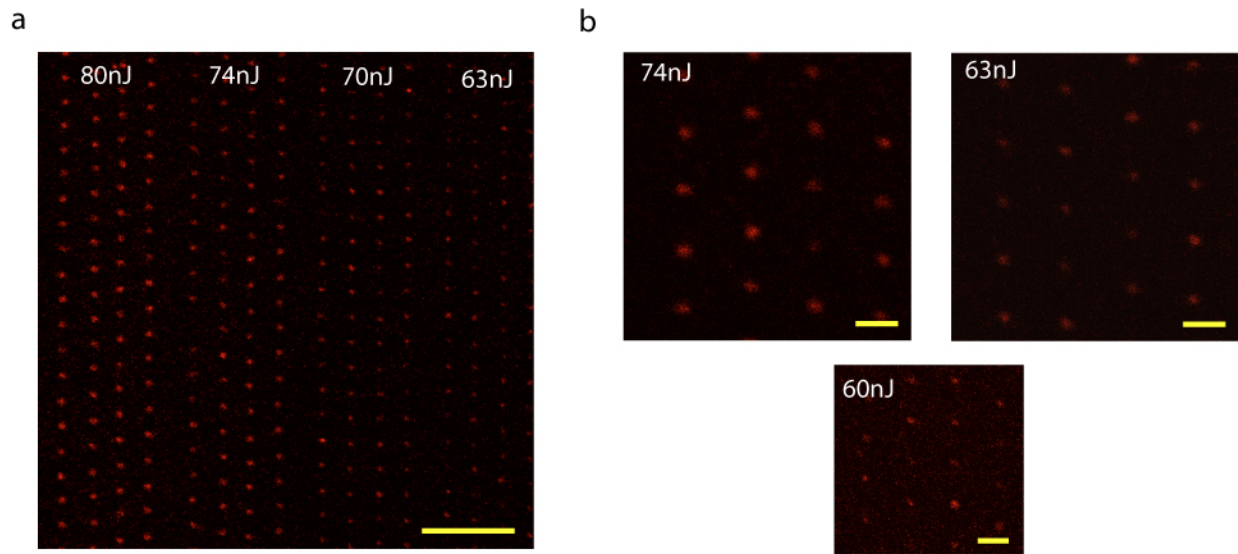
Figure 4.6.  Confocal images of avidin/biotin-Alexa594 adsorbed into ablated features.  Overview shown in (a, sb = 10 µm) Features were visible down to pulse energies of 60 nJ (b, sb = 2 µm), which corresponded to ~250nm features.

Feature diameters at ablated at energies at lower than 60 nJ have dimensions smaller than the diffraction limit of the confocal scope, therefore AFM was also employed to determine if protein was adsorbed into the craters.  Scans were taken of the same area using a high aspect ration tip prior to and following exposure to neutravidin and fibronectin solutions at 0.1 mg/mL in buffer to determine if a height change could be detected, and cross sections are shown in Figure 4.7. Both neutravidin (a-c) and fibronectin (d-f) show approximately a 2-5nm reduction in crater depth for ablated features after protein adsorption, as well as a notable increase in the roughness of the polymer surface.  The difference in crater depth appears for higher pulse energies that ablate into the quartz substrate as well as flat bottomed "film only" removals, which suggests that sufficient film removal occurs to eliminate the pEG brush layer's non-fouling capacity.
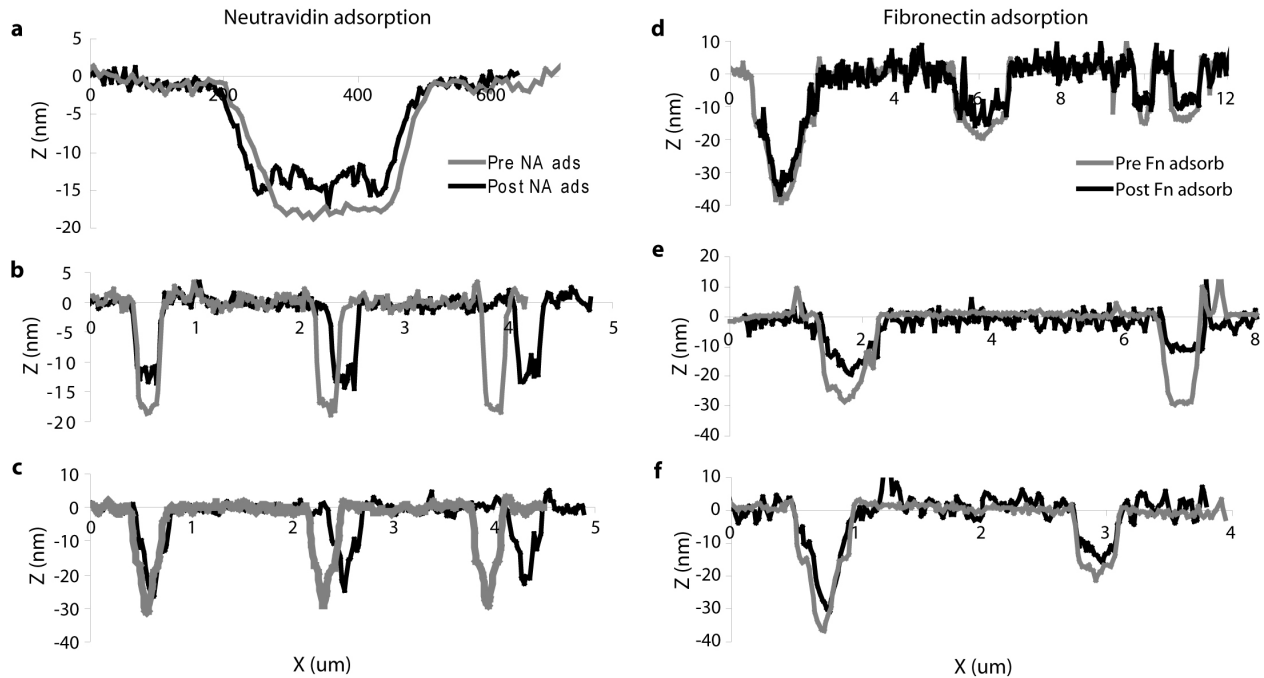
Figure 4.7. AFM scans before and after adsorbing protein onto patterned surfaces.  Both neutravidin (a-c) and fibronectin (d-f) were examined to verify changes in crater depth.  In both cases, decreases in depth from 2-10 nm were observed.

### 4.3.3 - Multishot patterns

Multiple shots near the ablation threshold have yielded sub 100 nm features in metal films using far field optics.  Therefore, multishot ablation using our processing setup was explored as an option to reduce feature size, as well as ensure a more repeatable and cleaner ablation profile. AFM scans and corresponding confocal images of fluorescently tagged avidin of features ablated near the threshold energies are shown in Figure 4.8.  Multishot features were created by stopping the stage at each feature, and ablating with a set number of pulses in rapid succession before moving to the next single feature.  In Figure 4.8, the pulse energy decreases moving from (a) to (d).  Each individual image depicts 6 columns of ablated features, with the first two columns on the left corresponding to single shot ablation, the middle two columns to 5 shots at the same energy, and the right two columns to 15 shots.
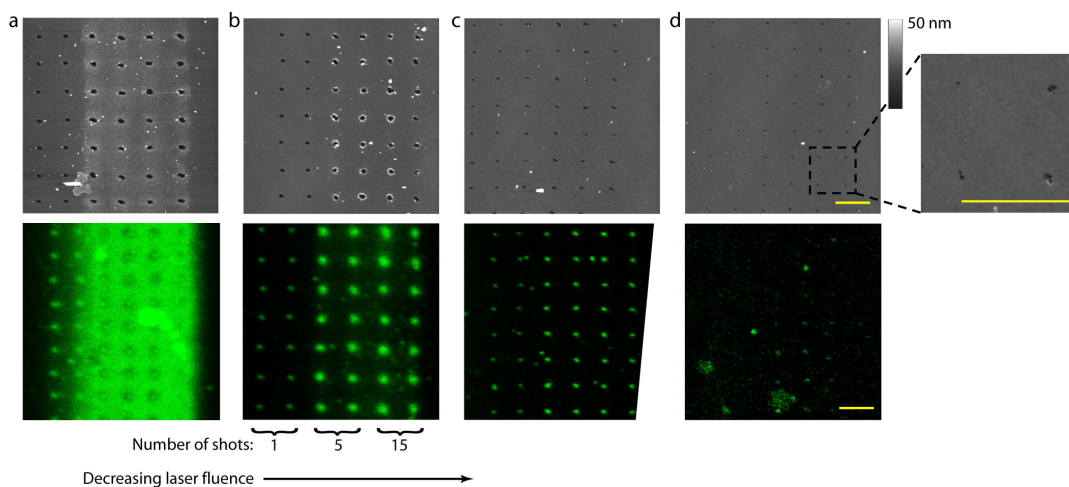
Figure 4.8. Effect of multiple shots feature size and protein adsorption. Each image represents a separate ablation energy, with 1, 5, and 15 shots for each energy.  (sb = 5 μm)

Examining the fluorescence and AFM images in Figure 4.8, it is clear that an incubation effect occurs during multishot ablation for our polymer film, resulting in collateral film damage surrounding the actual ablated area.  For high fluences (a), this damage eliminates the film's ability to resist protein adsorption complete, as the right 4 columns of features are nearly occluded by the strong fluorescent signal that surrounds the features.  This damage is also clearly evident surrounding the features in the tapping mode AFM scan.  These features were ablated using a high laser fluence, corresponding to single shot features of over 500 nm.  As laser fluence approaches the ablation threshold of the pEG film, the background film damage is reduced and eventually eliminated:  it is still slightly visible in (b), and not present in (c).  For ablation near the polymer threshold (d), protein fluorescence was only visible for a small number of the multishot features at the bottom of the confocal scan.  However, as these features correspond to single shot features of sub-200 nm, it is unclear whether this is due to lack of protein or the limitations of the imaging methodology.

Multishot features have a brighter fluorescent spot under confocal imaging than their corresponding single shot counter parts, but the difference between 5 and 15 shots was not qualitatively different.  This increased brightness suggests increased protein presence in the crater, but the mechanism by which this occurs is not clear.  From the zoomed AFM image in Figure 4.8d, there are irregularities in the perimeter of multishot ablated features when compared to the typically circular or oval shaped single shot features, a result of small displacements in the stage that cause each shot to ablate in a slightly different area.  Thus, the increase in feature brightness could correspond to either a more complete film removal in the bottom of the feature, increased feature area due to incubation effects, increased area due to small stage displacements occurring during the multishot process, or some combination of the three.

### 4.4 - Discussion

We have demonstrated our ability to create protein islands using femtosecond laser nanomachining.  By using a variety of objectives and pulse energies, we can generate a wide variety of feature sizes, as well as having the ability to alter the polymer layer thickness.  Laser machining provides a flexible and tunable patterning system to examine cell response to proteins

on the nanometer length scale. Since the current processing system has a fixed objective, a variety of patterns can be created simply by programming the XY stage motion on the computer control system. Figure 4.9 shows patterns that can be created that are not easily achievable using comparable patterning processes. For example, a two dimensional gradient of feature spacing that spans 100 microns on a side is shown in (a), and isolated patterns on the order of the area of a single cell (40 x 40 microns) that could constrain single cells are shown in (b). Large area cell patterns, including isometric pitch patterns (a, inset) and gradients of pitch and/or feature diameter can be patterned. Such large area patterns are not easily achievable by scanning probe and other serial lithography processes, while isolated feature patterns and more complex gradient patterns would not be achievable by colloidal or other distributive lithographical processes.
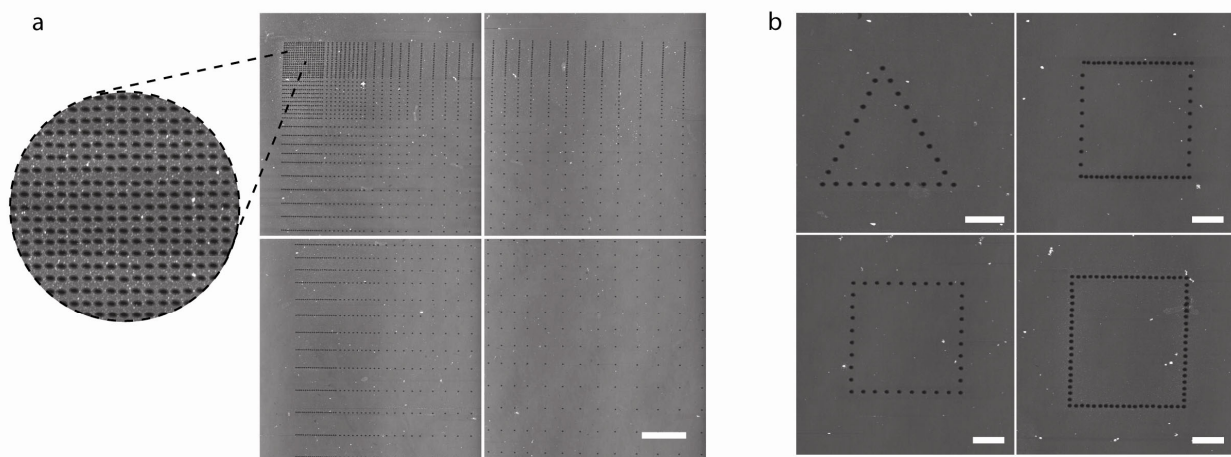


Figure 4.9. Various features arrangements achievable using laser nanomachining. Isometric pitch (a, inset), one dimensional and two dimensional gradients (a, sb = 20 μm) and areas designed to isolate single cells in various geometries (b, sb = 5 μm).

However, our patterning method, especially in its current form, has a number of significant disadvantages that must be overcome before it could be widely utilized by the biological community. Currently, throughput is not much higher than e-beam lithography and is significantly lower than colloidal lithographies as the maximum stage speed is limited to 0.2 mm/s, with translational repeatability errors that are significant for nanoscale patterning. Patterning complex geometries that only depend on stage motion is simple, but gradients of feature diameter are difficult as the laser fluence or objective lens must be changed during the patterning process by hand, as these are not automated in the current process. The sample tilt also must be adjusted perpendicular to the incoming beam path to ensure the sample remains in focus across the entire patterned area during translation in both the X and Y direction. It should also be noted that the sample is mounted vertically, as depicted in Figure 4.2, an unstable configuration that causes vibration and translational errors in all three dimensions. These errors are significant on the nanoscale in the XY dimension, as demonstrated by the oddly shaped features shown in the multishot study (Figure 4.8d, insert) caused by sample motion relative to the processing objective. Sample movement in the Z-direction (along the beam axis) is also problematic, especially for high magnification objectives with smaller focal depth, as the sample moves slightly out of focus and results in decreased ablation efficiency.

Based on the multishot processing study, patterning with multiple pulses seems to provide greater protein density within individual features. The current stage, however, would not allow

for quick, clean patterns to be made.  As described above, sample motion causes error in the position of the craters on the order of hundreds of nanometers, resulting in odd feature shapes. The stage must also be brought to a complete stop to generate every individual feature, which causes drastic increase in sample processing time for high density patterns.  Currently, we are able generate a 1 mm x 1 mm patterned area in approximately 4 hrs at a reduced 20 Hz firing rate, depending on the feature density required and using single shot features. However, throughput depends heavily on the overall number features required and can be greatly improved with a higher speed stage and increased firing rates. The maximum firing rate of current our laser system is 1 kHz, allowing orders of magnitude improvement in processing speed, especially if coupled to an industrial stage capable of movement at 100 mm/s, resulting in the ability to pattern a 1 cm$^2$ cell culture surface with 1 μm pitch in approximately 30 mins.

# Chapter 5 - Optimization of avidin/biotin for ligand presentation

## *5.1 - Introduction*

In this chapter, the use of avidin derivatives and a number of biotinylated biomolecules was explored to determine the most effective system to present peptides from our nanopatterned interfaces. The laser nanomachining process described in the previous chapter ablates the non-fouling pEG brush layer in subregions of the surface, allowing for subsequent protein adsorption into the craters. To render the patterns cell adhesive, a number of ECM proteins could be adsorbed to the surface, including laminin, fibronectin, or collagen. However, simply adsorbing these proteins into the craters would remove an element of control, as denaturating of the proteins could expose cells to undesired amino acid epitopes that are normally not accessible *in vivo*. In order to create a more structured and manageable interface, the protein avidin or its derivatives were deposited into the craters, and subsequently conjugated with a biotinylated peptide of interest. This would cause the adhesive peptides to be extended into solution, allowing for increased conformational flexibility and providing tighter control of the ligand-receptor interface on our nanopatterned surfaces.

The interaction between avidin and biotin is highly specific, and has one of the highest known non-covalent bond strengths, with a dissociation constant of $5*10^{-14}$ M.[94] The avidin-biotin conjugation system has been used in the biological, biointerface, and sensor communities for a wide range of applications, including: western blots and ELISA assays[95-98], protein and cell purification from solid substrates,[99] and affinity chromatography.[100] The avidin/biotin scheme has also been utilized in other nanopatterning studies, as the ability to create multiple structured layers is advantageous is these schemes. For example, patterns of biotin have been created using photolithographic processes with a novel resist,[16] patterns of streptavidin have been created by "scraping" off a pEG layer with a scanning probe,[20] and patterns of avidin or streptavidin have been microcontact printed onto polymeric substrates.[101, 102] Following the modification of a substrate with an avidin derivative, whether it is by simple physisorption or conjugation to a biotin activated surface, the resulting avidin pattern can be further functionalized with any biotinylated molecule of interest.

Avidin itself, a protein isolated from avian egg whites, is tetrameric glycoprotein that can bind up to four biotin molecules, with each subunit binding individually to one biotin. Although avidin has been used in the aforementioned applications, the protein has been implicated in non-specific binding to substrates, other biomolecules in certain assays, and the cell membrane due to avidin's glycosylation and net positive charge.[103] Therefore, a number of derivatives have been developed, including streptavidin and its derivative neutravidin that eliminate the carbohydrate groups from the protein.[104] Neutravidin was designed to have a near neutral isoelectric point, further minimizing non-specific and electrostatic interactions.[105]

A number of biotin peptides were studied on the patterned surfaces prepared in this chapter, including a 15 amino acid peptide containing the sequence RGD that had been derived from bone sialoprotein (biotin-CGGNGEPRGDTYRAY-NH2, termed **biotin-bsp-RGD(15)**), and interacts with the $\alpha_v\beta_3$ and $\alpha_v\beta_5$ integrins.[69, 106] Peptides containing the RGD sequence are generally known to interact with integrins containing the $\alpha_v$ subunit. A peptide sequence termed AG-73 was also tested, consisting of the amino acid sequence biotin-RKRLQVQLSIRT, termed **biotin-AG-73** that is believed to interact with the heparin sulfate side chains of the Syndecan-I

transmembrane protein, and thought to provide a separate cell adhesive pathway to integrin binding.[107, 108]

Two deposition schemes are depicted in Figure 5.1, representing two methods that were explored for conjugating peptides to the surface. In Scheme 1, the avidin (or analogue) was simply physisorbed onto a cell culture substrate, followed by conjugation with a biotin molecule of interest. In Scheme 2, the substrate was first blocked with a biotinylated bovine serum albumin (BSA) to elevate the avidin molecule off the surface and prevent potential denaturation caused by protein adsorption to the surface. Cell adhesion utilizing both of these schemes, and a number avidin derivatives and biotinylated molecules of interest, was quantified using a fluorescence based DNA quantification assay. Unmodified avidin was found to cause high levels of background adhesion that were decreased on surfaces modified with neutravidin or streptavidin. Neutravidin was shown to have the least amount of non-specific background adhesion, as well as high cell attachment when conjugated to the cell adhesive biotin-bsp-RGD(15). Preplating with biotin-BSA increased the ability of cells to adhere to streptavidin/biotin-bsp-RGD(15) substrates, but had minimal effect on neutravidin/biotin-bsp-RGD(15) substrates.
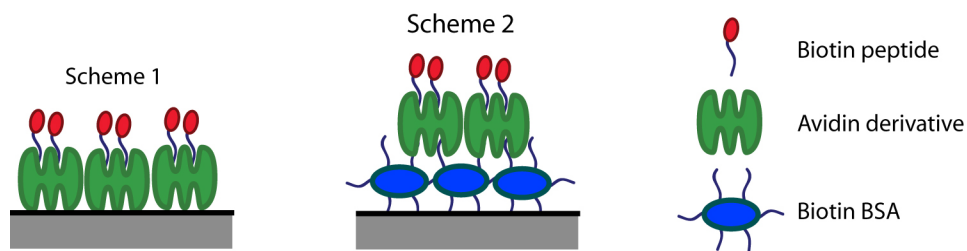


Figure 5.1. Avidin/biotin deposition schemes.

## 5.2 - Methods

### 5.2.1 - Surface Preparation

A number of combinations of albumin blocking, media conditions, and avidin derivatives were deposited onto polystyrene surface in an attempt to minimize non-specific cell adhesion, and are listed in Table 5.1. Biotinylated BSA and avidin derived proteins were adsorbed from PBS (pH 7.2) at 0.1 mg/ml for 1hr followed by three rinses with PBS. Biotin molecules were conjugated to the avidin derivatives for 30 mins at 0.1 mg/ml in PBS, and rinsed three times. Surfaces were kept under PBS until cell seeding. Avidin, streptavidin, and neutravidin were all purchased form Invitrogen. All peptides were purchased from American Peptides. Biotin-pEG was purchased from Nanocs. Streptavidin-RGD was graciously donated by Patrick Stayton's lab of University of Washington.[109]

Table 5.1. Avidin and biotin molecules tested.

| Avidin Derivatives | Biotinylated molecules |
|---|---|
| Avidin | biotin-bsp-RGD(15) |
| Streptavidin | biotin-RGE |
| Neutravidin | biotin-AG73 |
| Streptavidin-RGD | biotin-pEG |

## 5.2.2 - Cell Culture and quantification

Human mesenchymal stem cells (Lonza) were cultured in MSC growth medium (Lonza) containing 10% serum and 1% gentamicin.  For adhesion experiments, cells were allowed to adhere for 4 hrs onto the surfaces at ~$10^4$ cells/well (100 μl/well) in hMSC growth media containing serum (Lonza) or serum free DMEM (Gibco) depending on experimental conditions. After 4 hrs, the cells were rinsed once with PBS and frozen for >24 hrs at -80C, followed by quantification of the number of adhered cells using the CyQuant assay (Invitrogen) using a fluorimeter.  Standard curves to calculate cell density based on relative fluorescent units (RFUs) were generated by creating a stock solution of known cell density (counted on a hemocytometer), and performing a serial dilution before applying the same CyQuant assay.

Cells were examined on peptide-modified surfaces to assess cell morphology using a Nikon T300 in phase contrast mode.  For this, cells were plated at $10^4$ cells/cm$^2$ in either a 24 or 48 well plate on the designed surface in serum free media.  Cells were allowed to attach for 2 hrs before being rinsed with fresh media and imaged.  The remaining cells were imaged again after 1d to visualize adhered morphology.

## 5.3 - Results

### 5.3.1 - Effect of serum on cell attachment

In previous development on embryonic stem cells,[110] elimination of background attachment of cells on negative control surfaces required the use of bovine serum albumin (**BSA**) that had been heat inactivated, as well as the use of serum free media during deposition.  The effect of serum containing media and blocking with normal and heat inactivated BSA (**HI-BSA**) is shown in Figure 5.2.  The avidin/**biotin-bsp-RGD(15)** system was employed to examine cell adhesion, with wells dedicated to each point in the deposition procedure. Samples were constructed as shown in Scheme 1 of Figure 5.1:  avidin, followed by biotin-bsp-RGD(15), followed by normal or heat inactivated BSA.  Samples without blocking ("No block", white bars) and without any type of avidin/biotin modification ("Block only" on x-axis) were also quantified.  Using analysis of variance with a Tukey HSD pairwise comparison, statistical groups with a $p < 0.05$ were determined, demarcated by letters above the bars.  There were statistically significant differences between cells seeded in serum (groups C-E) versus cells seeded without serum (groups A-B). For surfaces without serum and no avidin modification, blocking was sufficient to eliminate cell attachment as seen in group A, which is significantly lower than all other statistical groups.  Heat inactivation did not seem to influence cell attachment from serum free media, as seen by the grey and black bars in group B.  However, it was noted that avidin

with and without biotin-bsp-RGD(15) peptides resulted in the same degree of cell adhesion, suggesting non-specific attachment of the cells to the avidin molecule.



Figure 5.2. Effect of heat inactivation of BSA and serum on cell adhesion. Groups without statistically significant differences are denoted by letters (e.g. A's are not significant from other A's, but are significantly different from other letters). Significance between groups was calculated with a $p < 0.05$ using a Tukey HSD pairwise comparison.

### 5.3.2 - Avidin derivatives and BSA blocking

Due to the non specific adhesion of cells to the avidin molecule, a number of other avidin derivatives were examined to attempt to minimize non-specific cell interaction. Proteins were adsorbed in the following order: the avidin or derivative (Avidin, Streptavidin, Neutravidin, or Streptavidin-RGD) followed by biotinylation (biotin-PEG or biotin-bsp-RGD(15)), and then blocking with standard BSA. CyQuant results are shown in Figure 5.3, with statistical groups again demarcated by letters above the bars. Defining statistical group D as a median degree of cell adhesion, all wells without BSA blocking were at or above this group (groups A and D, right half). Blocking with BSA effectively reduced non-specific cell adhesion for certain negative control samples, notably background adhesion to neutravidin or neutravidin/biotin-pEG and streptavidin (group C). However, addition of the biotin-bsp-RGD(15) molecule significantly improved cell adhesion to neutravidin modified surfaces, while streptavidin/biotin-bsp-RGD(15) surfaces did not show a significant difference from streptavidin only surfaces.
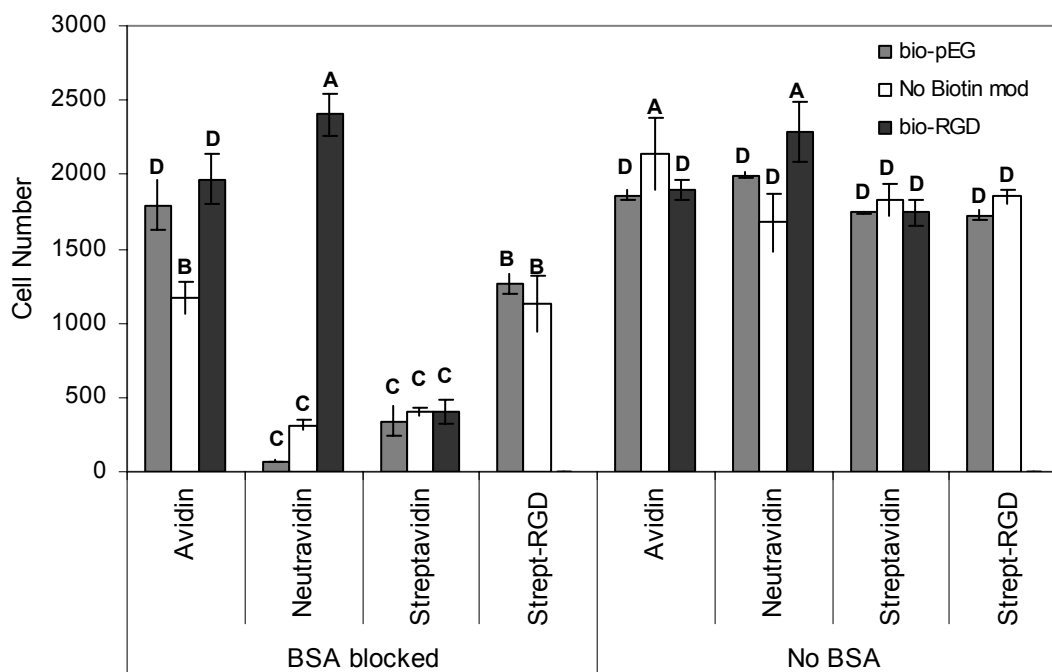
Figure 5.3. Effect of various avidin derivatives and blocking on cell adhesion. Groups without statistically significant differences are denoted by letters (e.g. A's are not significant from other A's, but are significantly different from other letters). Significance between groups was calculated with a $p < 0.05$ using a Tukey HSD pairwise comparison.

In order to help reduce potential avidin/neutravidin denaturation, as well as add another passivation layer, we preadsorbed polystyrene surface with a biotin modified BSA prior to avidin modification, as shown in Scheme 2 of Figure 5.1.  Proteins were adsorbed in the following order: biotin modified BSA (biotin-BSA), followed by either streptavidin or neutravidin, followed by a biotin-bsp-RGD(15) or biotin-pEG, followed by blocking with BSA.  As seen in Figure 5.4, preincubation with biotin-BSA improved overall cell adhesion for streptavidin/biotin-bsp-RGD(15) modified surfaces, suggesting that physisorption streptavidin to polystryrene has a deleterious effect the proteins ability to bind biotin.  For neutravidin, preincubation with biotin-BSA did not seem to affect cell adhesion on RGD modified surfaces, shown by group B.
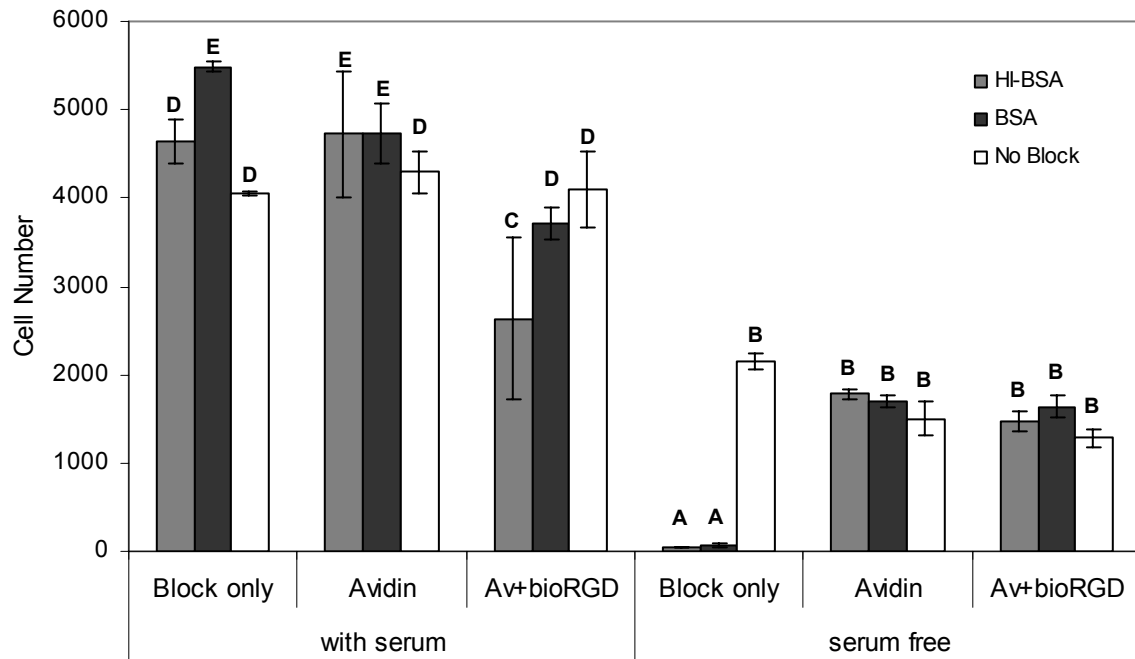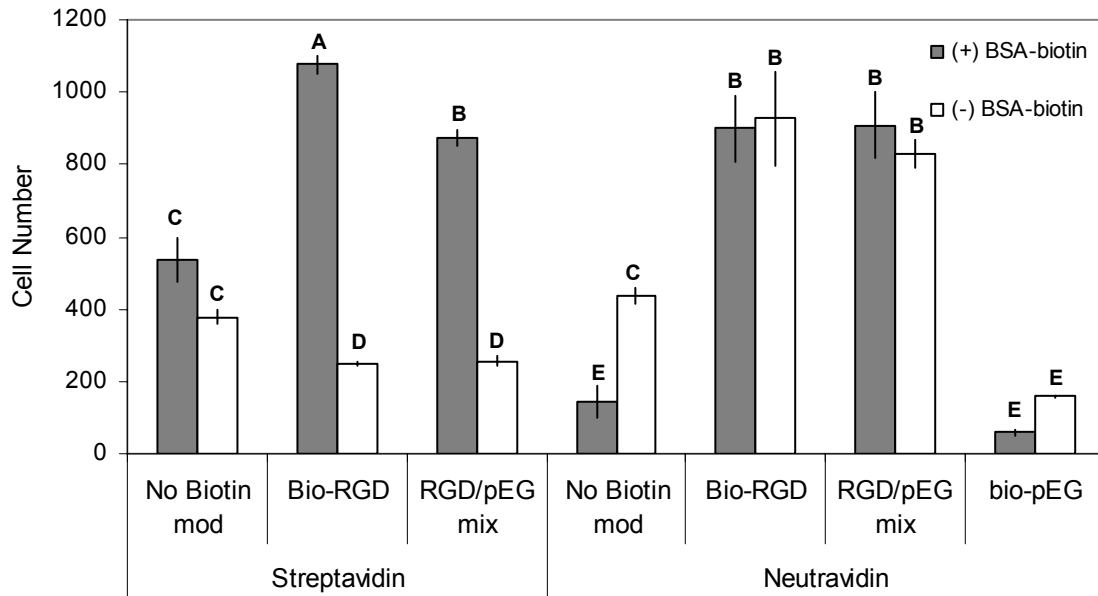
Figure 5.4. Effect of biotin-BSA on cell adhesion Groups without statistically significant differences are denoted by letters (e.g. A's are not significant from other A's, but are significantly different from other letters). Significance between groups was calculated with a $p < 0.05$ using a Tukey HSD pairwise comparison.

Based on this data, the simplest avidin based system for presenting cell binding domains was determined to be biotin-bsp-RGD(15) conjugated to physisorbed neutravidin, followed by blocking with BSA. This peptide presenting system provided a high level of cell attachment when conjugated to biotin-bsp-RGD(15), while minimizing non-specific cell adhesion when RGD was not present on the surface.

Using the BSA blocked neutravidin system, biotin-bsp-RGD(15) was compared to biotin-AG-73, a peptide that engages with the heparin sulfate side groups of Syndecan-1 and has been implicated in human embryonic stem cell adhesion and proliferation.[110] For this experiment, hMSCs were plated into 24 well culture plates and imaged at two hours and one day to examine both density and cell morphology, and the resulting images are shown in Figure 5.5. The left set of images (a-d) show mixtures of various percentages of biotin-bsp-RGD(15) and biotin-RGE, to determine how the degree of surface coverage of cell adhesive peptide controls adhesion. Cells attached and spread down to a 50-50 mixture of RGD and RGE, while at 40% RGD and below cell attachment was sporadic and the cells remained rounded on the surface (d).
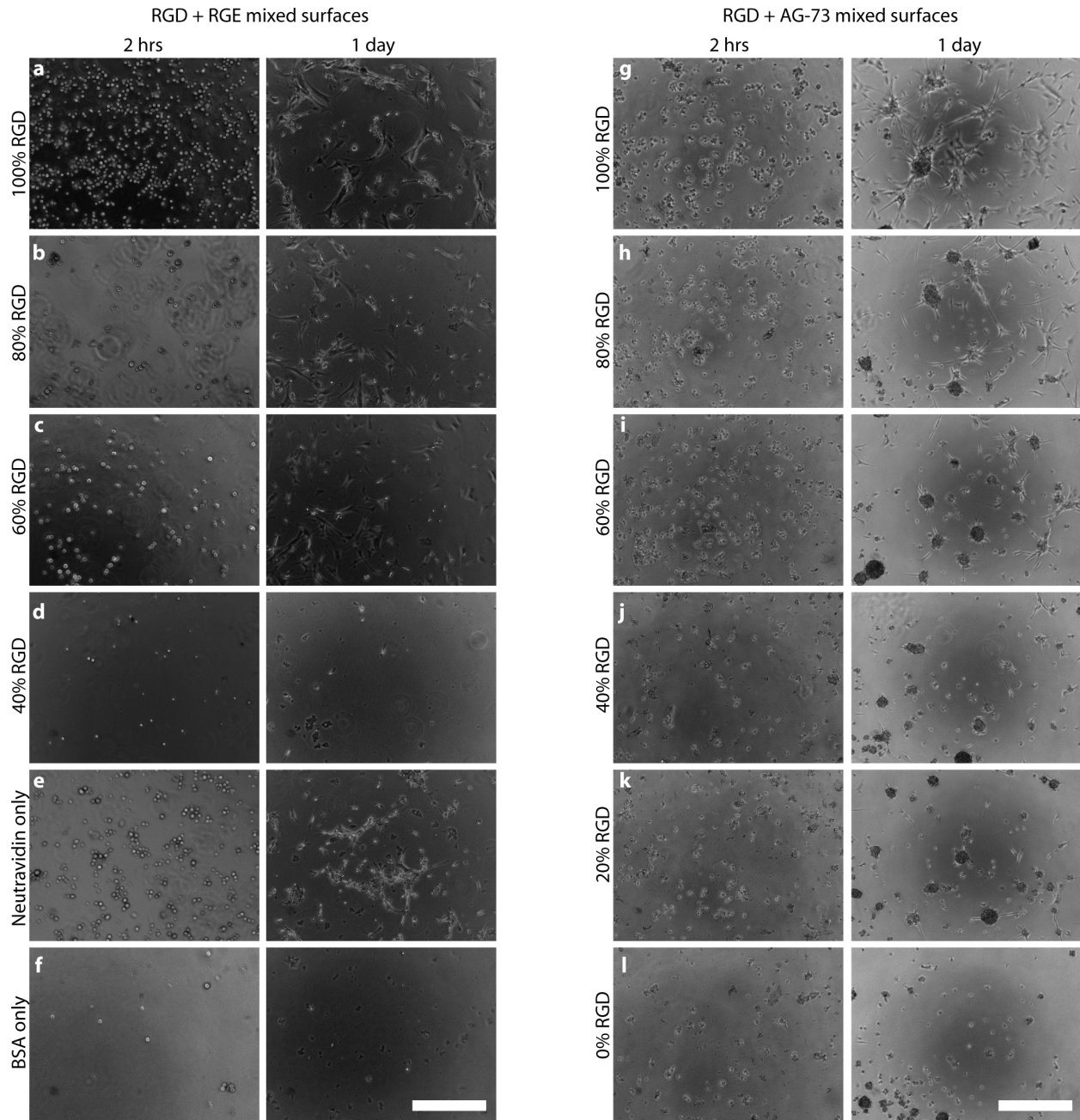
Figure 5.5. hMSCs attached to different peptide concentrations on polystyrene. Cells were attached on various mixtures of biotin-bsp-RGD(15) and RGE (a-d) or mixtures of biotin-bsp-RGD(15) and AG-73 (g-l). Controls of only neutravidin and BSA blocked surfaces are shown in (e-f). (sb = 200 microns)

In biotin-bsp-RGD(15) and biotin-AG-73 peptide mixtures, shown in the right set of images of Figure 5.5 (g-m), cells were adhered to all combinations of peptide, from 100% RGD to 100% AG-73. However, at 40% RGD and below, cells did not spread and form spindle like morphologies that are normally observed for hMSCs. It was also observed that the cells formed colony like masses on the surface on substrates presenting AG-73 peptides. (h-m)

50

### 5.4 - Discussion

In this chapter, the influence on cell adhesion for a variety of avidin derivatives and biotinylated peptides was examined.  A range of avidin derivatives were deposited, including avidin, neutravidin, streptavidin, and a streptavidin that had been modified to include cell adhesive RGD groups.  A variety of biotinylated molecules were also examined, including biotin-bsp-RGD(15) and biotin-AG-73 as cell adhesive ligands, and biotin-pEG and biotin-RGE as negative controls.  Neutravidin and biotin-bsp-RGD(15) provided the most robust cell adhesive substrate modification, while minimizing background adhesion to the neutravidin protein.  pEG or RGE modification was sufficient to eliminate cell adhesion as well.  Both blocking with BSA and removal of serum from the media were necessary to prevent background adhesion to the polystyrene, regardless of the avidin/biotin scheme used.  Preadsorption of a biotinylated BSA molecule before avidin conjugation resulted in greater cell adhesion for the streptavidin/biotin-bsp-RGD(15) system, but did not enhance cell adhesion for neutravidin coated substrates.  One possible mechanism for the difference in cell adhesion for stretpavidin conjugation could be denaturation of the streptavidin protein upon adsorption onto the polystyrene, resulting in a decrease in its ability to conjugate biotin efficiently.

Based on the data presented in this chapter, it was determined that neutravidin and biotin-bsp-RGD(15) would be used for future cell studies on ablated surfaces.  The neutravidin/biotin-bsp-RGD(15) system showed high cell affinity, even without the preadsorption of biotin-BSA prior to neutravidin deposition, while minimizing background adhesion when RGD moieties were not present. This deposition scheme allowed us to manipulate the type and density of the peptide deposited and presented the peptides from the surface in an ordered and controlled manner.

# Chapter 6 - Patterns to control cell behavior

## *6.1 - Introduction*

An overall goal of this thesis was to create a modular, flexible cell culture platform with better control over the input variables to the cell than typical micropatterning methods. Such a platform would ideally have a number of advantageous properties: control of the size and pitch of cell adhesion domains positioned on a non-fouling background; amenable for a wide variety of substrates; sufficient throughput to create the large number of samples required for a cell studies; and, ease of accessibility to biological researchers. The patterning platform developed in this thesis meets many of these goals and also does not require specific chemistry to conjugate biomolecules, allowing wide range of proteins or peptides can be patterned by simple physisorption.

Spatially controlling the distribution of extracellular matrix proteins or their peptide mimetics on the micrometer length scale has been shown to have a profound effect on a number of cellular events, such as cytoskeletal organization,[111] proliferation,[1, 5, 9] differentiation,[3, 7, 10, 112, 113] and gene expression.[6] Changes to the cytoskeleton lead to altered stress levels imparted on the nucleus,[70, 114, 115] believed to affect organelle and DNA organization and distribution, ultimately altering or controlling cell fate. One hypothesis to explain the mechanism of this effect involves the continuous physical linkage between cytoskeletal elements and the nuclear matrix, via extracellular matrix (ECM)-integrin engagement, which can alter DNA topography and transcription.[116] Gene expression and protein production have been altered by changing nuclear shape of cells isolated on patterned substrata.[6] However, these micron scale studies have been limited by the inability to directly control the ligand input into the cell via the focal adhesions it forms with the substrate. This limitation has prevented independent examination of the effect of ligand type, density, and nanoscale distribution in controlling cell fate, ultimately hindering a mechanistic analysis of more global cell behavior observations.

Controlling protein or peptide presentation on the nanometer length scale allows for direct arrangement of individual proteins or cellular components, providing researchers with a powerful tool to investigate the relationship between cell area, ligand density, focal adhesion size, and ligand spatial arrangement on cell fate and function. A number of techniques exist for generation of nanoscale spatially resolved chemistries, but each technique has its own advantages and limitations, as reviewed in Chapter 2. Scanning probe based lithographies suffer from scale-up issues,[17, 22, 24] while electron beam lithography requires special processing environments and substrates, as well as access to an electron beam source.[117, 118] Lithographical techniques involving colloidal distributions or copolymer demixing are fast and cost effective, but are limited in the types of patterns that can be generated by the physics of the systems.[52, 56] We have developed a technique that involves femtosecond laser ablation of an non-fouling ultrathin (10-20nm) poly(ethylene glycol) (pEG) polymer film, exposing the underlying quartz or glass substrate and creating unprotected regions that can be further modified as focal adhesion domains. This will allow us to vary the peptide density within the subcellular region of the pattern itself, and to create patterns that can interrogate the effect of integrin clustering and size on focal adhesion formation and cell spreading.

This chapter presents a variety of nanoscale patterns of cell adhesion domains that were created to probe cell response to the density and overall spatial arrangement of adhesive ligands presented. Gradient patterns of feature pitch and diameter were created to probe the minimal

ligand density required for cell adhesion and outgrowth. We also selected two peptide densities identified from the literature, 0.03 pmol/cm$^2$ and 1 pmol/cm$^2$,[52, 119] to create isometric pitch samples surrounded by non-binding regions. Using these guidelines, patterns were generated to present the same projected density using differing feature geometries.

## 6.2 - Methods

### 6.2.1 - Surface preparation

Surfaces were prepared as described in Chapter 3. Briefly, cleaned quartz substrates were treated with oxygen plasma and silanized with a 1% brominated silane initiator from 94% anhydrous methanol and 5% water, with 1 mmol acetic acid. Following a bake at 110°C for 30 min, samples were reacted in a solution containing 1 mmol CuBr, 2 mmol bipy, 0.3 mmol CuBr$_2$, 12 ml methanol, and 3 ml degassed water under nitrogen until the desired thickness was reached (~ 6 hrs for a 10 nm thick layer). Thickness was verified prior to ablation by including a silicon sample and measuring film thickness using a Filmetrics F20 spectral reflectometer (Manila, Spain). Samples were nanomachined to give the desired patterns with a variety of lenses and fluences to achieve the desired feature size based on the parameters outlined in Chapter 4.

### 6.2.2 - Ligand density measurement

Ligand density was measured as previously reported.[120] Briefly, a fluorescently labeled analog to the cell adhesive domain of bone sialoprotein (bsp), biotin-CGGNGEPRGDTYRAYK(FITC)GG-NH2 (American Peptide, Sunnyvale CA) , which we termed **biotin-bsp-RGD(15)(FITC)** was conjugated to an avidin activated quartz surface, as described above. Following conjugation, samples were immersed in 500µl of a digestion buffer containing 1 mg/mL of high purity bovine pancreas chymotrypsin (Calbiochem) in 10 mM tris-HCl buffer (100 mM CaCl2, pH = 8.0) for 30 min. Unpatterned pEG modified substrates were also included to account for background fluorescence resulting from protein adsorption to the sides and bottoms of the substrates. Following digestion, 100µl of the digestion buffer over each substrate was pipetted into a 96 well plate, and the fluorescence was read in a SpectraMax Gemini XS flourometer (Molecular Devices, Sunnyvale, CA). These values were compared against a standard curve generated by serial dilution of unconjugated peptide in the digestion buffer, and the surface peptide density was back calculated using the substrate area.

### 6.2.3 - Cell culture

Bone marrow derived mesenchymal stem cells (MSC), previously isolated from Sprague Dawley male rats, were cultured in Dubellco's Minimum Essential Media (DMEM) supplemented with 15% fetal bovine serum (FBS) and 1% penicillin-streptomycin at 5% CO$_2$ and 37C. Media was replaced every 2-3 days and the cells were passaged approximately once per week. Human mesenchymal stem cells (hMSCs) were cultured in MSC growth media (Lonza) containing 10% FBS, 1% gentamicin, and 1% L-glutamine. Media was replaced every 3-4 days and the cells were passaged once per week, at ~90% confluency. NIH-3T3 murine fibroblasts were used in the video microscopy experiments and were cultured in CO$_2$ independent media containing 10% FBS and 1% penicillin-streptomycin.

### 6.2.4 - Video microscopy

Time lapse imaging was done on a custom built video microscopy system, constructed and run by Hojeong Jeon in the Laser Thermal Lab. NIH-3T3 murine fibroblasts were seeded onto a patterned surface in a temperature controlled chamber in $CO_2$ independent media. Images were captured at regular intervals using a CCD camera (Q-imaging) over the course of 21 hours.

### 6.2.5 - Staining protocol development

During staining cells were found to peel or rapidly detach from our nanopatterned surfaces, likely due to the reduced adhesive ligand signal available to the cell. Upon peeling, actin residue would frequently still seen adhered to the surfaces, indicating that interaction between the cell surface receptors and adhesive ligands was at least sufficient to maintain protein adhesion after the cells were removed. Weak binding on the patterned surfaces, potential cell contraction, or some combination of the two were thought to be the main contributors to this problem. Weak adhesion could be caused by weak protein-substrate interaction due incomplete film removal or repolymerization of pEG in the crater bottom, the spacing and interstitial pEG film between the individual adhesive islands, or inability of cells to access the peptides in the bottom of the craters.

A number of fixation methods were tried, including fixation in various percentages of paraformaldehyde (1-4%), methanol, and acetone. Methanol and acetone fixation is typically done at low temperature (-20C), and the rapid cooling of the cells frequently caused them to contract and detach from the surface. The number of rinses required also caused cells to be removed from the surface, especially when present in large sheets or multilayers. In order to minimize cell exposure to large temperature differences and minimize potential contraction caused by rapid formaldehyde polymerization, a one pot staining method was developed using low percentages of PFA and Triton X at 37C. As they are small molecule stains, DAPI and phallodin were simply included in the fixation/permeabilization solution in order to simultaneously stain the cells. This minimized the number of rinse to two both prior to and after fixation/staining.

### 6.2.6 - Staining and nuclear shape analysis

Nanopatterned substrata were seeded at $10^5$ cells/cm$^2$ with mesenchymal stem cells (MSCs, human or rat) in DMEM without serum. Cells were allowed to attach for 24 hrs onto the substrates, gently rinsed with media to detach weakly adhered cells, transferred to fresh wells, and covered with normal growth media. Cells were fixed and permeabilized in 1% paraformaldehyde and 0.05% Triton-X. The substrates were incubated in 0.5 μM fluorescent phalloidin (rhodamine or Alexa488 conjugated, Molecular Probes) and 1 μg/mL DAPI (Molecular Probes) to visualize actin and nuclei respectively. Spacers were inserted around the samples to prevent compression; a drop of SlowFade (Molecular Probes) was placed onto the sample followed by sealing against a coverslip.

Fluorescence micrographs were captured with an IEEE 1394 CCD camera (Q-imaging) on a Nikon TE300 inverted microscope, or via confocal microscopy on a Zeiss 510 Meta. The nuclear shape index (NSI) was calculated by dividing the maximum x-y area by the overall height of the nucleus. Z-stack images of the nucleus were collected under identical exposure, gain, and scan speed settings and thresholded to determine cross sectional areas and the highest and lowest slice for each nucleus. To determine if the observed differences in nuclear shape

were significant, NSI measurements were compared using analysis of variance (ANOVA) followed by a Tukey HSD pairwise comparison, with a cutoff value of p< 0.05.

## 6.3 - Results

In this chapter, femtosecond laser nanomachining was employed to create a wide range of patterned geometries to probe cell attachment and morphology. One advantage of our particular patterning scheme was that we were able to generate large area surface patterns with a variety of feature arrangements on a single substrate, where typically scanning probe lithographies are typically limited to scan areas of 100x100 microns and colloidal lithographies are limited to a fixed geometry across an entire cell culture surface unless more exotic combinations of techniques are used. To show the flexibility of our patterning process, a variety of substrates were created, including one dimensional and two dimensional gradients of individual feature pitch, line patterns with variable pitch between lines, and isometric pitch patterns designed to control presented ligand surface density by changing pitch and feature diameter, as shown in Figure 4.9.

### 6.3.1 - Time lapse microscopy of cell adhesion to nanopatterns

Cell adhesion to our nanopatterned substrates proved difficult in the early stages of the project. Checking cells after one day of adhesion frequently revealed no cell adhesion, large masses or multilayer sheets of cells, or single layers of distributed cells. We hypothesized that these different outcomes could be caused by low adhesion ligand density or swelling of the polymer chains beneath the cells. Cell clumping and uneven growth across a substrate could also be caused by lack of sufficient ligand density, as well as incomplete resuspension of cells prior to plating.

In order to obtain a comprehensive picture of cell interaction with our nanopatterned substrates, various patterns were generated on a single substrate and seeded with NIH-3T3 fibroblasts in $CO_2$ independent media and visualized under a custom built, temperature controlled microscope chamber with time lapse imaging capabilities. Following cell seeding, time lapse images of the cell were captured at regular intervals over the course of 21 hrs. Figure 6.1 shows selected image captures at regular intervals, 1.75 hrs apart. The patterned areas that are visible in frame, including both vertical and horizontal heavily ablated marking lines that intersect in the bottom left corner, and (from left to right) an isometric pitch area, a 1D gradient, and a 2D gradient. As a reference, a sample still at the bottom of the figure outlines the patterned areas with dashed boxes. Features designed to isolate single cells also continue further to the right, but are out of frame of the video (these features are also shown in Figure 4.9).
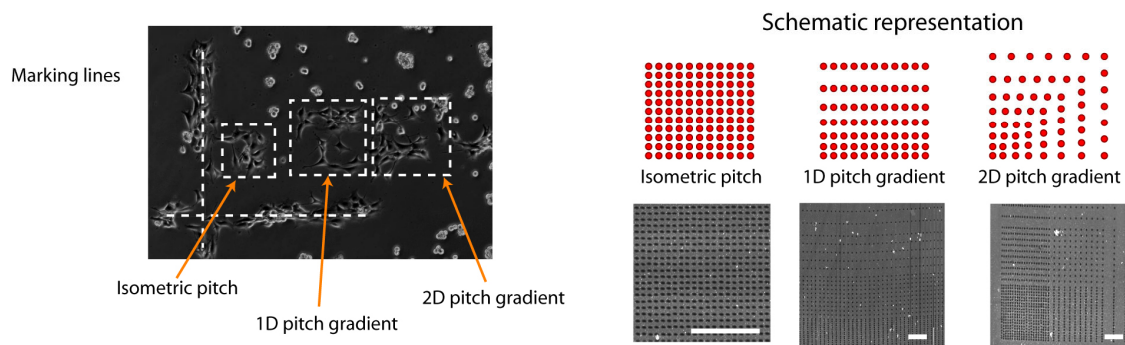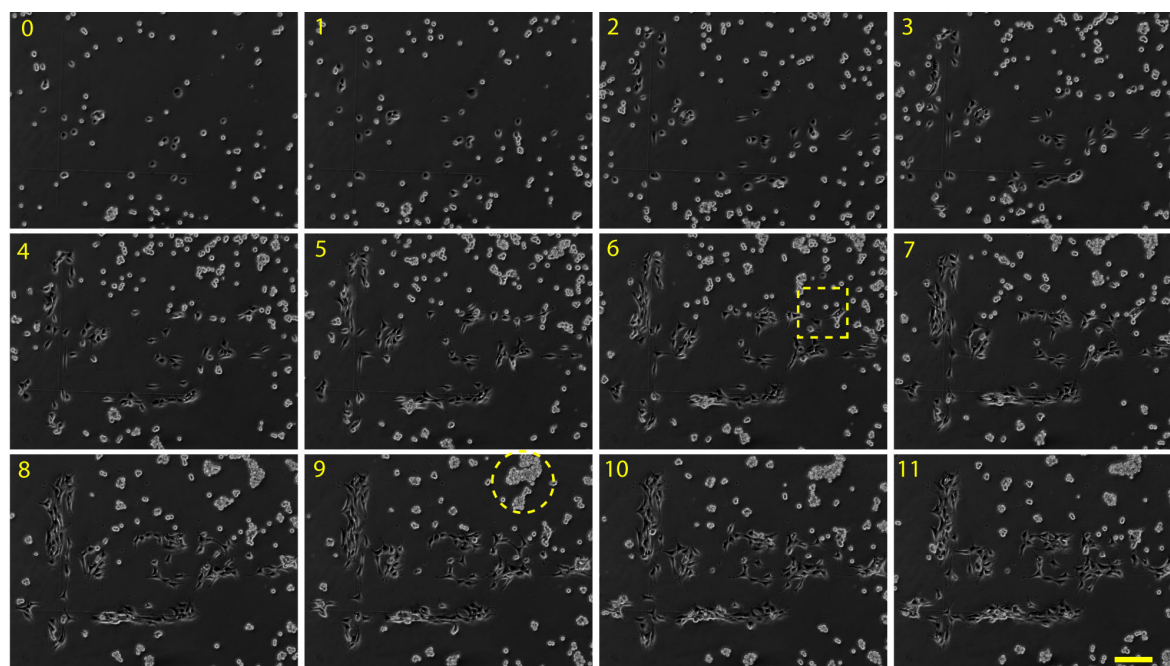
Figure 6.1. Frame captures from video of NIH-3t3 attachment over 21 hrs on various patterned geometries, with each frame corresponding to roughly 1.75hrs. Cell image scale bars are 100 microns, AFM scale bars are 10 microns. Cells in non-adhesive regions were observed to clump together (dashed circle in (9)), while cells encountering gradient patterns were observed to move towards higher density features (dashed square in (6)).

Video microscopy allowed us to make a number of critical observations. First, it is evident that cells are well dispersed across the substrate (Image 0) and are not clumped prior to seeding. As time progresses, rounded cells can be seen to clump into rounded cell aggregates while remaining untethered to the surface along the top of the video frame in unpatterned regions. An example is highlighted with a dashed circle in Image 9. The lower density area of the 2D gradient is highlighted in Image 6, where cells were observed to interrogate, attach to the surface, and then migrate to the higher density areas to the lower left.

Mesenchymal stem cells were observed to adhere and spread where adhesive ligands were presented from the nanopatterns, while forming balled aggregates in non-adhesive regions. These aggregates were not germane to this video experiment, as large spherical cell masses were observed on other patterned substrates. Reexamining Figure 5.5, cell aggregates similar to those observed on in the video microscopy can be seen in the RGD/AG-73 copeptide surfaces for RGD

concentrations of 80% or lower after 1 day.  Although similar aggregates were not observed for RGD/RGE mixed surfaces after one day, the video micrsoscopy experiments suggest that the "adhesiveness" or overall ligand density of the surface is a critical factor in this aggregation behavior, as these cell aggregates form on the unnpatterned pEG background.

### 6.3.2 - Estimation of peptide density on patterned surfaces

To estimate the peptide surface density both theoretical and experimental approaches were employed. A simple packing model was used to calculate the amount of protein physisorbed into the ablated features.  It was assumed that neutravidin was a spherical protein of 5 nm in diameter,[121] and packed into features in a hexagonal conformation without denaturing. In this manner, an average of two biotin binding sites were available for peptide conjugation per avidin molecule. Under these assumptions, a surface plot was generated for exposed peptide density available to a cell based on the ablated feature diameter and spacing (Figure 6.2).
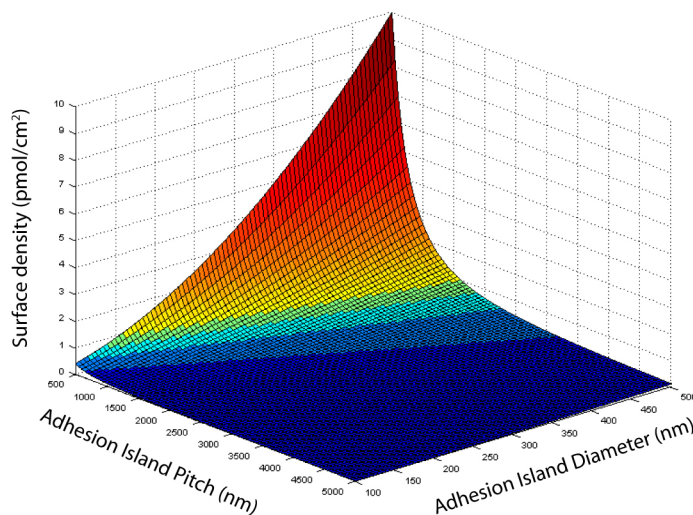


Figure 6.2. Estimated peptide surface density for Neutravidin/biotin-bsp-RGD(15) system based on packing model.

To verify our model, we used a previously developed fluorescence assay to determine the peptide surface density of a bare, cleaned quartz substrate that had been physisorbed with neutravidin and biotin-bsp-RGD(15)(FITC).[120] The fluorescent end group of the peptide sequence, designed to be cleavable by chymotrypsin, was released from the peptide chain and the fluorescence of the supernatant solution was measured.  These values were compared against a standard curve generated by serial dilution of unconjugated peptide in the digestion buffer, and the surface peptide density was back calculated using the substrate area, yielding an overall surface density for a homogenous avidin/biotin-bsp-RGD(FITC) coated substrate of ~ 12.0 pmol/cm$^2$.  This value is within 5% of our calculated estimate of 12.6 pmol/cm$^2$, confirming the value of our model.  As we are assuming that the peptide packs with the same conformation on patterned and unpatterned surfaces, the overall projected surface density is identical for surfaces with identical exposed area in the craters.  With our nanofabrication method the total ligand input into the cell can be modulated independently via the ablated feature diameter and spacing variables, allowing exploration of the effect of a range of factors on stem cell fate and function.

### 6.3.3 - Minimal ligand Density for cell adhesion

In order to determine a minimal ligand density for cell adhesion, one dimensional gradients of clustered peptides were patterned by either fixing laser fluence (to keep feature diameter constant) while varying the pitch between individual features or varying laser fluence (and thus feature diameter) for a fixed pitch.  It should be noted that these are not true gradients; instead, regions of isometric features were created directly adjacent to one another, such that the feature diameter or density were decreased across the sample surface.  Figure 6.3 shows hMSC adhesion to gradients of pitch (a-c) and feature diameter (d-e) for cells after 3-7 days, with the alternating black and white scale bar indicating a region of changed feature geometry.  For each sample (a-c), pitch was increased every 200 microns of vertical distance traveled.  Gradients (a-b) had constant feature diameter of 700 nm, while (c) had a constant feature diameter of 500nm. The sample shown in (d) featured decreasing feature diameter that was changed every 50 microns and ranged from 750 nm to 350 nm.  Gradient (e) also featured decreasing feature diameter, ranging from 900 to 500 nm.
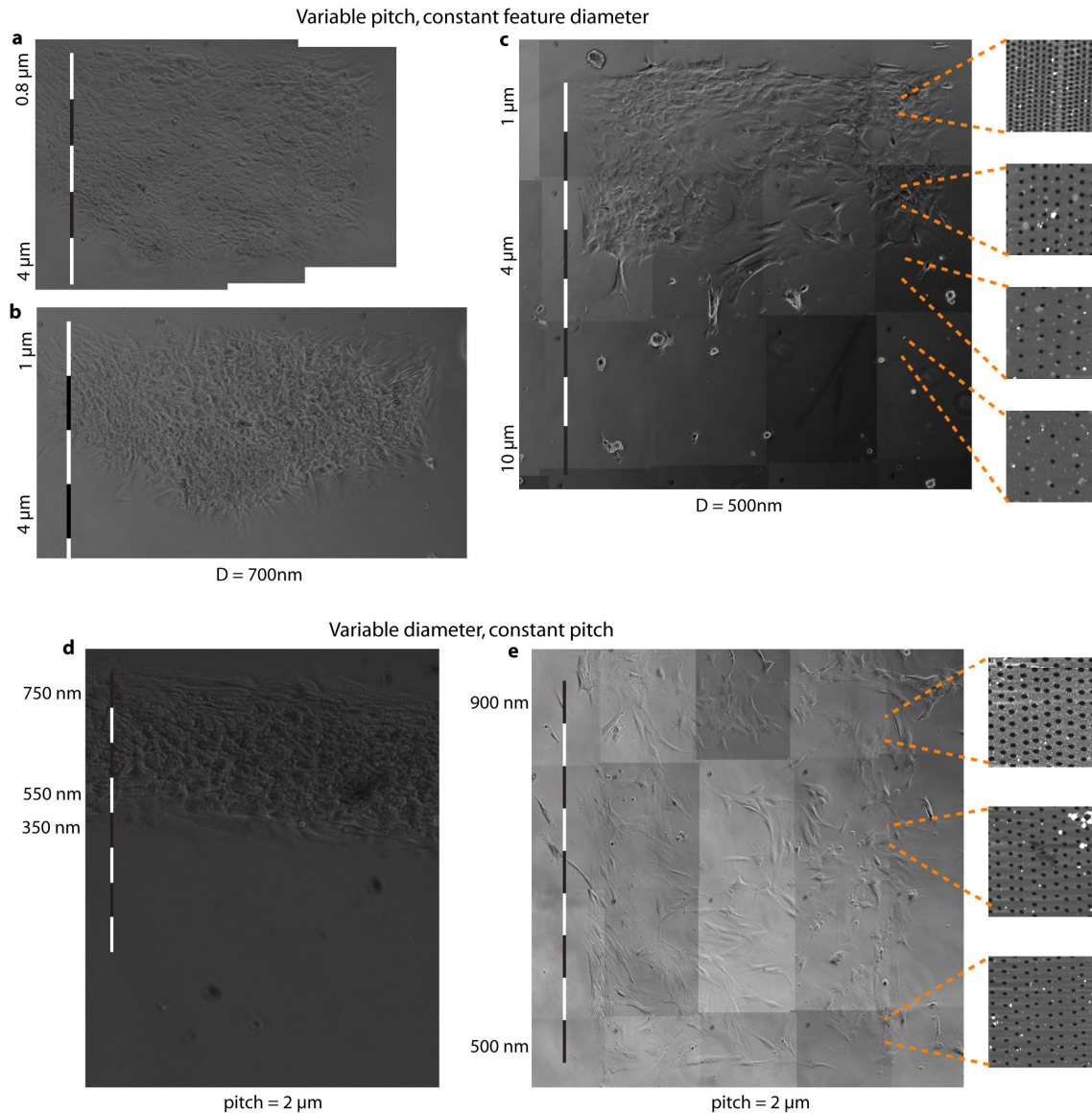
Figure 6.3. Composite phase contrast images of hMSC attachment to gradients of feature pitch (a-c) with constant feature diameter, as well as gradients of feature diameter with constant pitch (d-e). Each black/white bar on the left of the composite images corresponded to a transition to a different feature pitch/diameter. These transitions were every 200 microns, except for (d) where the transition is every 50 microns. Sample AFM scans are given on the right of the of the images (AFM images are 15 microns on a side)

    For varying pitch (a-c), hMSCs completely covered the areas ablated having 3 micron pitch, with a transitional region of some cell attachment and spreading into the 4 micron pitch zone and no attachment at pitches greater than 5 microns,. Feature diameter gradients (d-e) showed varying results. hMSCs plated on a feature gradient with a constant pitch of 2 microns and a much smaller patterned area (d) initially adhered in a multilayered sheet on areas with feature diameters greater than 500 nm, followed by partial outgrowth into the 375 nm features by day 3. In (e), the diameter gradient ranged from 500-900 nm, with cells adhered and spread across the entire patterned area in a more isolated and spindle-like formation that is typically seen in normal

cell culture. Table 6.1 presents projected surface densities for the positions on the gradients where cell outgrowth was observed to halt. For the diameter gradient shown in (d), the adhesion cutoff value seems to be approaching 0.25 pmol/cm$^2$, as the cells were able to partially grow onto the 375 nm diameter features. Similarly, the pitch gradients seem to yield a cutoff value between 0.15 and 0.3 pmol/cm$^2$.

Table 6.1. Projected peptide densities for cell adhesion cutoffs observed on gradient samples.

| Pitch (μm) | Diameter (nm) | Projected density (pmol/cm$^2$) | Gradient feature |
|---|---|---|---|
| 2 | 375 | 0.25 | Diameter |
| 2 | 500 | 0.6 | Diameter |
| 4 | 500 | 0.15 | Pitch |
| 4 | 700 | 0.3 | Pitch |

## 6.3.4 - Ligand density effect on nuclear shape

To determine if ligand density, focal adhesion size, and pitch effected overall cell morphology and cytoskeletal tension, regular arrays of adhesion domains were created in pEG thin films using two pulse energies and variable pitch to generate patterned areas containing different feature geometries designed to project the same overall peptide density to the cell. Using the avidin packing model to estimate peptide density, arrays of adhesion domains were to generate patterned areas projecting different peptide surface densities identified in the literature as possible critical surface densities for cell adhesion.[52, 120] An overview of the features created are summarized in Table 6.2. Single lines of adhesion domains were also ablated at pulse energies of 91nJ and 1 μm pitch between each adhesion spot. A control substrate was created by exposing clean quartz to the identical avidin-biotin binding conditions as patterned substrates, creating a homogenous surface of exposed ligand.

Table 6.2. Summary of isometric pitch features.

| Pulse energy | Feature Pitch | Peptide density | Cell attachment | NSI | Figure |
|---|---|---|---|---|---|
| 70 nJ | 8 μm | 0.03 pmol/cm$^2$ | Few | 8.3 +/- 3.2 | Figure 6.4a |
| 70 nJ | 2 μm | 1 pmol/cm$^2$ | Y | 16.3 +/- 6.8 | Figure 6.4b |
| 60 nJ | 4 μm | 0.03 pmol/cm$^2$ | Y | 11.6 +/- 3.9 | Figure 6.4c |
| 60 nJ | 1 μm | 1 pmol/cm$^2$ | Y | 22.0 +/- 5.2 | Figure 6.4d |
| Control | | 12.6 pmol/cm$^2$ | Y | 13.6 +/- 7.6 | Figure 6.4e |
| 91 nJ | 1 μm (line) | 9.97 pmol/cm$^2$ | Y | 7.6 +/- 1.7 | Figure 6.4f |

Rat bone marrow derived MSCs attached and spread on all domain sizes and pitches, with well established stress fibers and focal adhesions. However, at the lowest peptide density, 0.03 pmol/cm$^2$, we observed mixed results, where cell adhesion was dependent on a combination of adhesion domain size and spacing, as shown in Figure 6.4. For example, MSCs were well attached and formed stress fibers on surfaces with 250 nm domains spaced at 4 μm (c), but for samples with 500 nm features spaced at 8 μm (a) there were few cells attached, and those that attached were less spread with poorly developed cytoskeletal elements. These results suggest the

arrangement of ligand presentation is just as critical as the total ligand surface density and receptor-ligand affinity. These data are consistent with a critical peptide density defined by presenting clustered adhesion ligands, suggesting that ~ 0.03 pmol/cm$^2$ may be a limiting peptide surface density for integrin-mediated cell adhesion;[52] however, this clearly depends on the size and spacing of the nanoscale adhesion domains, ligand-receptor affinity, and cell type.
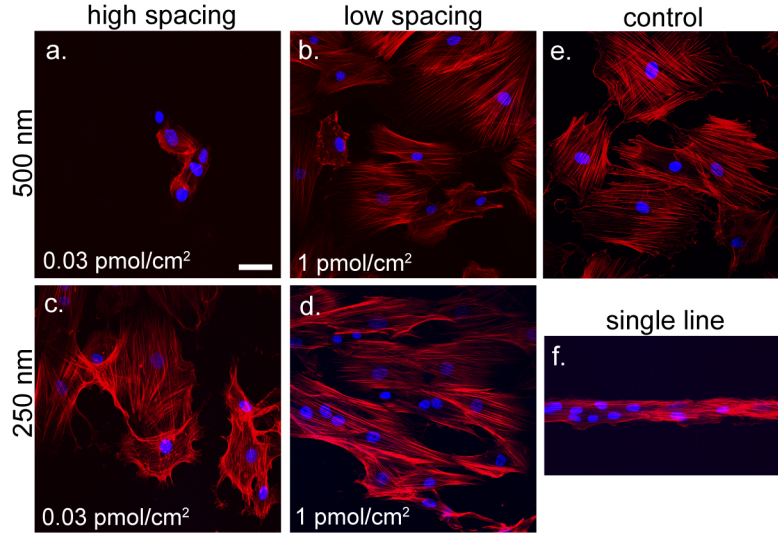


Figure 6.4. Rat mesenchymal stem cells adhered onto the features described in Table 1. Fewer cells attached on 500 nm features with 8 μm spacing and had less developed cytoskeletal elements (a). Cells were well adhered with highly developed cytoskeletons for 500 nm features with 2 μm spacing (b), 250 nm features with 4 μm spacing (c) or 1 μm spacing (d), and homogenous controls (e). Cells were also observed to form elongated structures on ablated single lines with 1 μm spacing (f)  (scale bar = 50 μm).

We also observed MSCs to be more densely packed onto surfaces with high peptide density, as well as having morphological differences and significant differences in their nuclear shape, quantified by nuclear shape index (NSI). The NSI of each nucleus was obtained dividing the maximum x-y area of the nucleus by the overall nuclear height. Data were grouped according to statistical significance, calculated by ANOVA and a Tukey HSD post hoc test with $p<0.05$, revealing two statistical groups (Figure 6.5). Patterns with lower overall peptide surface density showed statistical differences in nuclear shape from the higher density features (top bar). Cells also attached and aligned on domains arranged as single lines, and these feature arrangements were also statistically significant from the higher density features as well as the homogenous control.  Line patterns have a much higher projected ligand density but the lowest average NSI, implying that the arrangement and presentation of adhesive ligands beneath a cell can influence nuclear distension regardless of the input to the cell.
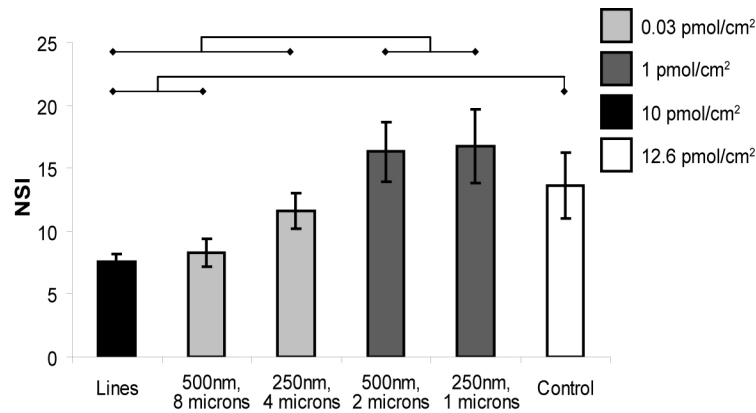
Figure 6.5. NSI analysis of isometrically nanopatterned hMCs. Significant differences were observed in nuclear shape between surfaces designed for high and low overall surface peptide densities. Error bars indicate standard error of the mean, and statistical significance was determined using ANOVA followed by a Tukey HSD post-hoc comparison.

## 6.4 - Discussion

In this chapter, varying cell types were attached to a variety of patterns to explore the interplay between adhesive island dimension, arrangement, and overall projected density on cell adhesion and nuclear shape. Video microscopy and density gradient patterns confirmed that cells will migrate to regions of higher ligand density, with a cutoff value of "cell adhesion preference" in the range of 0.15-0.3 $pmol/cm^2$. For patterns consisting of ablated lines, densities were above this cutoff point for all geometries, except for the 50 micron pitch lines designed to isolate single cells. On these line patterns, high density areas (greater than 1.7 $pmol/cm^2$) supported the growth of dense, colony-like clusters of cells while lower density (less than 1.7 $pmol/cm^2$) isolated cells or groups of cells were observed. The 1.7 $pmol/cm^2$ areas seemed to form a transitional zone, with cells clustered together but not in a high density cell mass.

When hMSCs were isolated on patterns of a single feature diameter and pitch, as shown in the isometric NSI study, much lower peptide densities (down to 0.03 $pmol/cm^2$) than the critical density calculated for the gradient surfaces yielded cell adhesion, including cell adhesion on patterns with 8 micron feature pitch. Cells were confined to the isometric patterned areas due to interstitial pEG boundaries, negating any directional migration up a density gradient. As the cells would be "forced" to attach where they landed, this could explain the differences in adhesion seen between the gradients and the isometric samples. Patterned surfaces with higher project peptide densities had significantly higher NSI that those with lower projected densities, suggesting that the overall ligand input to the cell directly influences the cytoskeletal tension within the cell, and subsequently nuclear distension.

However, the overall ligand density is not the only factor that influences cell morphology, as evidenced by the differing critical values noted between the line patterns, gradient patterns, and isometric pitch patterns. During the NSI analysis, notable differences were observed in morphology and cell adhesion between the 4 and 8 micron pitch samples. Compared to the line patterns (shown in Appendix A), a similar transition was evident between the 4 and 8 micron pitch samples though the line patterns project a much higher peptide density. Though cell attachment was observed in both cases 8 microns may be approaching a critical pitch across which cells are unable to readily extend. NSI for cells isolated on single line patterns with high

underlying peptide density was also significantly lower than seen on cells spread on high density features, indicating that constraining morphology can influence intracellular tension independent of underlying peptide density.

For unconstrained cells plated on the gradient and isometric pitch samples, two critical peptide densities were identified. A critical ligand density in the range of 0.15-0.30 pmol/cm$^2$ was identified on gradients of spacing and pitch for cell adhesion and growth. On isometric pitch samples, a critical density of 0.03 pmol/cm$^2$ was observed at which nuclear distension was significantly reduced. The higher critical density for adhesion seen on the gradient samples was likely due to the cells having the ability to migrate up the gradient to higher densities. In contrast, cells on the isometric pitch samples were trapped on specific densities by surrounding unpatterned pEG brushes. These values agree with adhesion densities identified in the literature for integrin activation in fibroblasts[52] and osteoblast mineralization[119]

In this chapter, we demonstrated that nanopatterned substrates support cell adhesion and growth. Video microscopy revealed that well dispersed cells will adhered and spread on patterned substrate areas, migrate to higher densities, and form aggregates in the unpatterned regions. Gradient and isometric pitch samples identified two critical densities, 0.15-0.30 pmol/cm$^2$ was observed as a cutoff value, below which MSCs migrate away from when a higher density is present. The nuclear shape study found that controlling underlying projected surface densities, as well as cell morphology, can significantly alter the nuclear morphology of the cell. This suggests that the intracellular tension within the cell is fundamentally changed, which could presumably lead to changes in cell fate.

# Chapter 7 - Conclusions and future directions

This chapter will outline the results and conclusions that can be drawn from this thesis, as well as providing ideas for future experiments and directions. The first section will outline the experimental results, while critical analysis of the various elements of the patterning technique will be saved for the conclusions section.

## *7.1 - Results Summary*

The aim of this project was to develop a nanopatterning method for creation of cell culture substrates designed to control the input to the cell via surface mediated ligand-receptor interaction. To achieve this, a general framework was established: render a substrate passive to non-specific adsorption, tether cell adhesive ligands on sub-micron regions of the surface, and seed cells onto the surface to examine the effect of our nanopatterns on cell behavior.

### 7.1.1 - Creation of a non-fouling polymer background

Rendering the cell substrate non-fouling was achieved by directly polymerizing a pEG brush layer using a controlled radical polymerization scheme initiated directly from the surface (SI-ATRP). This was a noted departure from the use of previous materials developed in our lab, where a (pAAm-co-pEG) IPN hydrogel had been used to render both polystyrene and glass/quartz substrates non-fouling. Initial attempts were made to pattern the IPN using focused femtosecond laser pulses, but the high surface roughness of the surface made characterization of higher resolution features impossible. After attempts at varying the reaction conditions failed to improve the surface roughness to an acceptable degree, a new scheme was implemented.

A SI-ATRP synthesized brush layer synthesis was then optimized and characterized. The underlying roughness of the silane initiator was minimized by changing the liquid immersion deposition solvent from anhydrous toluene to an aqueous methanol solution This change eliminated the observed deposition of hemispherical silane droplets one the surface, resulting in a low roughness profile that served as an ideal starting point for the reaction. Following the discovery that addition of a small amount of deactivating cuprous bromide provided a nearly linear, albeit slower, growth rate of the polymer from the surface, a polymerization scheme with tunable thickness was achieved. Growth kinetics were monitored *in situ* by QCM-D and by spectral reflectometry measurements of the film thickness at discrete time points. XPS verified that the surface chemistry was as expected for a pEG brush layer present on a quartz substrate, with a high peak for at carbon-oxygen bond energies.

SI-ATRP proved to be an ideal solution for our laser ablation nanofabrication needs. Aside from the aforementioned tunable thickness, the polymerized substrates showed little increase in surface roughness, with a typical final RMS roughness of under a nanometer. A 10 nm thick polymer brush also showed robust non-specific protein adsorption, with only a negligible frequency change measured on a quartz crystal oscillator under 10% serum that was immediately reversed upon reflow of PBS. The polymer also proved to have amenable ablation characteristics for laser processing, as described in Chapter 4.

### 7.1.2 - Femtosecond laser ablation

Creation of patterns involved ablating the non-fouling pEG brush layer with focused femtosecond laser pulses. At a processing wavelength of 400 nm, the polymer layer is largely

transparent to the incident laser light, necessitating a non-linear multiphoton adsorption (MPA) event in order to bridge the bandgap required for photochemical breakdown. Due to the threshold nature of ablation processes and the MPA requirement of ablation, feature sizes much smaller than the diffraction limit of the processing system were created, with creation of spot sizes down to 100 nm.

In order to delineate processing guidelines, parametric studies on the effect of laser fluence versus feature diameter for a number of combinations of film thicknesses and objective strengths were performed. For each condition, the ablation threshold of the polymer and the underlying quartz were determined by plotting the square of the feature diameter against the laser fluence, and extrapolating a linear fit to the x-intercept. Thus, an ideal processing regime was identified between the polymer and quartz ablation thresholds that would allow for various diameters of features to be generated without damaging the underlying substrate. Such processing limits were critical to minimize thermal and mechanical shock to the relatively fragile polymer layer during the ablation process. A multishot process at fluences near the ablation threshold was also attempted, but vibrations or small stage displacements caused a misalignment of features that resulted in differing focal centers for each feature.

Finally, protein adsorption was verified into the ablated craters through fluorescence microscopy and by AFM scanning before and after exposure to a protein solution. The latter was deemed necessary as many of the feature sizes on our patterned substrates were approaching or below the diffraction limit of confocal microscopy, making exact determination of protein location nearly impossible. However, the combination of these two characterization techniques lead us to believe that protein is adsorbed into the craters, as protein fluorescence is localized only to the patterned area and AFM scans reveal a crater depth change that would be expected from protein adsorption into the crater.

### 7.1.3 - Analysis of hMSC adhesion using the avidin/biotin system

A range of different avidin and biotinylated ligands were explored for use in our cell culture platform. The inclusion of biomolecules inside the ablated craters was dependent only on their physisorption from solution, the non-specific nature of which allows for a range of proteins and peptides to be patterned. For better control over the quantity and orientation of the peptide, biotinylated versions of various peptides were used in conjunction with a physisorbed avidin (or derivative). Cell quantification assays were run on a variety of surfaces modified with different albumin molecules, blocking protocols, avidin derivatives, and biotin-peptides. From these studies, it was determined that cells needed to be initially seeded with serum free media, preadsorbing a biotin-BSA layer enhanced cell adhesion for streptavidin surfaces but did not affect the already robust performance of neutravidin/biotin-bsp-RGD(15) modified surfaces. hMSCs adhered and spread on mixed peptide surfaces of RGD and RGE down to a mass ratio of 40% RGD: 60% RGE, below which minimal cell adhesion and spreading were observed. In a similar study on mixtures of RGD:AG-73 surfaces, cells initially adhered on all peptide mixtures, but after 1 day in culture cells with percentages lower than 60% RGD did not spread and formed into colony-like aggregates. For the nanopatterned substrates, physisorbed neutravidin with the biotin-bsp-RGD(15) peptide was identified as the best candidate for peptide presentation due to the low background adhesion to neutravidin modified surfaces and high adhesion to neutravidin/biotin-bsp-RGD(15) surfaces.

### 7.1.4 - Nanopatterned cell substrates

Patterned substrates were created, designed to control cell adhesion and morphology via the underlying geometry of cell-substrate adhesive domains. The diameter, pitch, and arrangement of these domains were controlled on the nanometer length scale, providing control of the cellular input through integrins and focal adhesions. Gradient samples, line patterns, and isometric pitch samples with features designed to project the same peptide densities through different feature geometries were created.

Video microscopy of NIH-3T3 fibroblasts on patterned surfaces revealed that cells formed large aggregates on the unpatterned pEG regions, similar to those observed on the RGD/AG-73 copeptide surfaces. These aggregates would occasionally encounter pattered area and flatten out into multicell sheets, or remain as spherical masses loosely tethered atop already adhered cells. Lack of significant peptide density was the likely driving force behind aggregation, but this behavior was not recapitulated on mixed RGD/RGE surfaces with low peptide densities. However, as the unpatterned mixed peptide surfaces were rinsed prior to imaging, it is possible RGD/RGE surfaces with low RGD concentrations were rinsed clean of unbound cells, while for RGD/AG-73 surfaces the Syndecan mediated AG-73 attachment provided sufficient adhesion strength to resist rinsing steps. Aggregate cell masses were also problematic for staining and NSI studies. The large numbers of cells anchored to a relatively small and homogenous signal on the patterned surface increased their tendency to peel off the surface during the staining process. The dense packing of the cells also influences cell morphology, an important factor in nuclear distension, cell cycle progression, and fate determination.

In order to determine if there was a critical ligand density for cell adhesion, gradient surfaces were created with either changing pitches or feature diameter to provide a range of ligand densities for fixed geometries. With the exception of a gradient of feature diameter in which all the projected densities were above 0.6 pmol/cm$^2$, hMSCs either adhered or migrated to the greatest ligand densities on the surface. The critical surface density for cell adhesion on the gradient surfaces was in the range of 0.15-0.30 pmol/cm$^2$. However, for rMSCs adhered on isometric pitch surfaces surrounded by non-fouling border regions, cells adhered down to 0.03 pmol/cm$^2$, suggesting that there was migratory effect on the gradient surfaces. Thus, hMSCs are able to attach to very low surface densities, but will migrate up a ligand density when presented with an option.

Finally, we were able to control nuclear distension of the cells on isometric pitch samples. This study revealed statistically significant differences in samples plated on high (1 pmol/cm$^2$) versus low (0.03 pmol/cm$^2$) surfaces. Differences in NSI were not seen in samples with identical projected peptide densities but different feature geometries (pitch, diameter), although notable morphological and cytoskeletal differences were observed on the 0.03 pmol/cm$^2$ samples when features were changed from 500 nm diameter/8 micron pitch to 250 nm diameter/4 micron pitch. Qualitatively speaking, there appears to be a pitch value for feature spacing around 4 microns for which the ability of a cell to spread across a passivated region becomes hindered. The critical density of 0.15-0.30 pmol/cm$^2$ on gradient surfaces and the 0.03 pmol/cm$^2$ density on isometric pitch surfaces resulted in changes in cell adhesion and nuclear distension. These indicate that adhesion ligand density plays a significant role in attachment and intracellular stress. However, differing nuclear shapes and morphologies on cells constrained to line patterns suggest that cell morphology and adhesion domain geometry also play a critical role in nuclear distension.

### 7.2 - Conclusions

The pEG brush layer synthesized by SI-ATRP proved to be a near ideal solution to the requirements of our nanopatterning technique. Due to the near linear reaction kinetics, slow growth rate, localization of polymerization to the surface, and low PDI, the surface generated can robustly resist protein adsorption, be grown to a range of thicknesses by controlling reaction time, and has minimal surface roughness. The rate of polymerization can also be controlled by altering the amount of the cupric bromide/bipy catalyst system or the initial monomer concentration in the solution. The slow reaction kinetics and growth directly from the surface likely resulted in a pEG chain density on the surface that exceeds what would be possible with a "grafting to" strategy, conferring robust protein adsorption resistance. The density of the chains, regularity of the rate of polymerization, and lack of unwanted termination mechanisms also combined to provide a surface with less than 1 nm RMS surface roughness, critical to our characterization of patterned features with AFM.

Femtosecond laser nanomachining offers a number of significant advantages over currently available patterning strategies. In the initial chapter, a number of properties were identified that would be necessary for a biological nanopatterning technique: 1) accessibility to biological researchers, 2) high throughput, 3) direct control over feature geometries, 4) the ability to pattern on a variety of substrates, 5) control over topographical features, and 6) the ability to passivate the areas surrounding the patterns from non-specific protein and cell adhesion. Our patterning scheme currently addresses four of those properties well, and two with middling results that could be easily improved. We are able to control topographical feature dimension and depth by controlling film thickness and restricting the laser processing to a regime where only polymer is ablated. We are also able to ablate a range of feature geometries in our passivating film without substrate limitations.

Throughput limitations, as well as a number of other complications that have presented themselves, are related to the current stage setup. The current stage used to control the XY position of the sample is substandard to the work we hoped to accomplish. Currently, the maximum stage speed is 0.2 mm/s with a minimum realizable step size of ~0.8 microns, severely restricting the types and area of patterns we were able to create. As the stage had very low positional accuracy (i.e. two 100 micron translations in opposite directions would result in a 5-10 micron difference in position), it was not possible to make patterns with pitches below approximately one micron. The stage also occasionally had small undulations in the z (focal) axis as it moved, which would cause the sample to move in and out of an ideal focal range. This affected both feature geometry and the quality of ablation. Unrelated to the stage, small deviations in laser quality and optical alignment can have significant effects on this type of threshold ablation process, requiring frequent recalibration of the effect of laser fluence on feature size. This is compounded by the fact that small changes (~5nm) in film thickness can influence the ablation process as well, as removal of thicker films requires higher laser fluence.

Issues of throughput and reliability hampered our ability to generate the amounts and areas of samples required for comprehensive cell studies. Gradients and isometric patterns with a variety of feature sizes patterned in a single day were the ideal investigative substrates, as these minimized the effect of small laser or film thickness variations. Repeatability also became an issue when attempting to create replicate samples for statistical analysis. As such, staining and single cell metrics would be ideal for these types of small, nanopatterned samples. Overall, laser nanomachining is a simple process that requires no special substrates or processing

environments, with throughput currently on par with e-beam lithography. Issues with throughput and patterning reliability are easily solvable by incorporating a more stable, high speed stage and an autofocus module, both of which have been purchase and are projected to come online shortly.

The final need for this patterning technique is accessibility to biological researchers. In this respect, femtosecond laser nanomachining has no significant advantages to other serial techniques. We were fortunate to find a willing collaborator on campus with an amplified system capable of generating the nanopatterns that we desired. These amplified systems are quite expensive to purchase and maintain and are not widely available to the biological community. The obvious need for a high quality stage has also been outlined, creating yet another barrier to entry. However, non-amplified femtosecond lasers are integral components to most two photon microscopy systems that are becoming more prevalent in biology labs. Such systems have already been used to generate structured materials using localized photoconjugation or photopolymerization. Therefore, it is conceivable that these imaging systems could be modified or manufactured with the capability to create ablated surfaces as well.

## 7.3 - Future work

This work outlines the development of a patterning strategy to control cell behavior using nanopatterned substrates. As such, a wide range of future projects are immediately evident. Constraining ourselves to the current patterning methodology, a number of interesting cell experiments can be envisioned. Since the protein deposition on the surface depends simply on the physisorption of proteins into ablated craters, a wide range of peptides or proteins could be presented from the surface and a variety of cell types could be explored. Varying amino acid sequences designed to target different integrin subunits, mixtures of peptides designed to a cohort of integrin or Syndecan receptors, mixtures of peptides and biotinylated growth factors, steroids, or hormones designed to elicit particular cell responses could all be created using our patterning technique.

As our patterning method controls the diameter of cell adhesive ligands, a straightforward study would involve varying the area of the adhesive domain while maintaining projected peptide density and quantifying the geometry of the focal adhesions formed. This change in adhesion geometry could then be correlated qualitatively to actin cytoskeletal formation and quantitatively to NSI, similar to the isometric patterned samples outlined in Chapter 6. The same study could then be repeated for consistent adhesion spot sizes, but varying the pEG film thickness to elucidate the limit to which a cell membrane is able to deform on a surface during sampling.

Following the incorporation of a higher throughput stage and an autofocus module, creating large numbers of high area, repeat samples will allow for more standard functional or differentiation studies. The patterns described in Chapter 6 and the above paragraph can be repeated on a large scale, to determine if the observed changes in adhesion area, cytoskeletal formation, and NSI correlate to a variable differentiation profile for pluripotent cells, such as hMSCs. Specifically, larger patterned areas will provide a stronger signal for quantitative PCR and microarray analysis of a range of differentiation genes.

A number of other technological developments on the patterning technique are feasible. The current system of adsorbing avidin/biotin into the craters to present peptides limits us to a

maximum peptide density of 12.6 pmol/cm$^2$, a rather low upper limit considering the significant reduction in density when the peptide is constrained to a nanopatterned area. Other proteins have been adsorbed into the craters, including serum proteins and fibronectin, but this removes an element of control from the system. With clean film removal, it may be possible to insert other chemistries into the ablated crater, potentially by reactivating the surface and polymerizing a different polymer that could conjugate directly to the peptide of interest. This would create a covalent link between the adhesive ligand and the surface, establishing a more robust interface. Dendritic polymers with high peptide densities could also be conjugated onto a silane modified ablated crater in order to covalently link a much higher density of adhesive ligands to surface.

Although a new stage and autofocus module will largely address issues related to throughput and repeatability, using laser nanomachining with imprint lithography could be a viable alternative to the serial processing outlined above. A mask or stencil patterned with pulse laser energy could be reused multiple times to generate repeat samples for statistical analysis, or to recreate a sample multiple times for process (such as staining) optimization, eliminating the need to spend multiple hours generating each individual sample. For example, a stencil with nanoscale openings could be used to selectively plasma treat or debrominate a silane initiator modified substrate, resulting in nanometer scale gaps in brush layer growth.

Abstractly considering the patterning method as simple creating two areas of differing chemistries, one can see that future technological development for this technique are varied and wide ranging. Should upgrading the stage and focusing method resolve the aforementioned limitations on throughput and repeatability, the femtosecond laser nanomachining process derived here could be a powerful technique for mechanistically studying the effect of cell-substrate interactions on cell behavior and fate.

# References

1.      Chen, C.S., et al., *Geometric control of cell life and death.* Science, 1997. **276**(5317): p. 1425-1428.
2.      MacBeath, G. and S.L. Schreiber, *Printing proteins as microarrays for high-throughput function determination.* Science, 2000. **289**(5485): p. 1760-1763.
3.      Lelievre, S.A., et al., *Tissue phenotype depends on reciprocal interactions between the extracellular matrix and the structural organization of the nucleus.* Proc. Natl. Acad. Sci, 1998. **95**: p. 14711-14716.
4.      Rezania, A. and K.E. Healy, *The effect of peptide surface density on mineralization of a matrix deposited by osteogenic cells.* Journal of Biomedical Materials Research, 2000. **52**(4): p. 595-600.
5.      Singhvi, R., et al., *Engineering cell shape and function.* Science., 1994. **264**: p. 696-698.
6.      Thomas, C.H., et al., *Engineering gene expression and protein synthesis by modulation of nuclear shape.* Proceedings of the National Academy of Sciences of the United States of America, 2002. **99**(4): p. 1972-1977.
7.      Watt, F.M., P.W. Jordan, and C.H. O'Neill, *Cell shape controls terminal differentiation of human epidermal keratinocytes.* Proc. Natl. Acad. Sci., 1988. **85**: p. 5576-5580.
8.      Chen, C.S., et al., *Cell shape provides global control of focal adhesion assembly.* Biochemical And Biophysical Research Communications, 2003. **307**(2): p. 355-361.
9.      Folkman, J. and A. Moscona, *Role of cell shape in growth control.* Nature, 1978. **273**: p. 345-349.
10.     Aubin, J.E., et al., *Osteoblast and chondroblast differentiation.* Bone, 1995. **17**: p. 77s-83s.
11.     Folch, A. and M. Toner, *Microengineering of cellular interactions.* Annual Review of Biomedical Engineering, 2000. **2**: p. 227-+.
12.     Schmidt, R.C. and K.E. Healy, *Controlling biological interfaces on the nanometer length scale.* Journal of Biomedical Materials Research Part A, 2009. **90A**(4): p. 1252-1261.
13.     Watkins, J.J. and D.J. Bishop, *Fabrication of sub-45nm structures for the next generation of devices: A lot of effort for a little device.* Mrs Bulletin, 2005. **30**(12): p. 937-939.
14.     Odom, T.W., et al., *Improved pattern transfer in soft lithography using composite stamps.* Langmuir, 2002. **18**(13): p. 5314-5320.
15.     Li, H.W., et al., *Nanocontact printing: A route to sub-50-nm-scale chemical and biological patterning.* Langmuir, 2003. **19**(6): p. 1963-1965.
16.     Christman, K.L., et al., *Submicron streptavidin patterns for protein assembly.* Langmuir, 2006. **22**(17): p. 7444-7450.
17.     Lim, J.H., et al., *Direct-write dip-pen nanolithography of proteins on modified silicon oxide surfaces.* Angewandte Chemie-International Edition, 2003. **42**(20): p. 2309-2312.
18.     Gu, J.H., et al., *Nanometric protein arrays on protein-resistant monolayers on silicon surfaces.* Journal Of The American Chemical Society, 2004. **126**(26): p. 8098-8099.
19.     Pavlovic, E., S. Oscarsson, and A.P. Quist, *Nanoscale site-specific immobilization of proteins through electroactivated disulfide exchange.* Nano Letters, 2003. **3**(6): p. 779-781.
20.     Choi, I., et al., *In situ observation of biomolecules patterned on a PEG-modified Si surface by scanning probe lithography.* Biomaterials, 2006. **27**(26): p. 4655-4660.

21.     Naujoks, N. and A. Stemmer, *Using local surface charges for the fabrication of protein patterns.* Colloids And Surfaces A-Physicochemical And Engineering Aspects, 2004. **249**(1-3): p. 69-72.

22.     Fresco, Z.M., et al., *AFM-induced amine deprotection: Triggering localized bond cleavage by application of tip/substrate voltage bias for the surface self-assembly of nanosized dendritic objects.* Journal of the American Chemical Society, 2004. **126**(27): p. 8374-8375.

23.     Hyun, J., et al., *Molecular recognition-mediated fabrication of protein nanostructures by dip-pen lithography.* Nano Letters, 2002. **2**(11): p. 1203-1207.

24.     Lee, S.W., et al., *Biologically active protein nanoarrays generated using parallel dip-pen nanolithography.* Advanced Materials, 2006. **18**(9): p. 1133-+.

25.     Valiokas, R., et al., *Selective recruitment of membrane protein complexes onto gold substrates patterned by dip-pen nanolithography.* Langmuir, 2006. **22**(8): p. 3456-3460.

26.     Wilson, D.L., et al., *Surface organization and nanopatterning of collagen by dip-pen nanolithography.* Proceedings Of The National Academy Of Sciences Of The United States Of America, 2001. **98**(24): p. 13660-13664.

27.     Pena, D.J., M.P. Raphael, and J.M. Byers, *"Dip-Pen" nanolithography in registry with photolithography for biosensor development.* Langmuir, 2003. **19**(21): p. 9028-9032.

28.     Jung, H., et al., *Surfactant activated dip-pen nanolithography.* Nano Letters, 2004. **4**(11): p. 2171-2177.

29.     Kenseth, J.R., et al., *Investigation of approaches for the fabrication of protein patterns by scanning probe lithography.* Langmuir, 2001. **17**(13): p. 4105-4112.

30.     Wadu-Mesthrige, K., et al., *Fabrication of nanometer-sized protein patterns using atomic force microscopy and selective immobilization.* Biophysical Journal, 2001. **80**(4): p. 1891-1899.

31.     Hoover, D.K., et al., *Electroactive nanoarrays for biospecific ligand mediated studies of cell adhesion.* Chembiochem, 2007. **8**: p. 1920-+.

32.     Bruckbauer, A., et al., *Multicomponent submicron features of biomolecules created by voltage controlled deposition from a nanopipet.* Journal Of The American Chemical Society, 2003. **125**(32): p. 9834-9839.

33.     Taha, H., et al., *Protein printing with an atomic force sensing nanofountainpen.* Applied Physics Letters, 2003. **83**(5): p. 1041-1043.

34.     Kwon, S., W. Chang, and S. Jeong, *Shape and size variations during nanopatterning of photoresist using near-field scanning optical microscope.* Ultramicroscopy, 2005. **105**(1-4): p. 316-323.

35.     Sun, S. and G.J. Leggett, *Matching the resolution of electron beam lithography by scanning near-field photolithography.* Nano Letters, 2004. **4**(8): p. 1381-1384.

36.     Bhatnagar, P., et al., *Dendrimer-scaffod-based electron-beam patterning of biomolecules.* Advanced Materials, 2006. **18**(3): p. 315-+.

37.     Zhang, G.J., et al., *Nanoscale patterning of protein using electron beam lithography of organosilane self-assembled monolayers.* Small, 2005. **1**(8-9): p. 833-837.

38.     Powell, T. and J.Y. Yoon, *Fluorescent biorecognition of gold nanoparticle-IgG conjugates self-assembled on e-beam patterns.* Biotechnology Progress, 2006. **22**(1): p. 106-110.

39.     Bretagnol, F., et al., *Fabrication of functional nano-patterned surfaces by a combination of plasma processes and electron-beam lithography.* Nanotechnology, 2007. **18**(13).

40.     Kunzi, P.A., et al., *Nanofabrication of protein-patterned substrates for future cell adhesion experiments.* Microelectronic Engineering, 2005. **78-79**: p. 582-586.

41.     Lussi, J.W., et al., *Selective molecular assembly patterning at the nanoscale: a novel platform for producing protein patterns by electron-beam lithography on SiO2/indium tin oxide-coated glass substrates.* Nanotechnology, 2005. **16**(9): p. 1781-1786.

42.     Curtis, A.S.G., et al., *Substratum nanotopography and the adhesion of biological cells. Are symmetry or regularity of nanotopography important?* Biophysical Chemistry, 2001. **94**(3): p. 275-283.

43.     Teixeira, A.I., et al., *Epithelial contact guidance on well-defined micro- and nanostructured substrates.* Journal Of Cell Science, 2003. **116**(10): p. 1881-1892.

44.     Karuri, N.W., et al., *Biological length scale topography enhances cell-substratum adhesion of human corneal epithelial cells.* Journal Of Cell Science, 2004. **117**(15): p. 3153-3164.

45.     Teixeira, A.I., et al., *The effect of environmental factors on the response of human corneal epithelial cells to nanoscale substrate topography.* Biomaterials, 2006. **27**(21): p. 3945-3954.

46.     Hoff, J.D., et al., *Nanoscale protein patterning by imprint lithography.* Nano Letters, 2004. **4**(5): p. 853-857.

47.     Park, S., et al., *Chemical patterning of sub-50-nm half pitches via nanoimprint lithography.* Microelectronic Engineering, 2005. **78-79**: p. 682-688.

48.     Coyer, Sean R., Andrés J. García, and E. Delamarche, *Facile Preparation of Complex Protein Architectures with Sub-100-nm Resolution on Surfaces.* Angewandte Chemie International Edition, 2007. **46**(36): p. 6837-6840.

49.     Yim, E.K.F., et al., *Nanopattern-induced changes in morphology and motility of smooth muscle cells.* Biomaterials, 2005. **26**(26): p. 5405-5413.

50.     Johansson, F., et al., *Axonal outgrowth on nano-imprinted patterns.* Biomaterials, 2006. **27**(8): p. 1251-1258.

51.     Liliensiek, S.J., et al., *The scale of substratum topographic features modulates proliferation of corneal epithelial cells and corneal fibroblasts.* Journal Of Biomedical Materials Research Part A, 2006. **79A**(1): p. 185-192.

52.     Arnold, M., et al., *Activation of integrin function by nanopatterned adhesive interfaces.* Chemphyschem, 2004. **5**(3): p. 383-388.

53.     Walter, N., et al., *Cellular unbinding forces of initial adhesion processes on nanopatterned surfaces probed with magnetic tweezers.* Nano Letters, 2006. **6**(3): p. 398-402.

54.     Cavalcanti-Adam, E.A., et al., *Cell spreading and focal adhesion dynamics are regulated by spacing of integrin ligands.* Biophysical Journal, 2007. **92**(8): p. 2964-2974.

55.     Glass, R., M. Moller, and J.P. Spatz, *Block copolymer micelle nanolithography.* Nanotechnology, 2003. **14**(10): p. 1153-1160.

56.     Agheli, H., et al., *Large area protein nanopatterning for biological applications.* Nano Letters, 2006. **6**(6): p. 1165-1171.

57.     Agheli, H., et al., *Narlostructured biointerfaces.* Materials Science & Engineering C-Biomimetic And Supramolecular Systems, 2006. **26**(5-7): p. 911-917.

58.     Cai, Y.G. and B.M. Ocko, *Large-scale fabrication of protein nanoarrays based on nanosphere lithography.* Langmuir, 2005. **21**(20): p. 9274-9279.

59.    Michel, R., et al., *A novel approach to produce biologically relevant chemical patterns at the nanometer scale: Selective molecular assembly patterning combined with colloidal lithography.* Langmuir, 2002. **18**(22): p. 8580-8586.

60.    Valsesia, A., et al., *Selective immobilization of protein clusters on polymeric nanocraters.* Advanced Functional Materials, 2006. **16**(9): p. 1242-1246.

61.    Masuhara, H., T. Asahi, and Y. Hosokawa, *Laser nanochemistry.* Pure and Applied Chemistry, 2006. **78**(12): p. 2205-2226.

62.    Glezer, E.N., et al., *Three-dimensional optical storage inside transparent materials.* Optics Letters, 1996. **21**(24): p. 2023-2025.

63.    Stuart, B.C., et al., *Optical ablation by high-power short-pulse lasers.* Journal of the Optical Society of America B-Optical Physics, 1996. **13**(2): p. 459-468.

64.    Kruger, J. and W. Kautek, *Ultrashort pulse laser interaction with dielectrics and polymers.* Polymers And Light, 2004. **168**: p. 247-289.

65.    Jones, S.C., et al., *RECENT PROGRESS ON LASER-INDUCED MODIFICATIONS AND INTRINSIC BULK DAMAGE OF WIDE-GAP OPTICAL-MATERIALS.* Optical Engineering, 1989. **28**(10): p. 1039-1068.

66.    Kuper, S. and J. Brannon, *KRF-LASER ABLATION OF POLYURETHANE.* Applied Physics A-Materials Science & Processing, 1993. **57**(3): p. 255-259.

67.    Thomas, C.H., et al., *Surfaces designed to control the projected area and shape of individual cells.* Journal Of Biomechanical Engineering-Transactions Of The Asme, 1999. **121**(1): p. 40-48.

68.    Giancotti, F.G. and E. Ruoslahti, *Integrin signaling.* Science, 1999. **285**(5430): p. 1028-32.

69.    Humphries, J.D., A. Byron, and M.J. Humphries, *Integrin ligands at a glance.* Journal of Cell Science, 2006. **119**(19): p. 3901-3903.

70.    Maniotis, A.J., C.S. Chen, and D.E. Ingber, *Demonstration of mechanical connections between integrins cytoskeletal filaments, and nucleoplasm that stabilize nuclear structure.* Proceedings Of The National Academy Of Sciences Of The United States Of America, 1997. **94**(3): p. 849-854.

71.    Engler, A.J., et al., *Matrix elasticity directs stem cell lineage specification.* Cell, 2006. **126**(4): p. 677-689.

72.    Bidwell, J.P., et al., *Osteocalcin gene promoter-binding factors are tissue-specific nuclear matrix components.* Proc Natl Acad Sci USA, 1993. **90**: p. 3162-3166.

73.    Bearinger, J.P., et al., *P(AAm-co-EG) interpenetrating polymer networks grafted to oxide surfaces: surface characterization, protein adsorption, and cell detachment studies.* Langmuir, 1997. **13**(19): p. 5175-5183.

74.    Fan, X.W., et al., *Biomimetic anchor for surface-initiated polymerization from metal substrates.* Journal Of The American Chemical Society, 2005. **127**(45): p. 15843-15847.

75.    Fan, X.W., L.J. Lin, and P.B. Messersmith, *Cell fouling resistance of polymer brushes grafted from Ti substrates by surface-initiated polymerization: Effect of ethylene glycol side chain length.* Biomacromolecules, 2006. **7**(8): p. 2443-2448.

76.    Kaholek, M., et al., *Fabrication of stimulus-responsive nanopatterned polymer brushes by scanning-probe lithography.* Nano Letters, 2004. **4**(2): p. 373-376.

77.    Kizhakkedathu, J.N., R. Norris-Jones, and D.E. Brooks, *Synthesis of well-defined environmentally responsive polymer brushes by aqueous ATRP.* Macromolecules, 2004. **37**(3): p. 734-743.

78. Nagase, K., et al., *Effects of Graft Densities and Chain Lengths on Separation of Bioactive Compounds by Nanolayered Thermoresponsive Polymer Brush Surfaces.* Langmuir, 2007.

79. Yamamoto, S.i., J. Pietrasik, and K. Matyjaszewski, *ATRP Synthesis of Thermally Responsive Molecular Brushes from Oligo(ethylene oxide) Methacrylates.* Macromolecules, 2007. **40**(26): p. 9348-9353.

80. Patten, T.E. and K. Matyjaszewski, *Atom transfer radical polymerization and the synthesis of polymeric materials.* Advanced Materials, 1998. **10**(12): p. 901-+.

81. Matyjaszewski, K., T.E. Patten, and J.H. Xia, *Controlled/"living" radical polymerization. Kinetics of the homogeneous atom transfer radical polymerization of styrene.* Journal of the American Chemical Society, 1997. **119**(4): p. 674-680.

82. Tang, W. and K. Matyjaszewski, *Kinetic Modeling of Normal ATRP, Normal ATRP with [Cu-II](o), Reverse ATRP and SR&NI ATRP.* Macromolecular Theory and Simulations, 2008. **17**(7-8): p. 359-375.

83. Patten, T.E., et al., *Polymers with very low polydispersities from atom transfer radical polymerization.* Science, 1996. **272**(5263): p. 866-868.

84. Ma, H.W., et al., *Protein-resistant polymer coatings on silicon oxide by surface-initiated atom transfer radical polymerization.* Langmuir, 2006. **22**(8): p. 3751-3756.

85. Irwin, E.F., et al., *Modulus-dependent macrophage adhesion and behavior.* Journal Of Biomaterials Science-Polymer Edition, 2008. **19**(10): p. 1363-1382.

86. Saha, K., et al., *Biomimetic interfacial interpenetrating polymer networks control neural stem cell behavior.* Journal of Biomedical Materials Research Part A, 2007. **81A**(1): p. 240-249.

87. Irwin, E.F., et al., *Analysis of interpenetrating polymer networks via quartz crystal microbalance with dissipation monitoring.* Langmuir, 2005. **21**(12): p. 5529-5536.

88. Barron, J.A., et al., *Biological laser printing: A novel technique for creating heterogeneous 3-dimensional cell patterns.* Biomedical Microdevices, 2004. **6**(2): p. 139-147.

89. Luo, Y. and M.S. Shoichet, *A photolabile hydrogel for guided three-dimensional cell growth and migration.* Nature Materials, 2004. **3**(4): p. 249-253.

90. Balgar, T., et al., *Preparation of submicron-structured alkylsiloxane monolayers using prepatterned silicon substrates by laser direct writing.* Langmuir, 2004. **20**(9): p. 3525-3527.

91. Underwood, J.M., et al., *Pulse energy dependence of subcellular dissection by femtosecond laser pulses.* Optics Express, 2005. **13**(10): p. 3690-3696.

92. Hwang, D.J., C.P. Grigoropoulos, and T.Y. Choi, *Efficiency of silicon micromachining by femtosecond laser pulses in ambient air.* Journal Of Applied Physics, 2006. **99**(8).

93. Hwang, D.J., et al., *Femtosecond laser ablation induced plasma characteristics from submicron craters in thin metal film.* Applied Physics Letters, 2007. **91**.

94. Holmberg, A., et al., *The biotin-streptavidin interaction can be reversibly broken using water at elevated temperatures.* Electrophoresis, 2005. **26**(3): p. 501-510.

95. Basham, L.E., et al., *A simple, quantitative, reproducible avidin-biotin ELISA for the evaluation of group B Streptococcus type-specific antibodies in humans.* Vaccine, 1996. **14**(5): p. 439-445.

96.     Martin, H., et al., *A fluorescence polarization assay to quantify biotin and biotin-binding proteins in whole plant extracts using Alexa-Fluor 594 biocytin.* Analytical Biochemistry, 2008. **381**(1): p. 107-112.

97.     Shenai, B.R., et al., *Recombinant antigen-based avidin-biotin microtiter enzyme-linked immunosorbent assay for serodiagnosis of invasive amebiasis.* Journal of Clinical Microbiology, 1996. **34**(4): p. 828-833.

98.     Wang, S.H., et al., *Identification and characterization of Bacillus anthracis by multiplex PCR on DNA chip.* Biosensors & Bioelectronics, 2004. **20**(4): p. 807-813.

99.     Bhat, V.D., G.A. Truskey, and W.M. Reichert, *Fibronectin and avidin-biotin as a heterogeneous ligand system for enhanced endothelial cell adhesion.* Journal of Biomedical Materials Research, 1998. **41**(3): p. 377-85.

100.    Matsumoto, Y., et al., *New fluorometric enzyme immunoassay for 17 beta-estradiol by homogeneous reaction using biotinylated estradiol.* Talanta, 2006. **69**(3): p. 663-668.

101.    Yang, Z.P. and A. Chilkoti, *Microstamping of a biological ligand onto an activated polymer surface.* Advanced Materials, 2000. **12**(6): p. 413-+.

102.    Patel, N., et al., *Printing patterns of biospecifically-adsorbed protein.* Journal Of Biomaterials Science-Polymer Edition, 2000. **11**(3): p. 319-331.

103.    Wilchek, M. and E.A. Bayer, *THE AVIDIN BIOTIN COMPLEX IN IMMUNOLOGY.* Immunology Today, 1984. **5**(2): p. 39-43.

104.    Weber, P.C., et al., *STRUCTURAL ORIGINS OF HIGH-AFFINITY BIOTIN BINDING TO STREPTAVIDIN.* Science, 1989. **243**(4887): p. 85-88.

105.    Vermette, P., et al., *Immobilization and surface characterization of NeutrAvidin biotin-binding protein on different hydrogel interlayers.* Journal of Colloid and Interface Science, 2003. **259**(1): p. 13-26.

106.    Chung, E.H., et al., *Biomimetic artificial ECMs stimulate bone regeneration.* Journal Of Biomedical Materials Research Part A, 2006. **79A**(4): p. 815-826.

107.    Miura, T., et al., *Monitoring early differentiation events in human embryonic stem cells by massively parallel signature sequencing and expressed sequence tag scan.* Stem Cells and Development, 2004. **13**(6): p. 694-715.

108.    Hoffman, M.P., et al., *Cell type-specific differences in glycosaminoglycans modulate the biological activity of a heparin-binding peptide (RKRLQVQLSIRT) from the G domain of the laminin alpha 1 chain.* Journal of Biological Chemistry, 2001. **276**(25): p. 22077-22085.

109.    Le Trong, I., et al., *Structural characterization and comparison of RGD cell-adhesion recognition sites engineered into streptavidin.* Acta Crystallographica Section D-Biological Crystallography, 2003. **59**: p. 828-834.

110.    Meng, Y., et al., *Characterization of integrin engagement during defined human embryonic stem cell culture.* Faseb Journal. **24**(4): p. 1056-1065.

111.    Thomas, M.J. and E. Seto, *Unlocking the mechanisms of transcription factor YY1: are chromatin modifying enzymes the key?* Gene, 1999. **236**(2): p. 197-208.

112.    Aulthouse, A.L., *Prolonged exposure of human chondrocytes to ascorbic acid modifies cellular behavior in agarose gel.* The Anatomical Record, 1994. **238**: p. 31-37.

113.    McBeath, R., et al., *Cell shape, cytoskeletal tension, and RhoA regulate stem cell lineage commitment.* Developmental Cell, 2004. **6**(4): p. 483-495.

114.    Feldherr, C.M. and D. Akin, *Regulation of nuclear transport in proliferating and quiescent cells.* Experimental Cell Research, 1993. **205**: p. 179-186.

115.    Alvarez, M., et al., *Rat osteoblast and osteosarcoma nuclear matrix proteins bind with sequence specificity to the rat type I collagen promoter.* Endocrinology, 1997. **138**: p. 482-489.

116.    Bidwell, J.P., et al., *Nuclear matrix proteins and osteoblast gene expression.* J. Bone and Mineral Res., 1998. **13**(2): p. 155-167.

117.    Golzhauser, A., et al., *Chemical nanolithography with electron beams.* Advanced Materials, 2001. **13**(11): p. 806-+.

118.    Biebricher, A., et al., *Controlled three-dimensional immobilization of biomolecules on chemically patterned surfaces.* Journal of Biotechnology, 2004. **112**(1-2): p. 97-107.

119.    Harbers, G.M. and K.E. Healy, *The effect of ligand type and density on osteoblast adhesion, proliferation, and matrix mineralization.* Journal Of Biomedical Materials Research Part A, 2005. **75A**(4): p. 855-869.

120.    Barber, T.A., et al., *In vitro characterization of peptide-modified p(AAm-co-EG/AAc) IPN-coated titanium implants.* Journal Of Orthopaedic Research, 2006. **24**(7): p. 1366-1376.

121.    Pinn, E., et al., *Crystallization And Preliminary-X-Ray Investigation Of Avidin.* European Journal Of Biochemistry, 1982. **123**(3): p. 545-546.

# Appendix A - Line Patterns to control cell adhesion

We also created patterns of single lines by slowly rastering the sample through the laser at a high pulse frequency such that the ablation spots overlapped, creating lines of exposed quartz. Processing was done at slightly above the ablation threshold of the pEG brush layer, creating lines in which only the polymer was ablated and each section of the line was exposed to approximately 10-15 shots. Figure A.1 shows fluorescent micrographs of hMSCs adhered across line patterns with varying pitch between lines, ranging from 1 to 8 microns, with some 50 micron spaced lines to identify if single, extended cells could be isolated on linear nanopatterns. The lines on the sample run horizontal in the images, and are 450 nm in thickness.
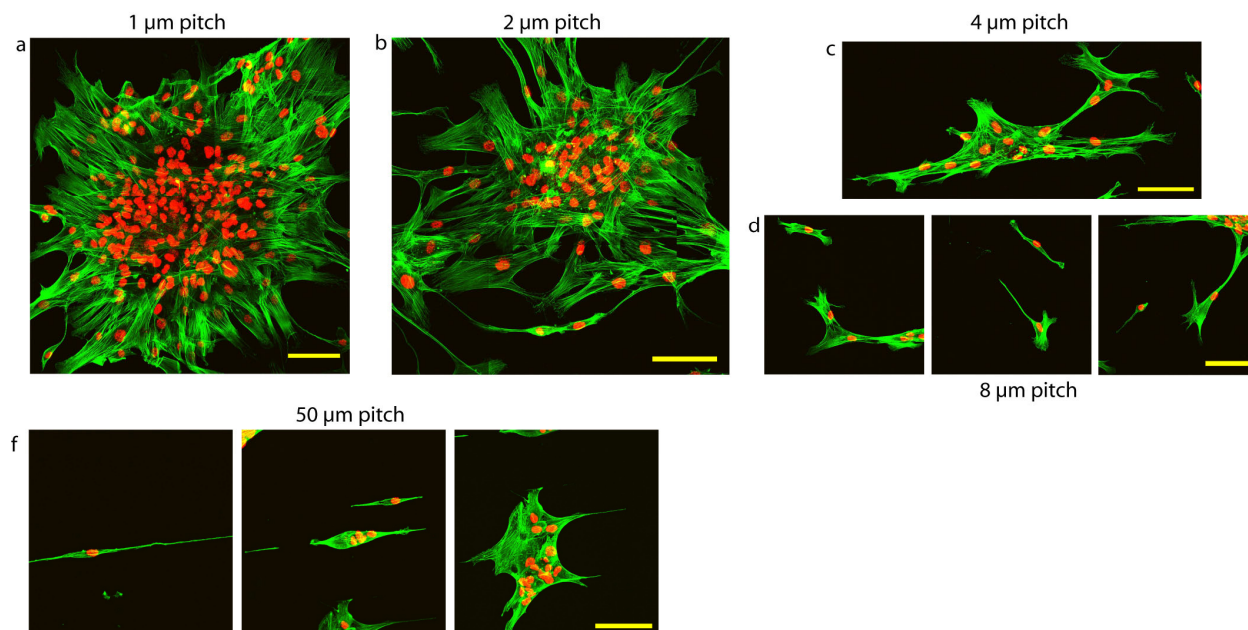


Figure A.1. Fluorescenct micrographs of hMSCs attached to horizontal line patterns with various pitches. For higher densities of lines (a-c) cells were able to form well adhered, large cell masses, while for higher pitches (d-f) cell attachment was sporadic and morphologies were more extended. Scale bars = 100 microns.

For line patterns, the projected peptide densities for various line pitches are presented in Table A.1. Low pitch patterns with a projected ligand density 2.9 pmol/cm$^2$ and greater resulted in the formation of large multilayer sheets or colony-like structures. Lines patterns with a projected density of 1.7 pmol/cm$^2$ (4 micron pitch) seemed to be in a transitional state between a colony like mass and the more isolated cells seen at 8 micron pitch and 0.7 pmol/cm$^2$. However, single cells were observed to attach and spread across high pitch lines, including those observed on 50 micron spacings, as shown in (f). It is also interesting to note that no contact guidance or cell orientation was observed for the hMSCs on the underlying line patterns, with the exception of spacings that were designed to isolate single.

Table A.1. Projected peptide densities on line patterns

| Pitch (µm) | Line thickness (nm) | Projected density (pmol/cm$^2$) |
|:---:|:---:|:---:|
| 1 | 450 | 5.7 |
| 2 | 450 | 2.9 |
| 4 | 450 | 1.4 |
| 8 | 450 | 0.7 |